The panorama of underlying electronic state in electron-doped cuprate $La_{2-x}Ce_xCuO_{4\pm\delta}$

and

Holographic Anti-Ferromagnetic state in Nickelate and Cobaltate, as $BiCoPO_5$ and Quantum Phase Transition induced by magnetic field

F.V. Kusmartsev , in collaboration with
IOP and ITP and Beijing University, CAS ,

State Key Laboratory of Theoretical Physics, Institute of Theoretical Physics,
Chinese Academy of Sciences,Beijing 100190, China.

Department of Physics, Loughborough University,
Loughborough, Leicestershire, LE11 3TU, United Kingdom

Joint Collaboration: UK, China, UAE

Heshan Yu[1,2,*], Xu Zhang[1,2,*], Runqiu Yang[3], Ge He[1,2], Ziquan Lin[4], Jinsong Zhang[1,2], Xinjian Wei[1,2], Wei Hu[1,2], Jie Yuan[1,2,6], Beiyi Zhu[1,2], Liang Li[4], Junfeng Wang[4,†], Yi-feng Yang[1,2,7], Tao Xiang[1,2,7], Ronggen Cai[2,8], and Kui Jin[1,2,6,7†]

Chinese Academy of Sciences

Anna Kusmartseva[5], F. V. Kusmartsev[5,†]

[1]Beijing National Laboratory for Condensed Matter Physics, Institute of Physics, Chinese Academy of Sciences, Beijing 100190, China.
[2]School of Physical Sciences, University of Chinese Academy of Sciences, Beijing 100049, China.
[3]Quantum Universe Center, Korea Institute for Advanced Study, Seoul 130-722, Korea
[4]Wuhan National High Magnetic Field Center (WHMFC), Huazhong University of Science and Technology, Wuhan 430074, China
[5]Department of Physics, Loughborough University, Loughborough LE11 3TU, United Kingdom
[6]Songshan Lake Materials Laboratory, Dongguan, Guangdong 523808, China
[7]Collaborative Innovation Center of Quantum Matter, Beijing, 100190, China
[8]CAS Key Laboratory of Theoretical Physics, Institute of Theoretical Physics, Chinese Academy of Sciences, Beijing 100190, China

$La_{2-x}Ce_xCuO_{4\pm\delta}$ (x = 0.10) thin films with slightly manipulated oxygen content by δ

- emergent electronic states as a function of magnetic field and assist in probing the nature of electron-doped cuprate from the aspects of plausible topological order with SR-SDW and the FM polarization.

- First, quantum phase transition from the AF state to ferromagnetism (FM) polarization is observed between 50 and 60 Tesla for different samples.

- The phase boundary shows a universal behavior that can be well described by the holographic model based on AdS/CFT.

- Second, a characteristic field between 20 and 30 Tesla, far beyond the upper critical field (i.e. H_{c2} ~ 10 T) be intimately related to the superconducting transition temperature

- Crossover from positive magnetoresistance to negative magnetoresistance at the zero temperature limits, linked to a plausible topological order with short-range spin density wave (SR-SDW) and a canted AF state,

The normalized temperature-field phase diagram of LCCO.

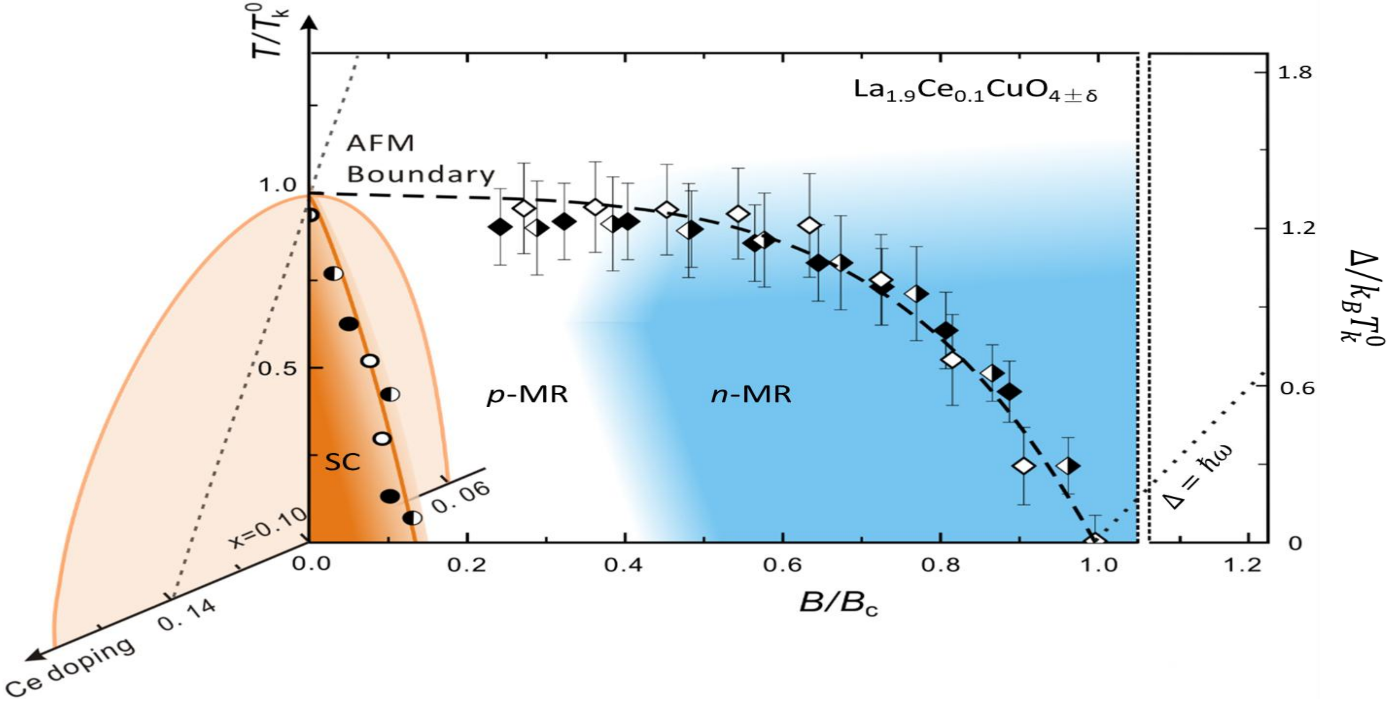

magneto-electrical transport in three optimal-doped LCCO samples with different oxygen content

The extensions of fitted curves (black dashed line) shows that the critical magnetic fields and onset temperature at zero field are $B_c \approx 62$ T, 55.2 T, 52 T and $T_k^0 \approx$ 32 K, 27 K, 26 K, respectively. After the normalizations by $T_k \to \frac{T_k}{T_k^0}$ and $B_c \to \frac{B_c}{B_c^0}$, fitted curves of three

Hall resistivity of optimal-doped LCCO at high magnetic field.

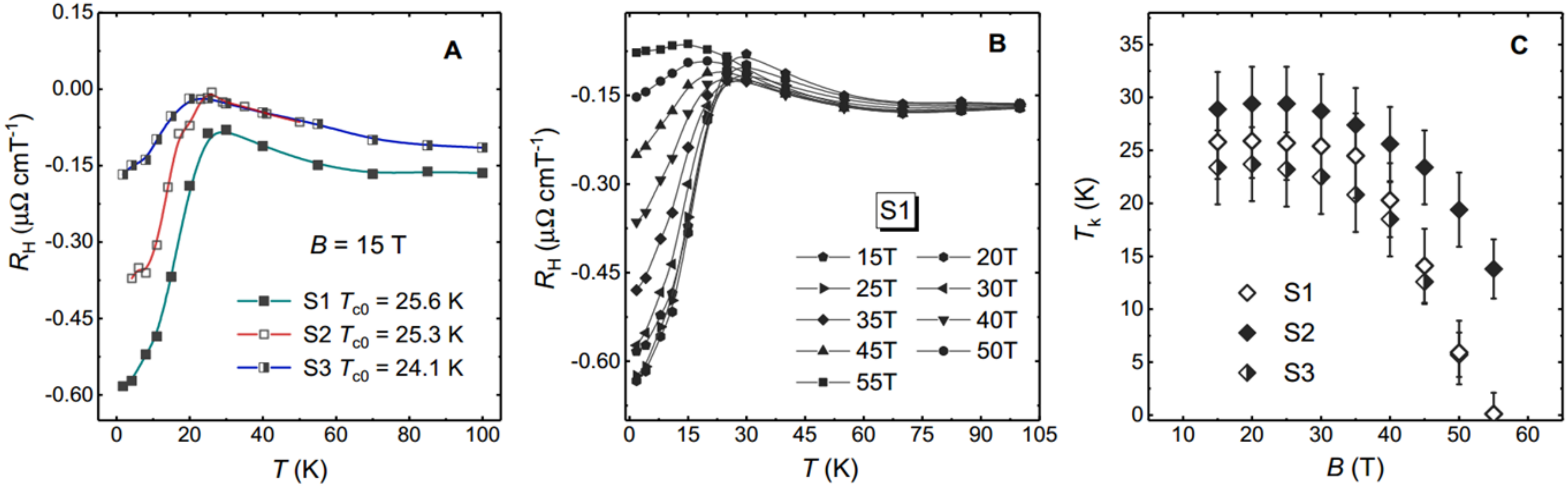

(A) Temperature dependence of Hall coefficient in 15 Tesla for all the samples. The kink behavior indicates Fermi-surface reconstruction at low temperature resulting from AFM transition. T_k of every sample are extracted from the apexes of curves.

(B) Temperature dependence of Hall coefficient in different fields up to 55 Tesla for S1. Hall kinks shift to low temperature with increasing field.

(C) The relationship between AFM transition temperature T_k and magnetic field B for three different samples.

Longitudinal Hall resistivity

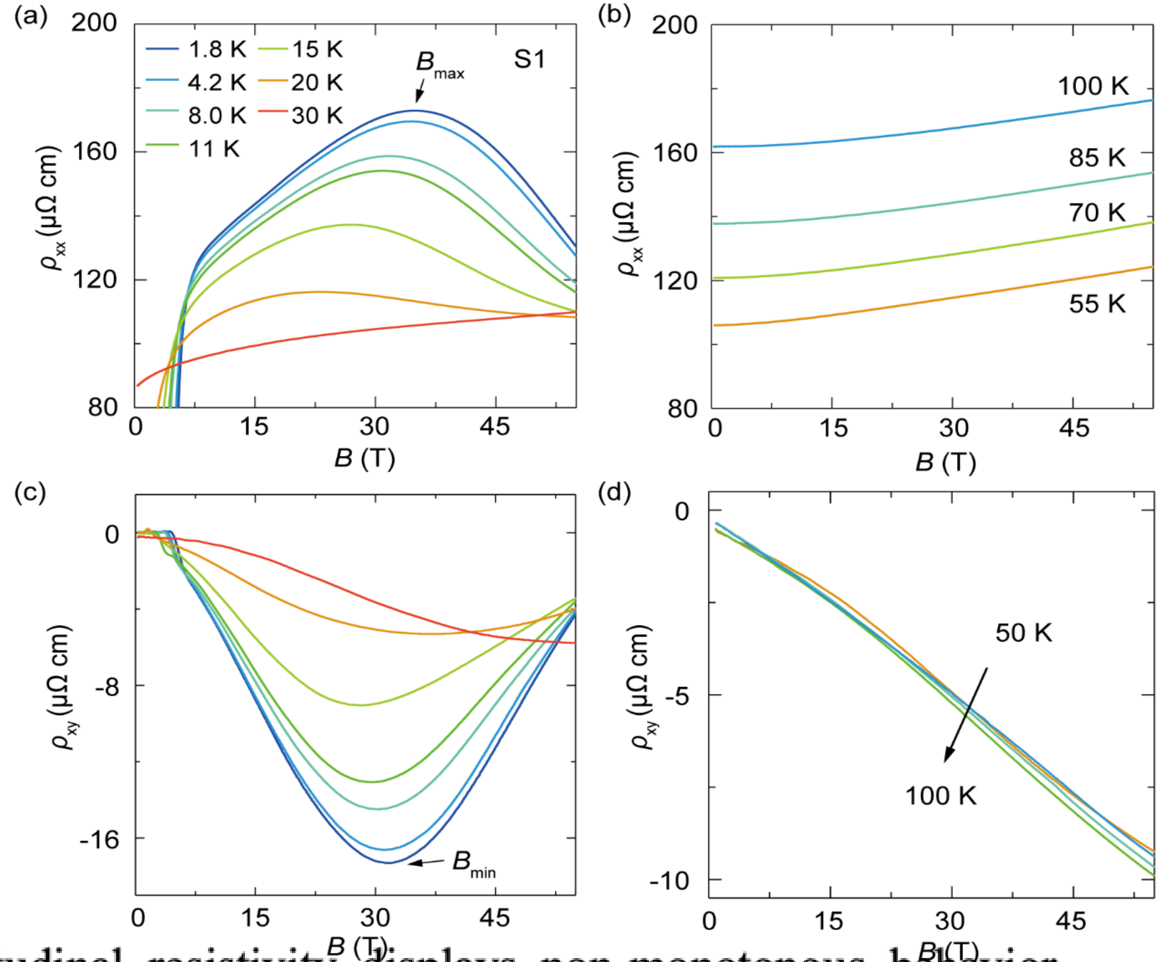

(a, b) The field-dependent longitudinal resistivity displays non-monotonous behavior below 30 K. The B_{max} marks the characteristic magnetic fields where the resistivity reaches the maximum. Above 30 K, magnetoresistance shows linearity at high magnetic fields.

(c, d) With decreasing temperature, there is a switching from linear to non-linear behavior. The minimum in ρ_{xy} curves corresponding to B_{max} also disappears above 30 K.

Magnetoresistivity of optimal-doped LCCO

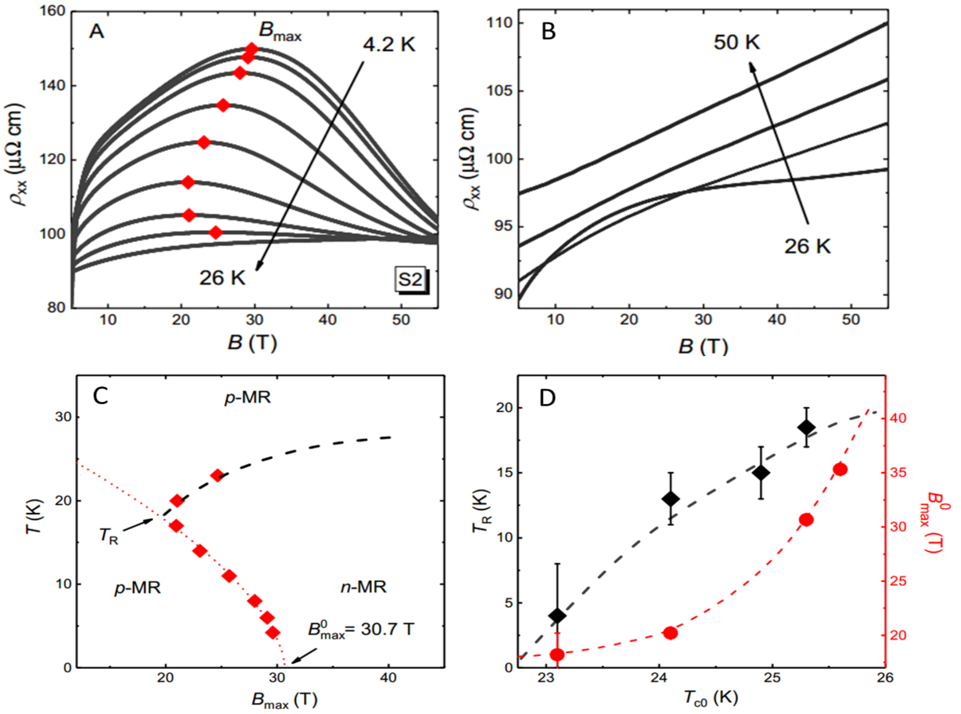

The p-MR at low temperatures seems unusually large compared to the normal MR. We take a definition of $\delta\rho(B) = \frac{d\rho(\mathrm{B})}{dB}\frac{1}{\rho(B)}$ to evaluate the magnitude of the anomalous p-MR.

Hall ‘kink’ and resistivity ‘upturn’

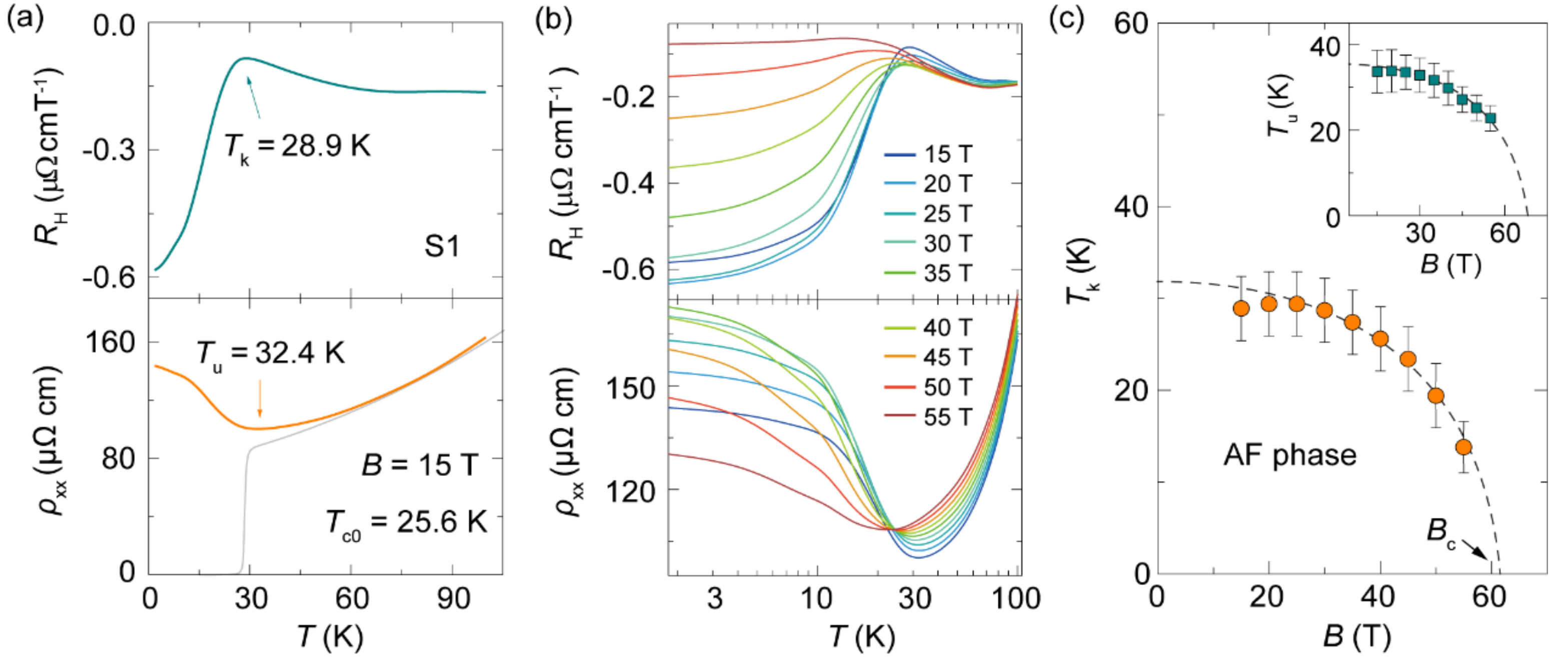

(a) Temperature dependence of the R_{H} and ρ_{xx} at 15 T for sample S1. T_{k} (T_{u}) is extracted from the maximum (minimum) of R_{H} (ρ_{xx}) curves.

- (b) Temperature dependence of the Hall coefficient (top panel) and resistivity (bottom panel) at different fields up to 55 T for sample S1.
- (c) The magnetic field dependence of T_{k}. Inset: The magnetic field dependence of T_{u}.

The Hall number and AF transition

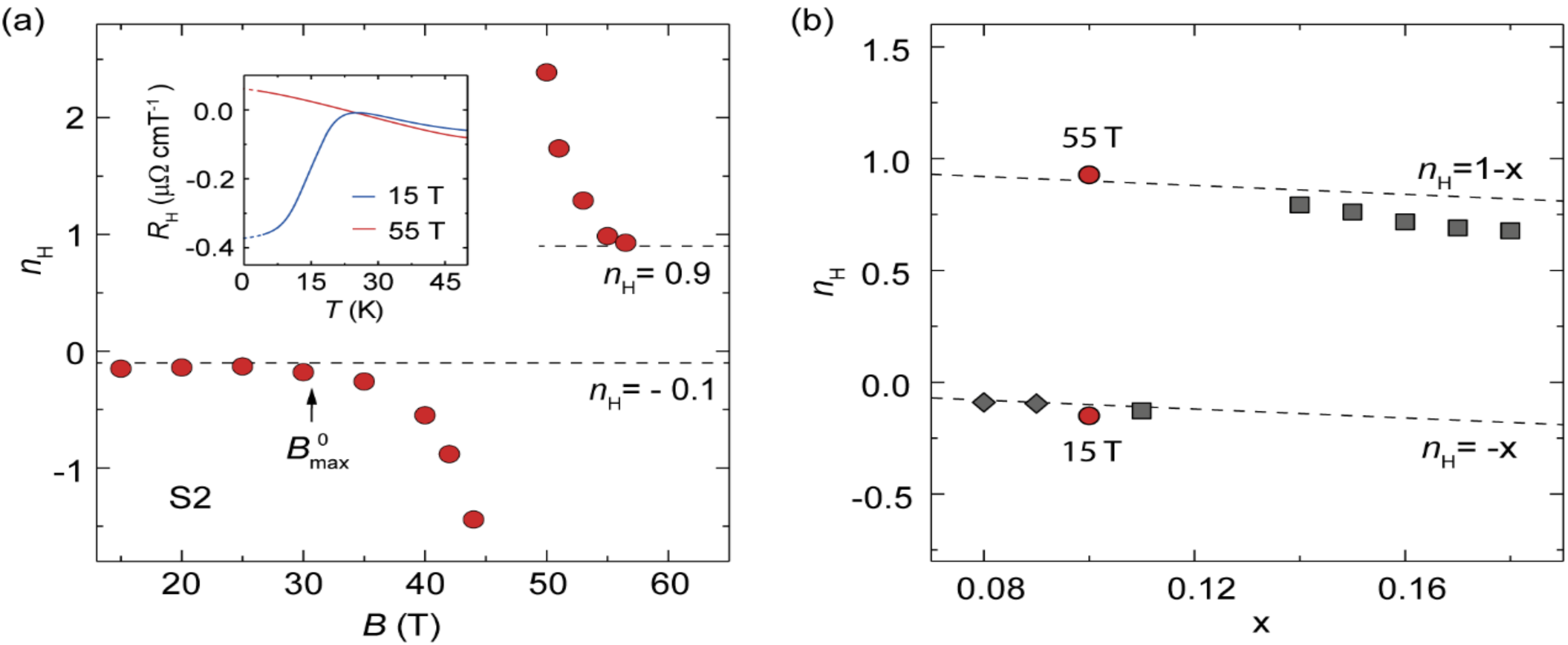

- (a) The Hall number n_{H} as a function of magnetic field. The n_{H} deviates from -0.1 at $B^0_{\max}$. Inset: Temperature dependence of the Hall coefficient at 15 and 55 T.
- (b) The Hall number n_{H} as a function of Ce doping (square from Ref. [17] and diamond from Ref. [18]). The upper dashed line marks $n_{\mathrm{H}} = 1 - x$; the lower dashed line marks $n_{\mathrm{H}} = -x$.

Topological order

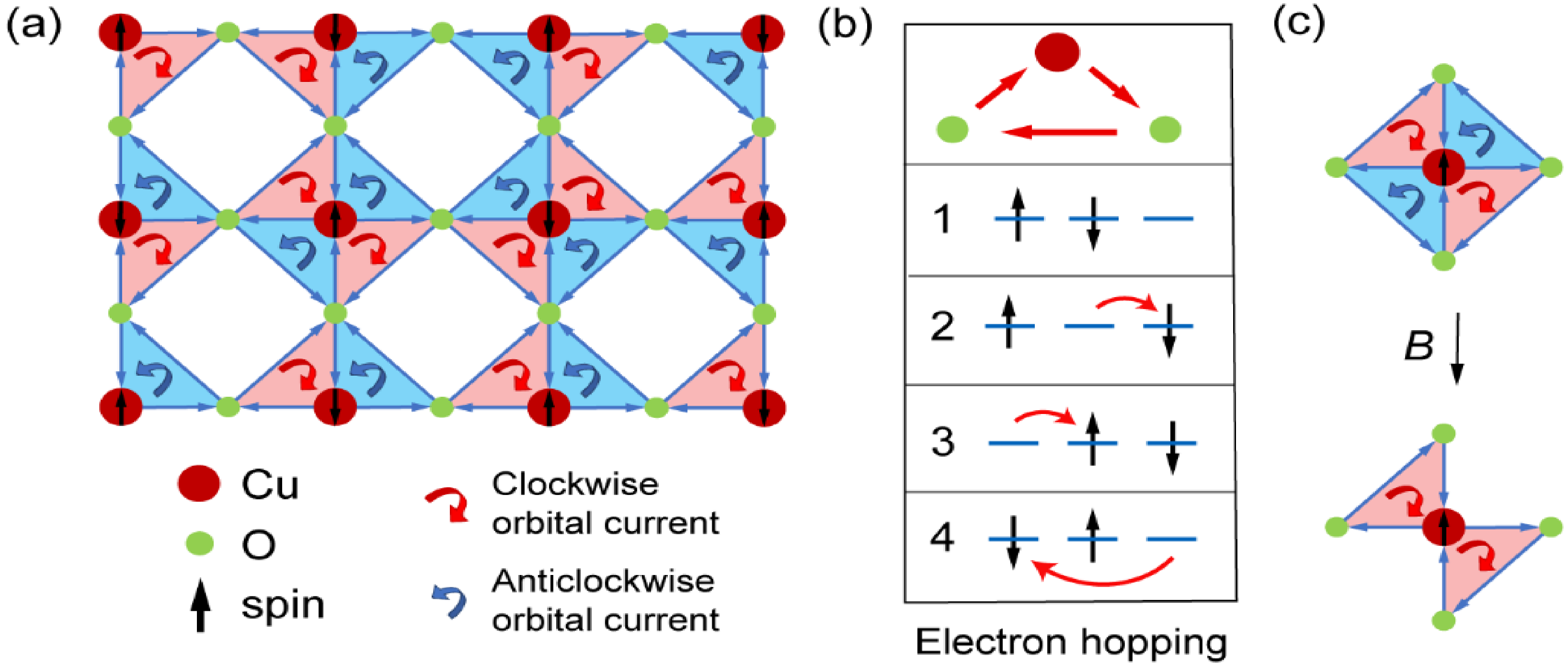

a Cu^{2+}-O-O triangular plaquette on the Cu-O plane, which has a pre-localized spin and two neighboring oxygens. Clockwise and anticlockwise π-orbital currents or moments are shown in pink and blue, respectively.

Topological Order and Phase transition

- a Cu^{2+}-O-O triangular plaquette on the Cu-O plane, which has a pre-localized spin and two neighboring oxygens. Clockwise and anticlockwise π-orbital currents or moments are shown in pink and blue, respectively.
-
- The sequence tunneling of a doped electron. Such state is unstable and this instability can lead to the formation of spontaneous local orbital current.

- A schematic depiction of the dissociation of the vortex-antivortex pairs (or clockwise and anticlockwise orbital currents) by magnetic field. The magnetic field is applied perpendicular to the plane of the quadruple moments.

- The field polarizes orbital currents of a particular chirality and thereby causes an unbinding of the vortex-antivortex pairs when the limit is approached.

- This leads to a Beresinki-Kosterlitz-Thouless like phase transition.

Doping vs Magnetic Field

- ARPES experiments have revealed a large hole-like pocket around (π, π) in overdoped $Nd_{2-x}Ce_xCuO_4$ (NCCO
- reconstructed to small electron pockets once AF state enters at lower Ce doping levels [19, 20].

- The resemblance between $n_{\mathrm{H}}(B)$ and $n_{\mathrm{H}}(x)$ suggests the recovery of a large hole pocket FS when the AF order is suppressed.

Holographic Top Down and Bottom Up

- What kind of Materials can be treated with Holographic Methods?

- What kind of States of Matter can be treated with Holographic Methods?

- Temperature as Hawking Temperature of black hole

- Quantum phase transitions!

We consider an Einstein-Maxwell theory in 3+1 dimensions with a negative cosmological constant and two anti-symmetry tensor fields $M^{(1)}_{\mu\nu}$ and $M^{(2)}_{\mu\nu}$. The total action reads

$$S = \int d^4x \, \sqrt{-g} \left[R - 2\Lambda - \frac{1}{4} F^2 - \lambda^2 (L_1 + L_2 + V_{12}) \right]$$

with

$$L_{\mathrm{a}} = \frac{1}{12} \left(dM^{(a)} \right)^2 + V(M^{(a)})$$

a = 1, 2 and

$$V_{12} = \frac{k}{2} M^{(1)\mu\nu} M^{(2)}_{\mu\nu}.$$

Here L_1 and L_2 are two bulk Lagrangians to describe the two different magnetic moments in staggered magnetization.

The term V_{12} describes the interaction between these two magnetic moments.

AF Order and QPT

The AF order parameter is the staggered magnetic moment, which is dual to xy-component $M_{\mathrm{xy}}^{(1)} - M_{\mathrm{xy}}^{(2)}$ in the interior. We fix the potential $V(M^{(\mathrm{a})})$ to be the following form

$$V\left(M^{(\mathrm{a})}\right) = M_{\mu\nu}^{(\mathrm{a})} M^{(\mathrm{a})\mu\nu} - \left(\epsilon_{\mu\nu\rho\sigma} M^{(\mathrm{a})\mu\nu} M^{(\mathrm{a})\rho\sigma}\right)^2.$$

In probe limit $\lambda \to 0$, the spacetime geometry in the interior is given by a dyonic AdS-Reissner-Nordstrom black hole which can be written as

$$\mathrm{ds}^2 = -r^2 f(r) dt^2 + \frac{dr^2}{r^2 f(r)} + r^2(dx^2 + dy^2),$$

$$f(r) = 1 - \frac{1 + \mu^2 + B^2}{r^3} + \frac{\mu^2 + B^2}{r^4}.$$

- chemical potential in the boundary is given by the constant μ,
- B can be viewed as the external magnetic field of the dual boundary field theory.

The compounds $BiMNO_5$ (M = Ni, Co, Ca, Cd, Pb, N = P, V, As)

Focus on Ni and Co: $BiCoPO_5$

- structure->: mixed double chains of
- Two edge-sharing CoO_6 octahedra, alternating
- With two edge sharing BiO_6 octahedra
- These two mixed chains are connected via oxi-phosphate PO_4 tetra-hedra
- Anti-ferro-magnetic at low T
- Interaction increases with Co->Ni

The compounds $BiMNO_5$ (M = Ni, Co, Ca, Cd, Pb, N = P, V, As)

Focus on Ni and Co: $BiCoPO_5$

- structure->: mixed double chains of
- Two edge-sharing MO_6 octahedra, alternating
- With two edge sharing BiO_6 octahedra

- Centre of inversion
- Between Bi atoms

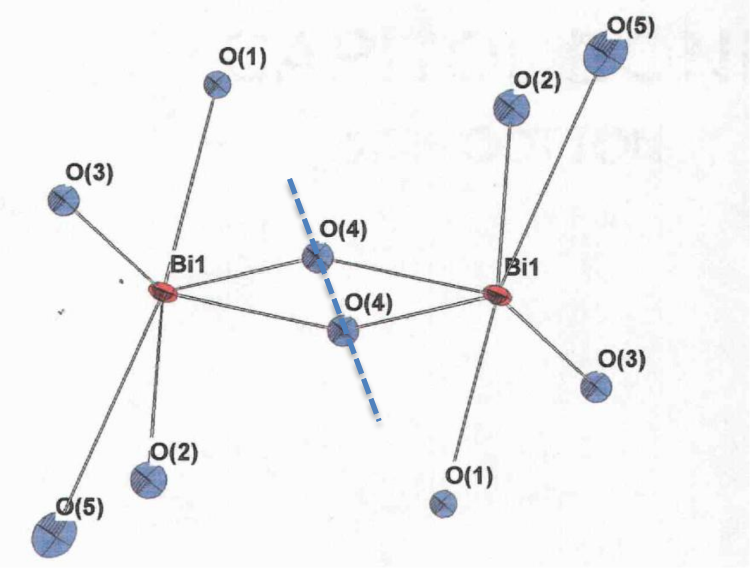

Co_2 O_{10}-group

- The centre of inversion between Co atoms

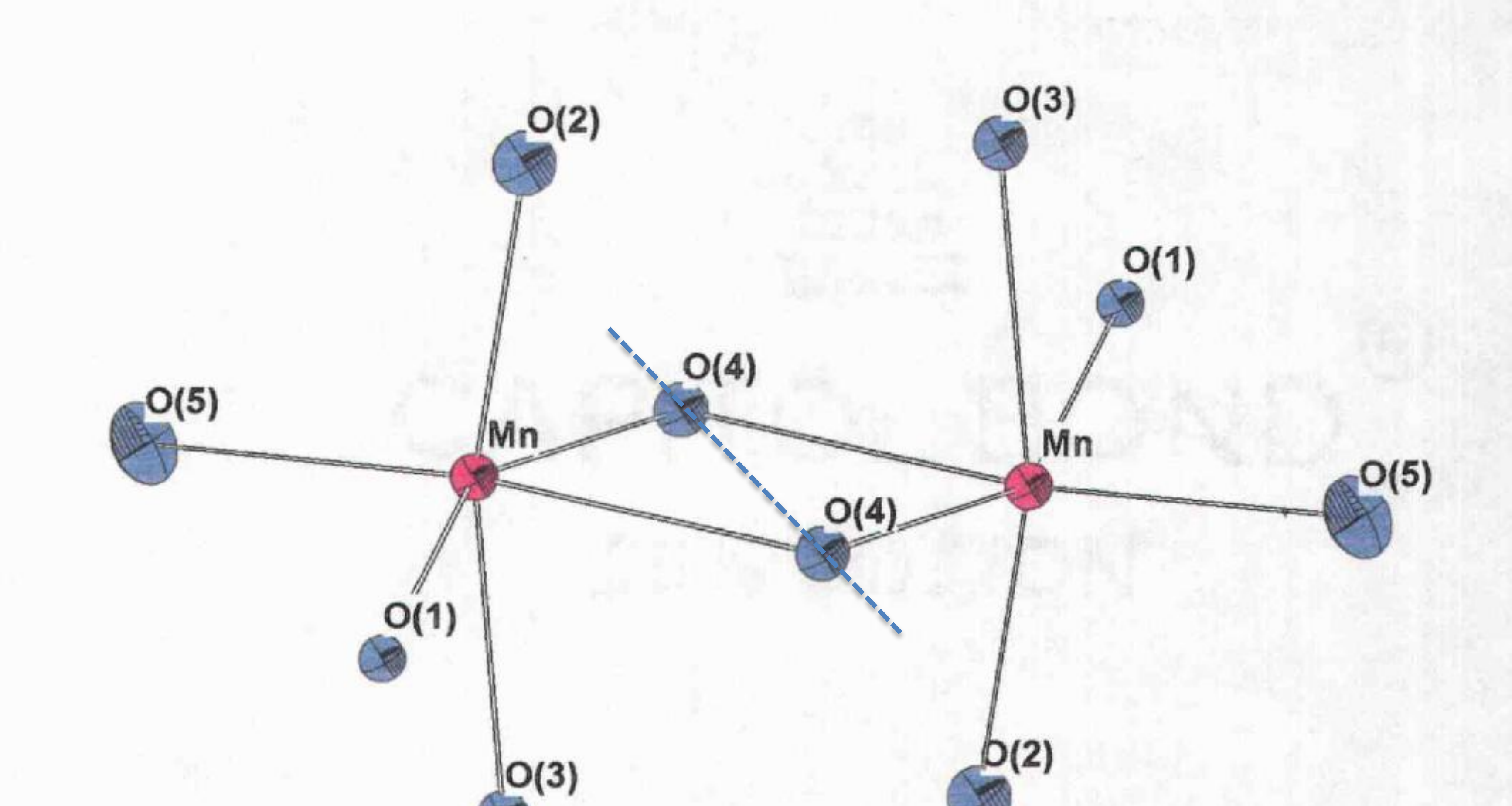

$BiCoPO_5$-structure

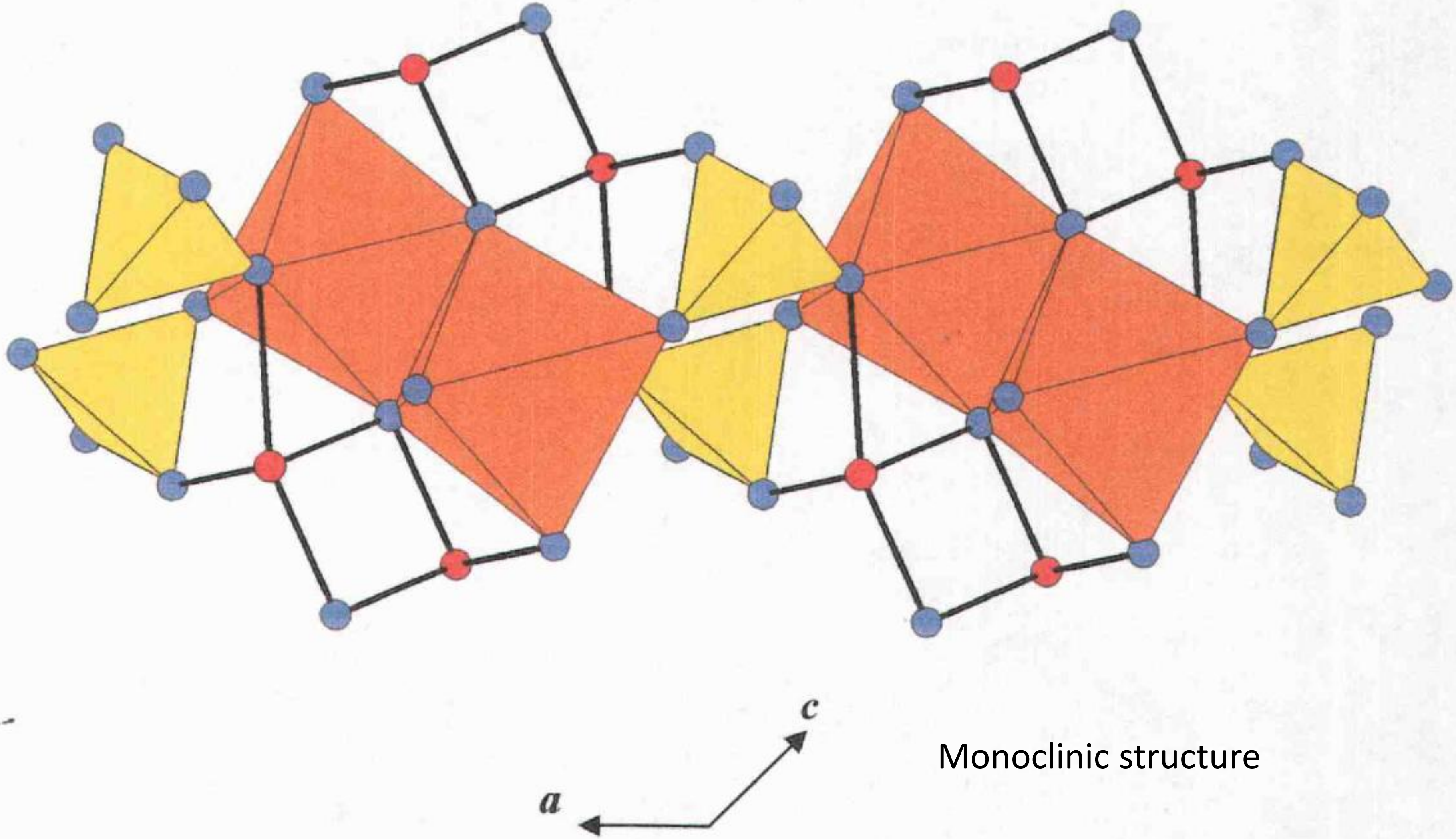

Monoclinic structure

Co^{2+} orbitals S=3/2

Co^{2+} $3d^7$-orbitals

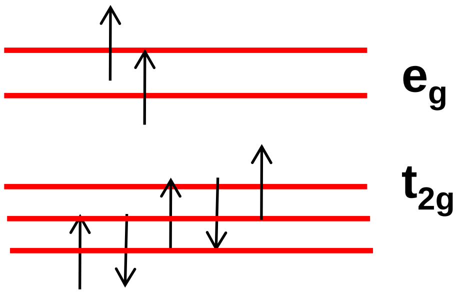

e_g $3z^2$-r^2, x^2-y^2

t_{2g} xy, xz, yz

Ni^{2+} $3d^8$-orbitals : S=1

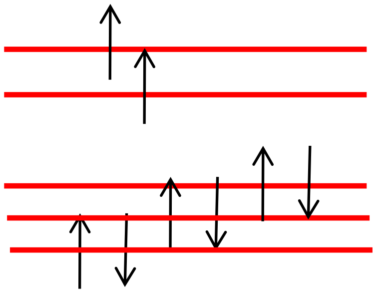

e_g

t_{2g}

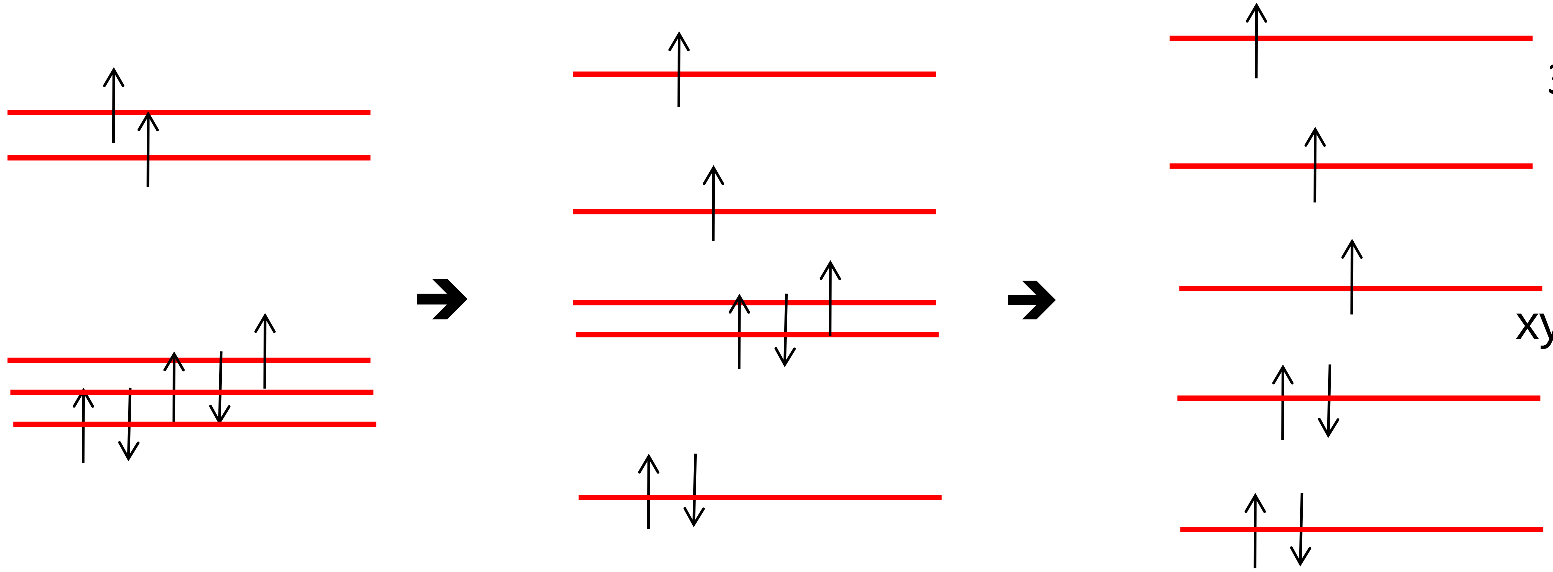

Δ_{CF}

➔

➔

$3z^2$-r^2

x^2-y^2

xy, xz, yz

Crystal field

Tetragonal distortions

Monoclinic distortions

Ni^{3+} 3d^7 orbitals S=3/2 High Spin

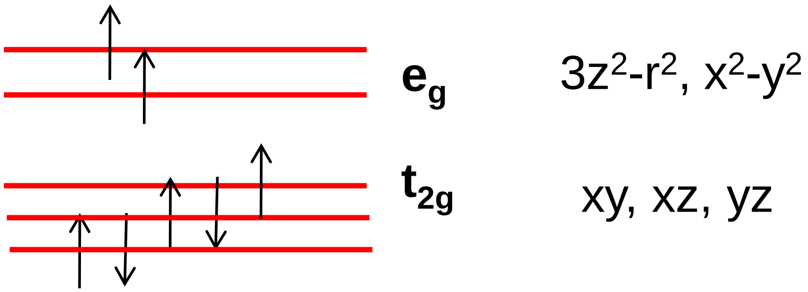

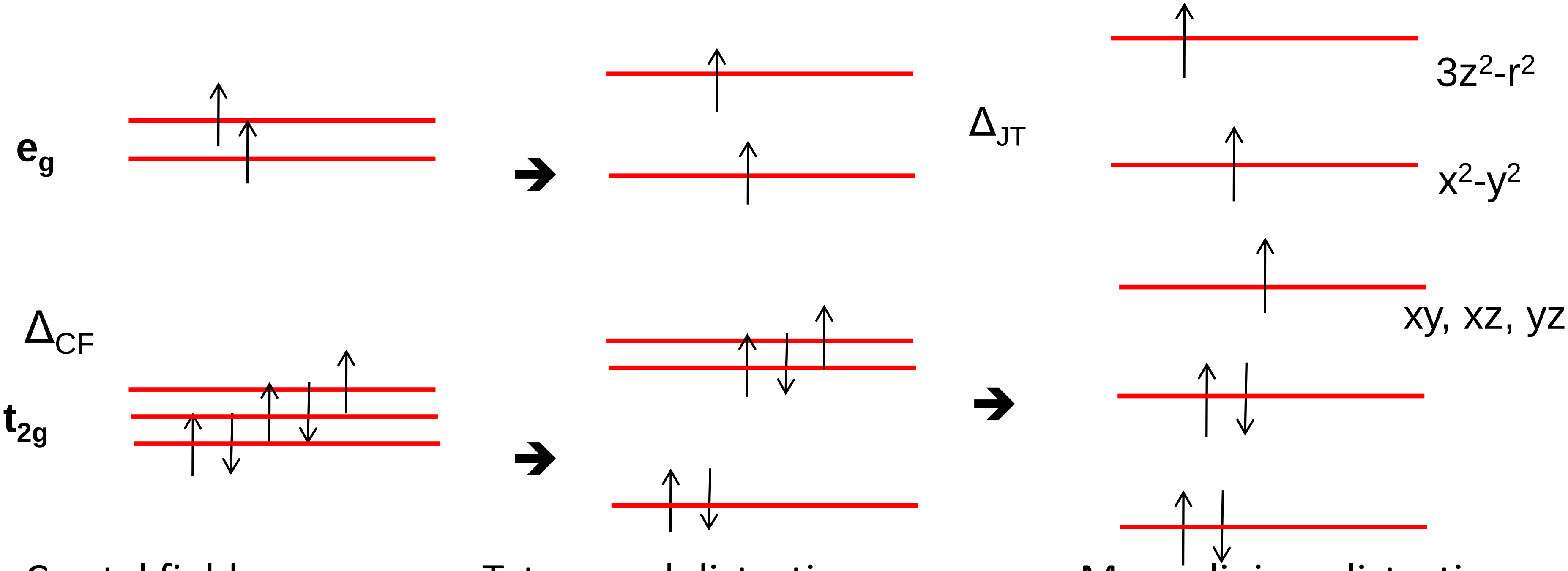

Crystal field Tetragonal distortions Monoclinic distortions

Ni^{3+} $3d^7$ orbitals S=1/2 Low Spin

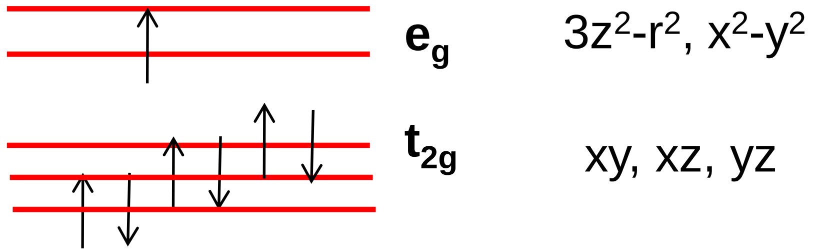

e_g $3z^2-r^2$, x^2-y^2

t_{2g} xy, xz, yz

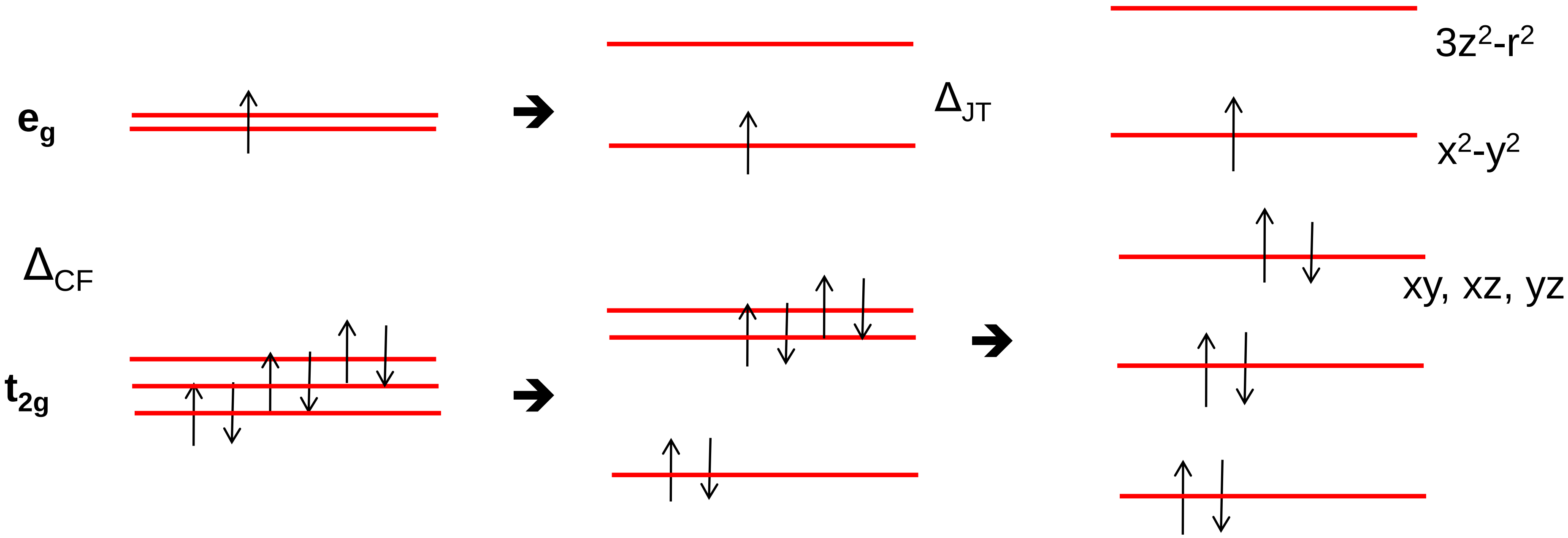

e_g

Δ_{CF}

t_{2g}

Δ_{JT}

$3z^2-r^2$

x^2-y^2

xy, xz, yz

\Crystal field

Tetragonal distortions

Monoclinic distortions

Ni^{2+} $3d^8$ orbitals $S=1$

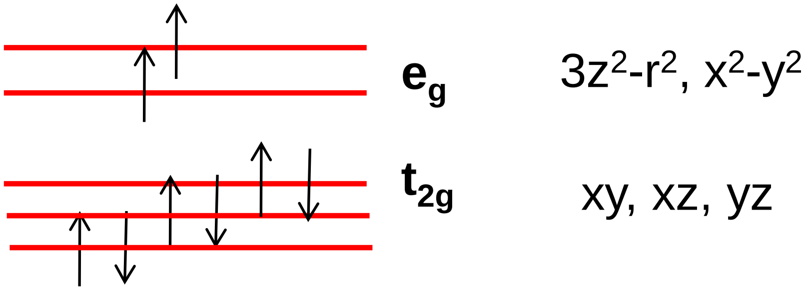

e_g $3z^2$-r^2, x^2-y^2

t_{2g} xy, xz, yz

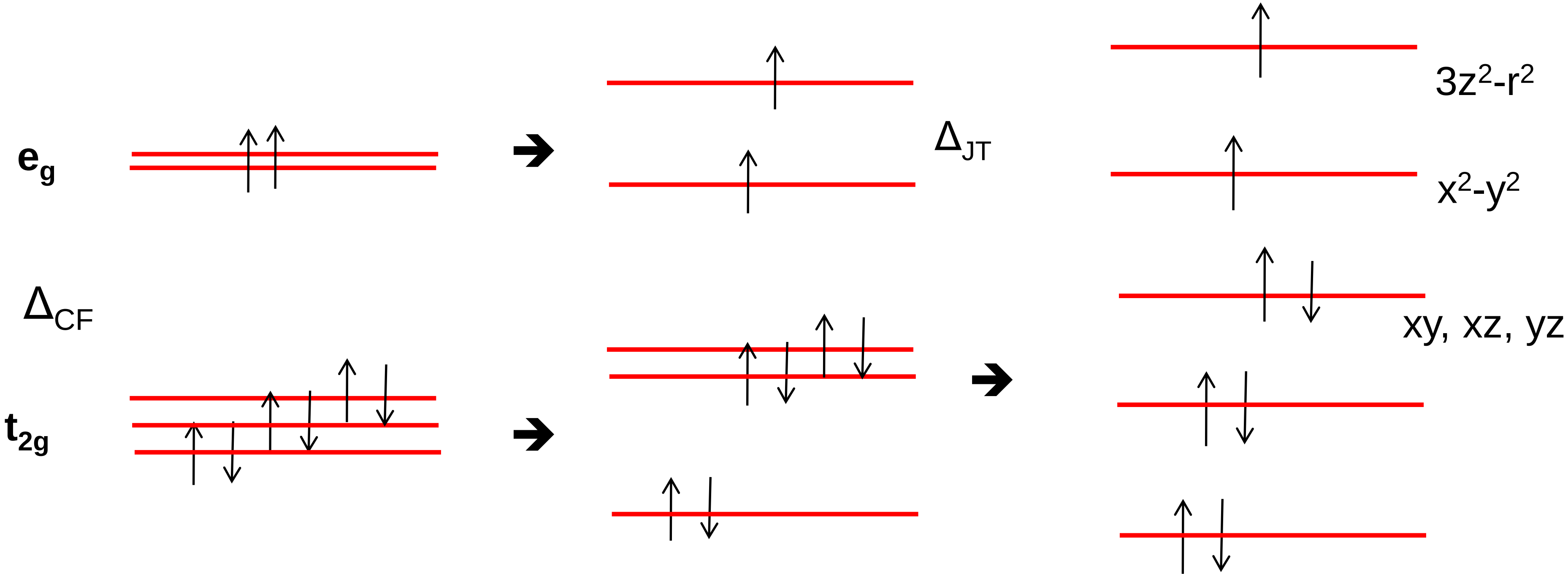

e_g

Δ_{CF}

t_{2g}

Δ_{JT}

$3z^2$-r^2

x^2-y^2

xy, xz, yz

\Crystal field Tetragonal distortions Monoclinic distortions

$BiCoPO_5$-magnetic structure

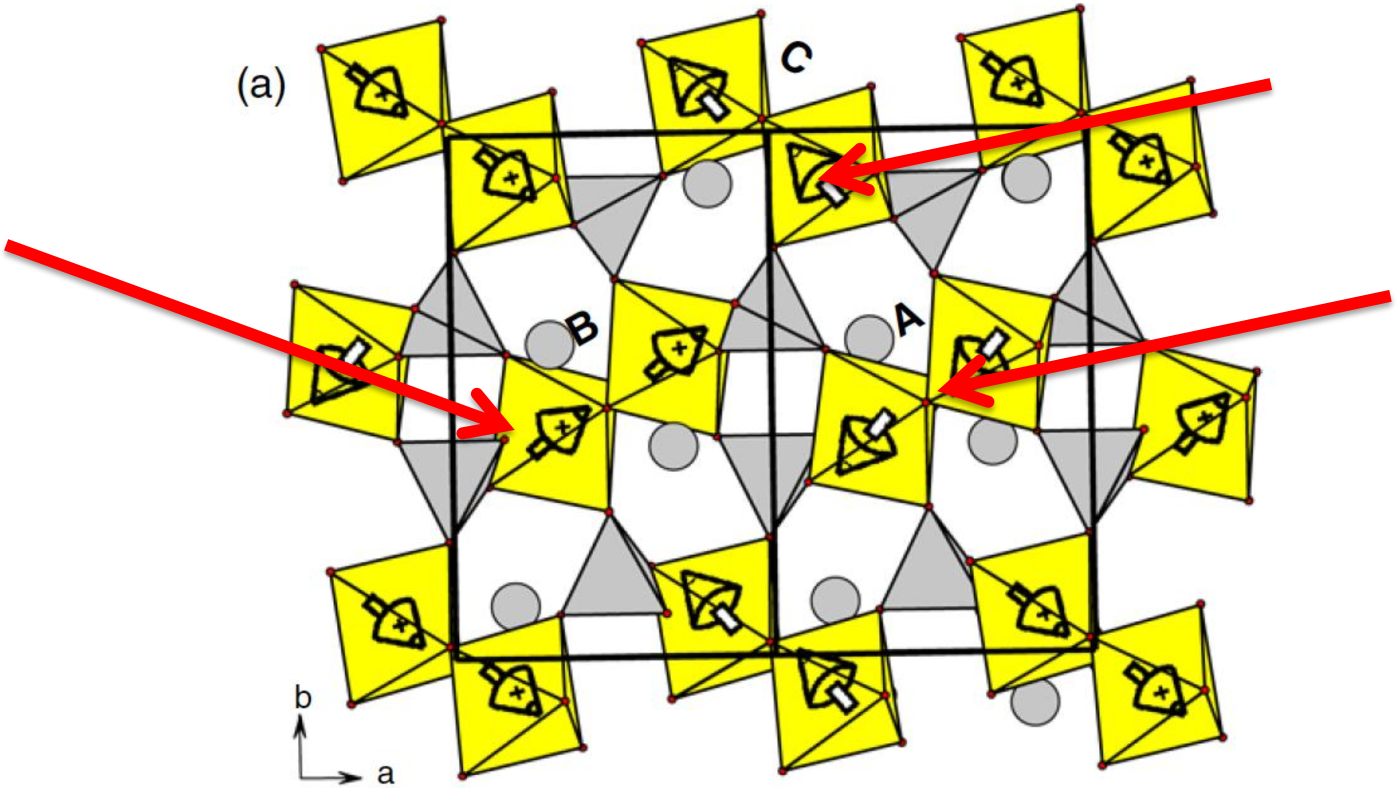

- monoclinic,- magnetic group P $2_{1/}$n (C_{2h}) has four irreducible 1 D representations: 4 spin config-orientations,
- Ni mag-moments nearly perpendicular to the a-b plane, Co - are not-collinear, close to the plane

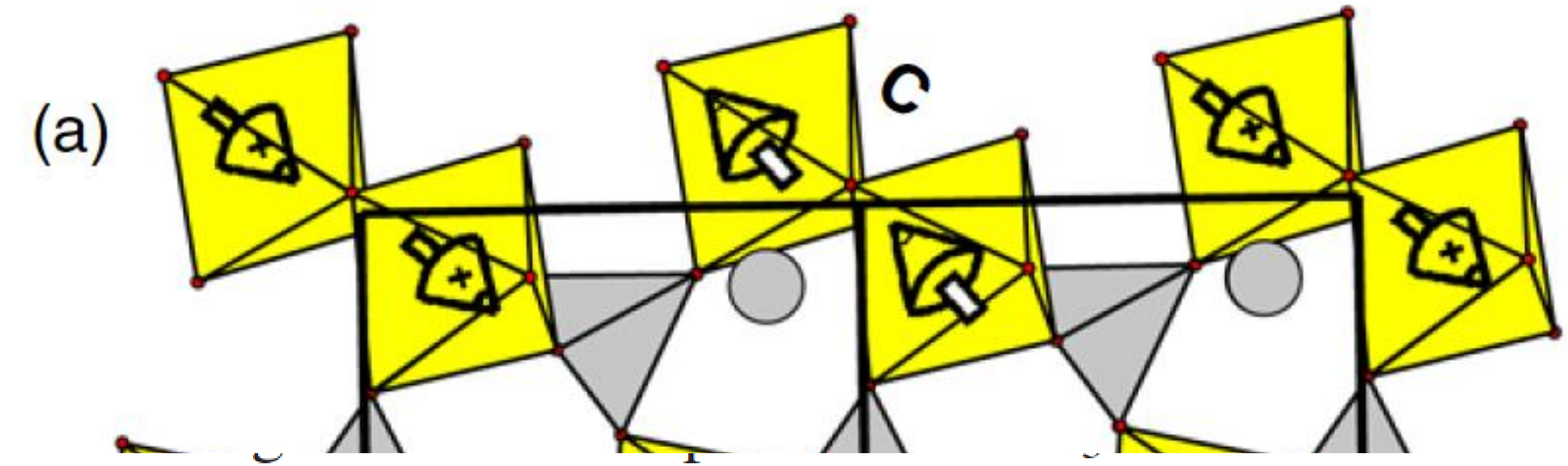

R_{magn} is 7.15% while $\mu\mathrm{Co}^{2+} = 3.52(3)\ \mu_{\mathrm{B}}$ that suggests an orbital contribution of $\sim 0.5\ \mu_{\mathrm{B}}$, in good agreement with the μ_{eff} value. In this case the structure is clearly non-collinear anymore according to the three components $\mathbf{M}_x > \mathbf{M}_y > \mathbf{M}_z$.

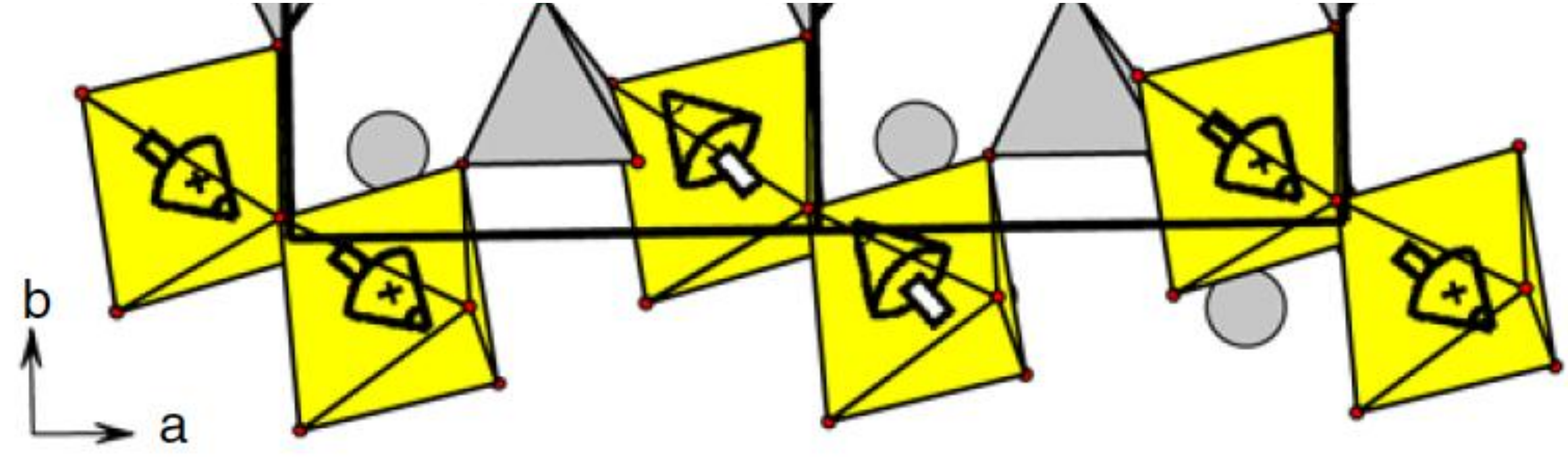

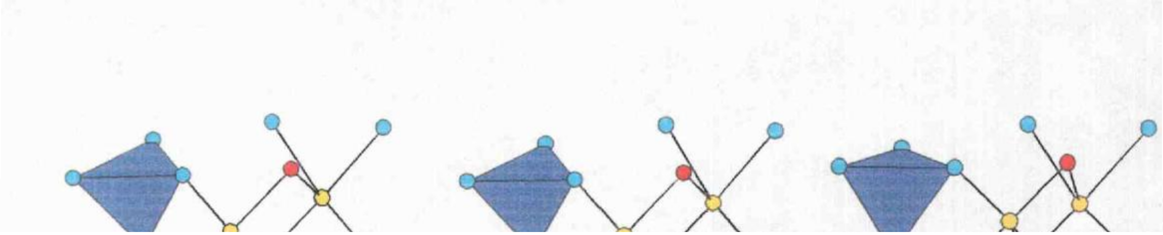

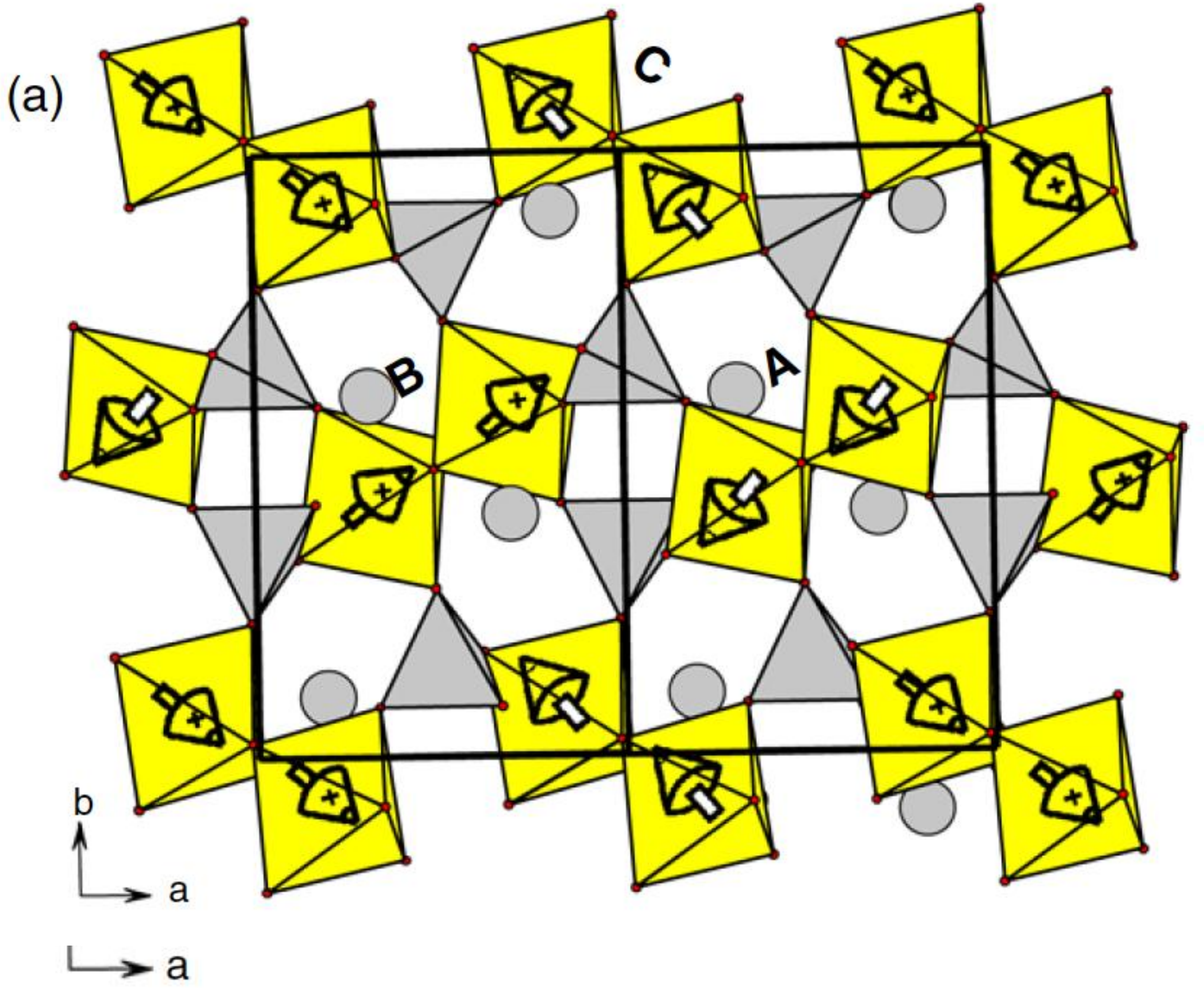

The

As)

Top view on AF magnetic chains in $BiCoPO_5$- each unit is a large spin ~7 μ_B .

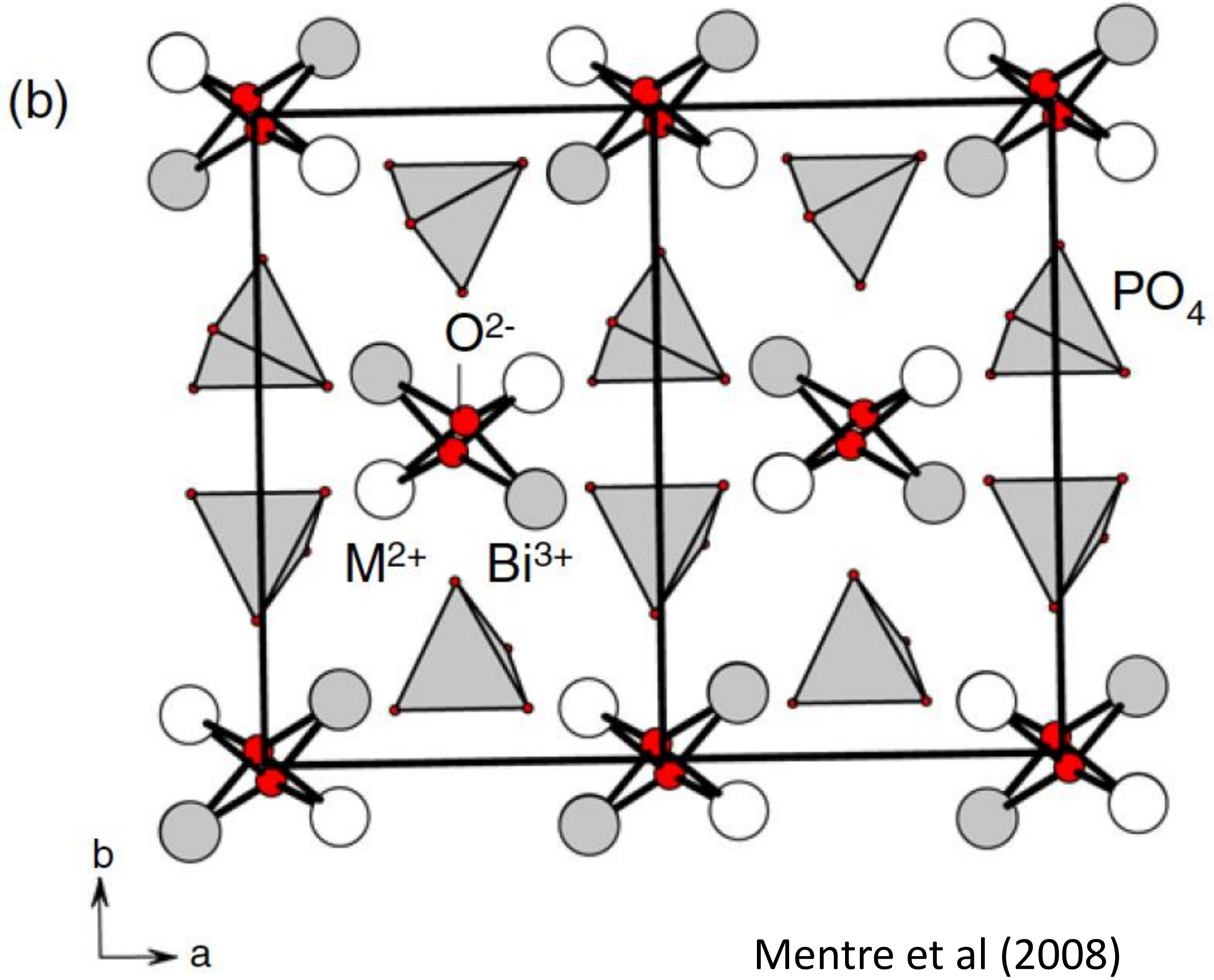

Mentre et al (2008)

More than 8 exchange parameters

$>J_{1}, J_{2}, J_{3}, J_{4}, J_{5}, J_{6}, J_{7}, J_{8}$

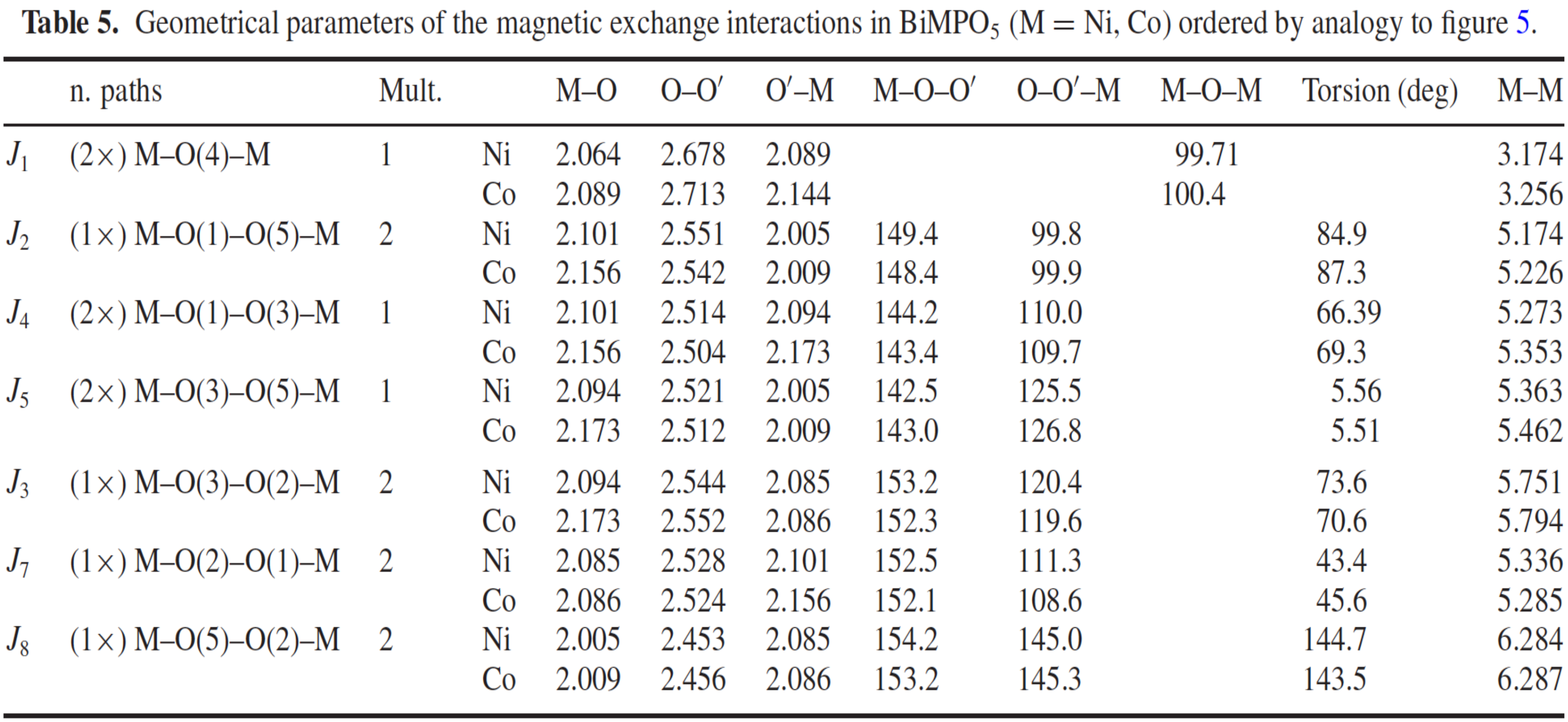

Table 5. Geometrical parameters of the magnetic exchange interactions in $BiMPO_5$ (M = Ni, Co) ordered by analogy to figure 5.

	n. paths	Mult.		M–O	O–O′	O′–M	M–O–O′	O–O′–M	M–O–M	Torsion (deg)	M–M
J_1	(2×) M–O(4)–M	1	Ni	2.064	2.678	2.089			99.71		3.174
			Co	2.089	2.713	2.144			100.4		3.256
J_2	(1×) M–O(1)–O(5)–M	2	Ni	2.101	2.551	2.005	149.4	99.8		84.9	5.174
			Co	2.156	2.542	2.009	148.4	99.9		87.3	5.226
J_4	(2×) M–O(1)–O(3)–M	1	Ni	2.101	2.514	2.094	144.2	110.0		66.39	5.273
			Co	2.156	2.504	2.173	143.4	109.7		69.3	5.353
J_5	(2×) M–O(3)–O(5)–M	1	Ni	2.094	2.521	2.005	142.5	125.5		5.56	5.363
			Co	2.173	2.512	2.009	143.0	126.8		5.51	5.462
J_3	(1×) M–O(3)–O(2)–M	2	Ni	2.094	2.544	2.085	153.2	120.4		73.6	5.751
			Co	2.173	2.552	2.086	152.3	119.6		70.6	5.794
J_7	(1×) M–O(2)–O(1)–M	2	Ni	2.085	2.528	2.101	152.5	111.3		43.4	5.336
			Co	2.086	2.524	2.156	152.1	108.6		45.6	5.285
J_8	(1×) M–O(5)–O(2)–M	2	Ni	2.005	2.453	2.085	154.2	145.0		144.7	6.284
			Co	2.009	2.456	2.086	153.2	145.3		143.5	6.287

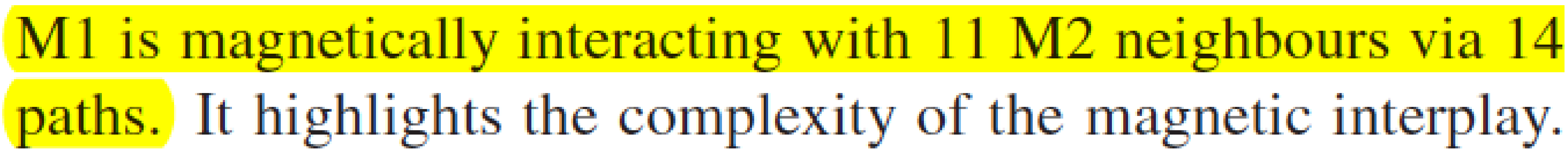

M1 is magnetically interacting with 11 M2 neighbours via 14 paths. It highlights the complexity of the magnetic interplay.

More than 8 exchange parameters

$>J_1, J_2, J_3, J_4, J_5, J_6, J_7, J_8$

J. Phys.: Condens. Matter **20** (2008) 415211

Table 5. Geometrical parameters … ure 5.

	n. paths	M	M–M
J_1	(2×) M–O(4)–M	1	3.174 3.256
J_2	(1×) M–O(1)–O(5)–M	2	5.174 5.226
J_4	(2×) M–O(1)–O(3)–M	1	5.273 5.353
J_5	(2×) M–O(3)–O(5)–M	1	5.363 5.462
J_3	(1×) M–O(3)–O(2)–M	2	5.751 5.794
J_7	(1×) M–O(2)–O(1)–M	2	5.336 5.285
J_8	(1×) M–O(5)–O(2)–M	2	6.284 6.287

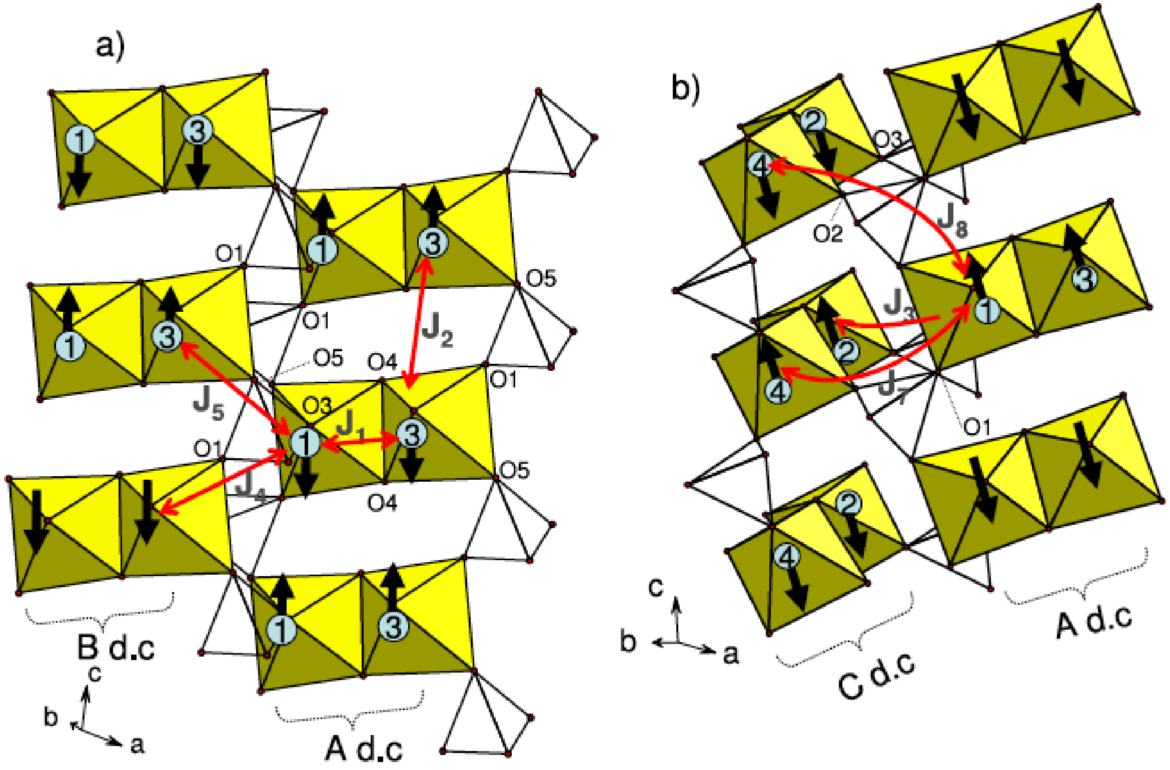

Figure 5. Representation of the exchange paths between the Ni^{2+} cations. (a) J_1, J_2 intra double chains (d.c.) and J_4, J_5 inter A–B d.c. exchange interactions. (b) J_3, J_7, J_8 inter A–C d.c. exchange interactions. A, B and C entities are defined in figure 2(a).

More than 8 exchange parameters

$>J_{1,} J_{2,} J_{3,} J_{4,} J_{5,} J_{6,} J_{7,} J_8$

J. Phys.: Condens. Matter **20** (2008) 415211

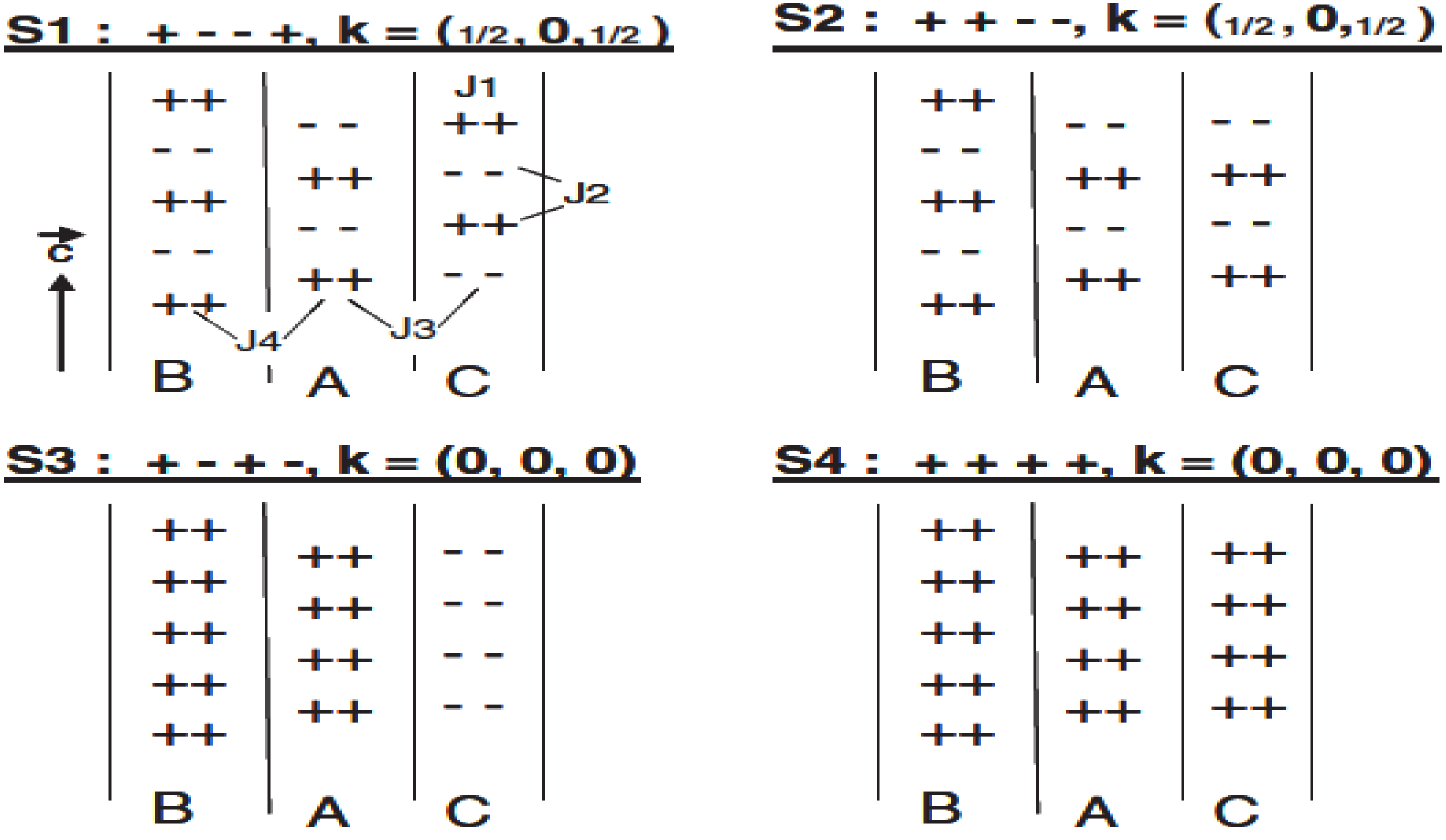

Figure 6. Scheme of the magnetic orderings between double chains A, B and C associated with the structures S1–S4. In this figure, A, B and C, are arranged by analogy to figures 5(a) and (b).

More than 8 exchange parameters $>J_1, J_2, J_3, J_4, J_5, J_6, J_7, J_8$: *Phase Diagram?*

J. Phys.: Condens. Matter **20** (2008) 415211 O Mentre *et al*

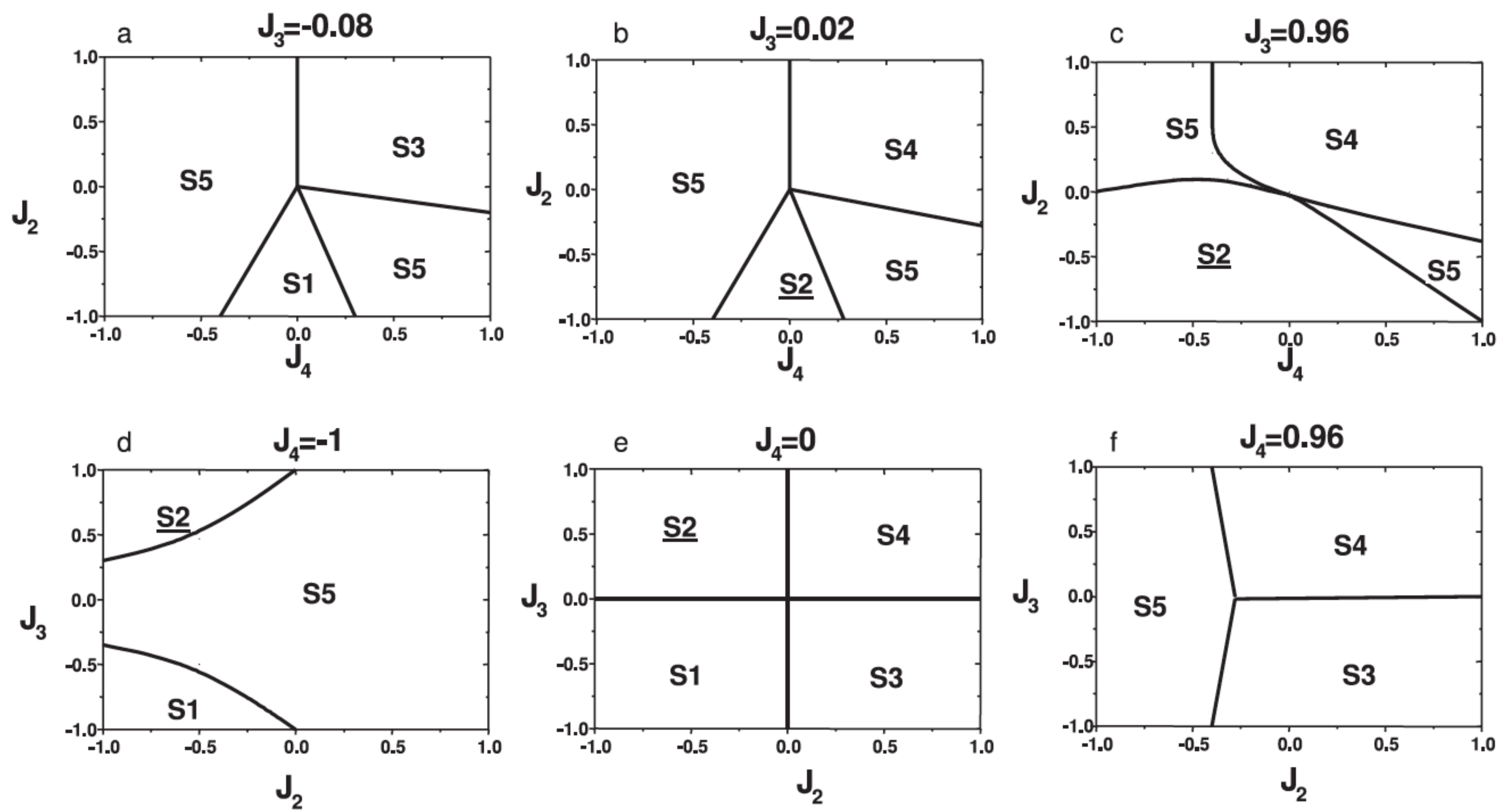

Figure 7. (a)–(f) Maps of the magnetic phase diagram for $BiMPO_5$ (M = Ni, Co). The exchange constant J_1 has been taken as unity ($J_1 = 1$).

$BiCoPO_5$-structure

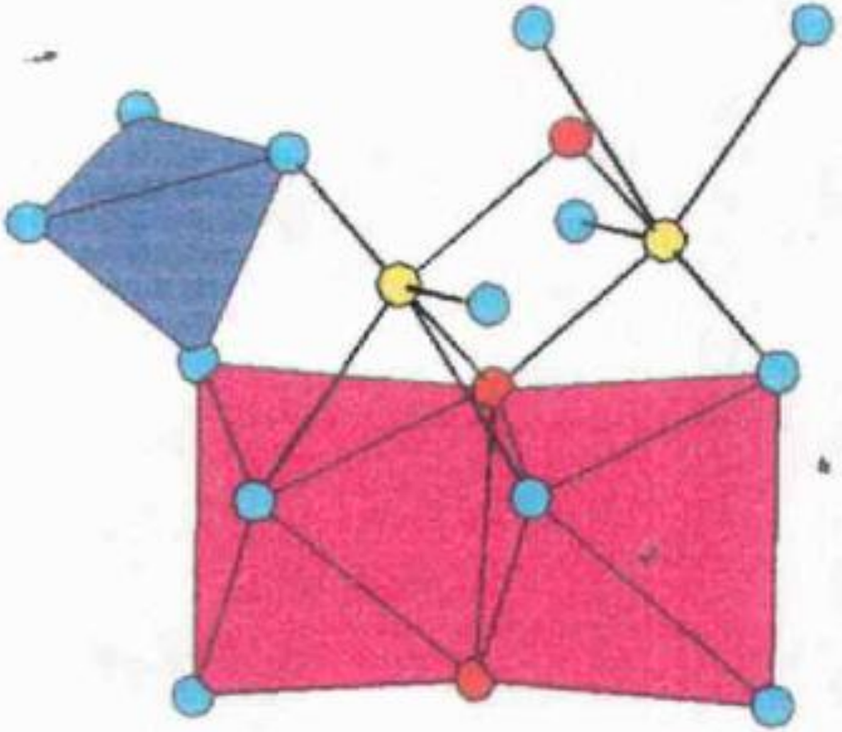

$BiCoPO_5$

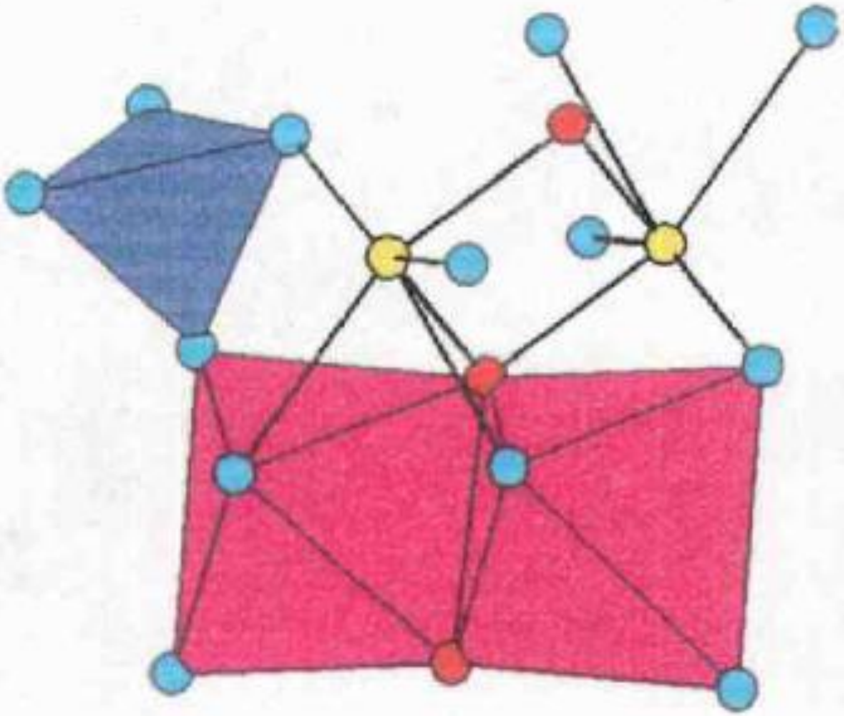

$BiNiPO_5$

General $BiCoPO_5$ like-structures

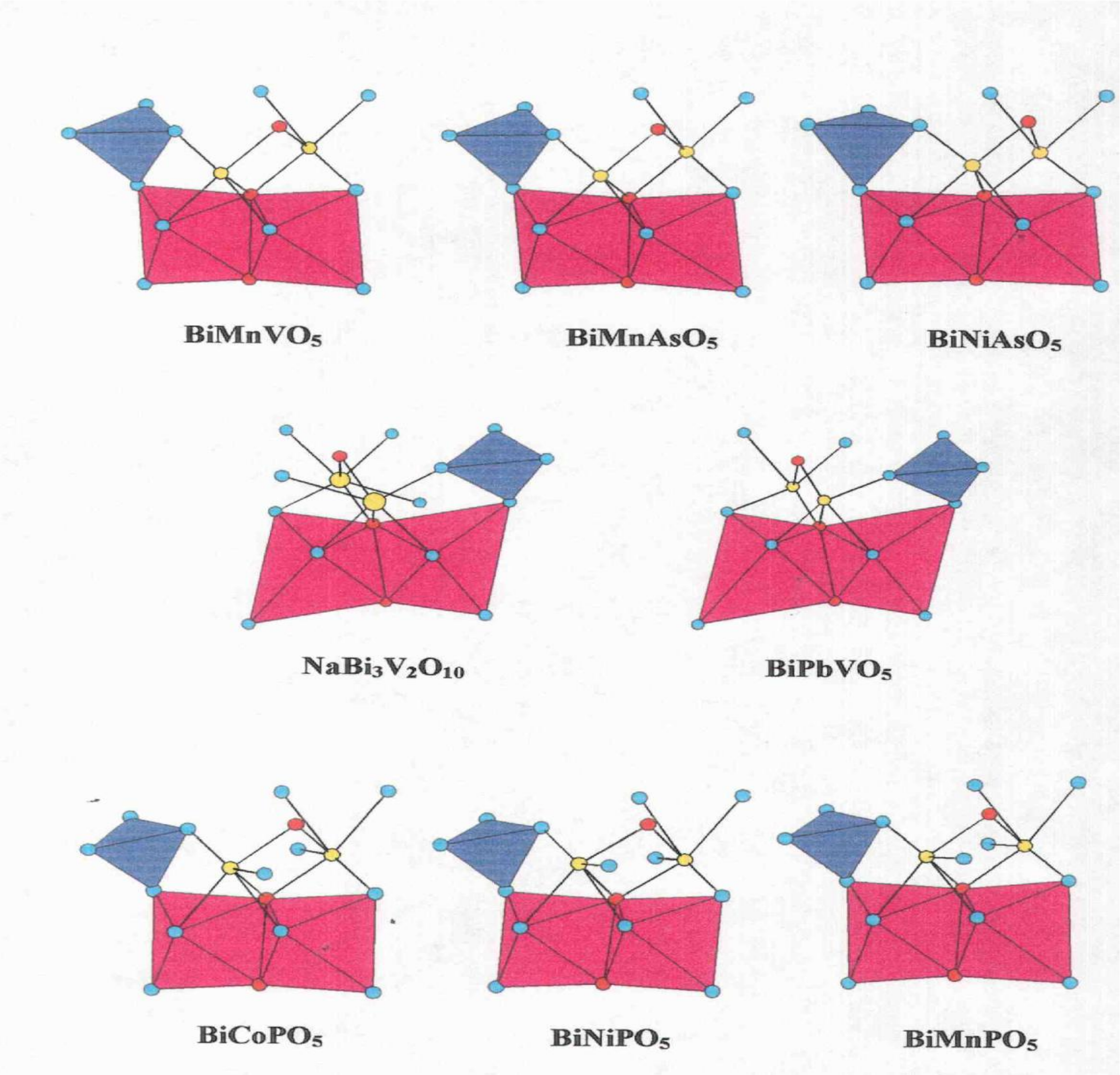

Specific Heat of BiCoP O_5
II Order Phase Transition

E. Mathews et al. / Solid State Communications 154 (2013) 56–59

$$C_{ph}(T) = 9R \sum_{n=1}^{n=2} c_n \left(\frac{T}{\theta_D^{(n)}} \right)^3 \int_0^{\theta_D^{(n)}/T} \frac{x^4 e^x}{(e^x - 1)} dx$$

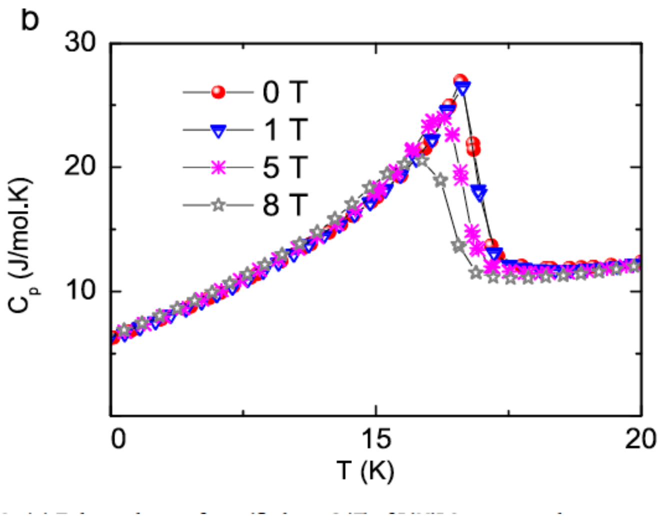

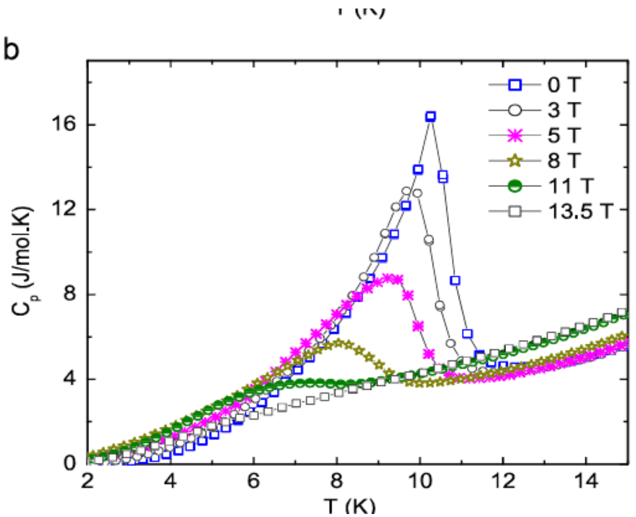

Succeptibility of BiCoP O_5
Curie-Weiss like AF state

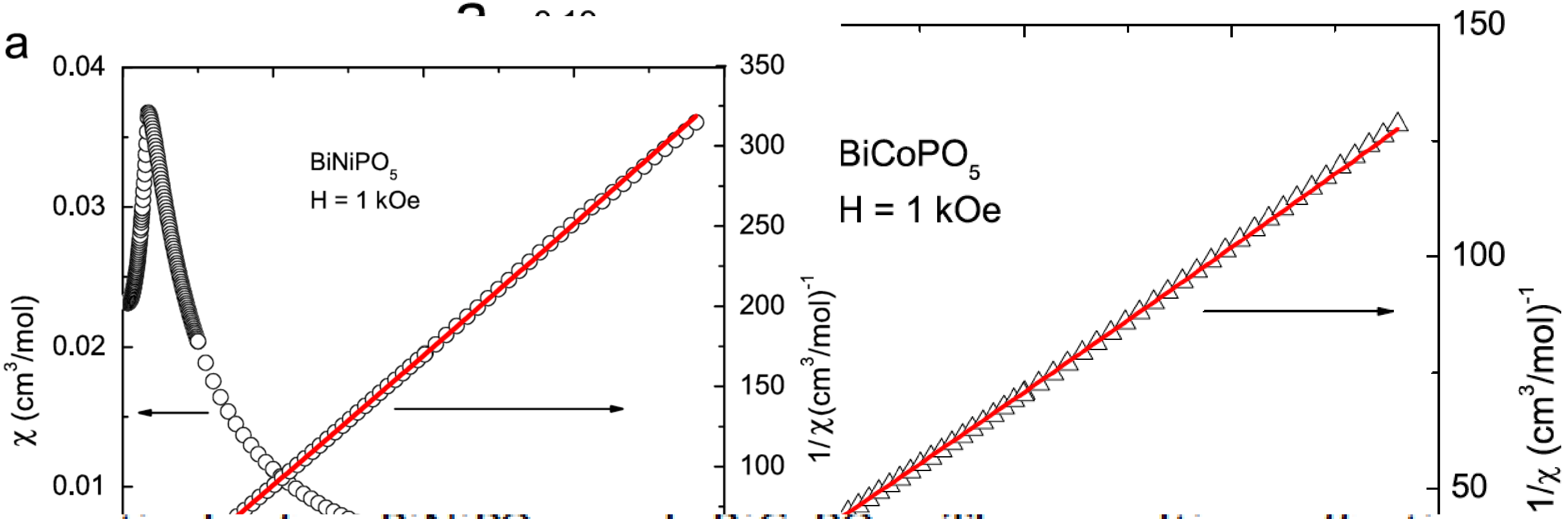

respectively for $BiNiPO_5$ and $BiCoPO_5$. The resulting effective moment μ_{eff} was calculated to be 3.1 μ_B and 5.2 μ_B for $BiNiPO_5$ and $BiCoPO_5$, respectively. For $BiNiPO_5$, the calculated μ_{eff} is in close agreement with the spin-only value of 2.83 μ_B expected for Ni^{2+} ($S=1$) while for $BiCoPO_5$, it is much higher than the expected spin only value 3.9 μ_B for Co^{2+} ($S=3/2$). Such an enhanced value of μ_{eff}

Comparison with traditional AF

The antiferromagnetic axis along which the sublattice magnetizations lie is determined by magnetocrystalline anisotropy

Response below T_N depends on the direction of H relative to this axis.

No shape anisotropy (no demagnetizing field)

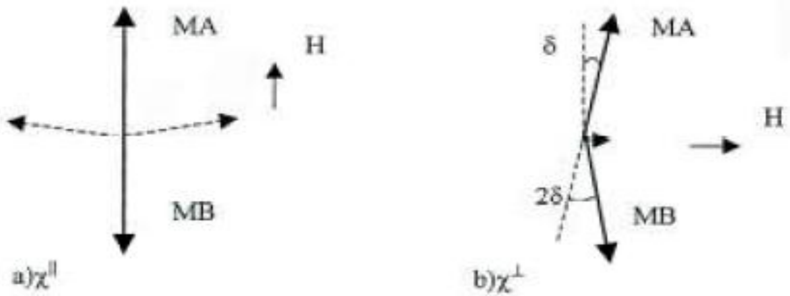

Calculation of the susceptibility of antiferromagnet below T_N. In a) the
nes show the configuration after a spin flop. The phase diagram shows the bel
lose to T_N.

$$\chi_{||} = N m^2 \mathcal{B}_J(x_0)/[k_B T + n n'_W$$

x_0 is $\mu_0 m n_W M/k_B T$

$$\chi_{\perp} = 1/n_W$$

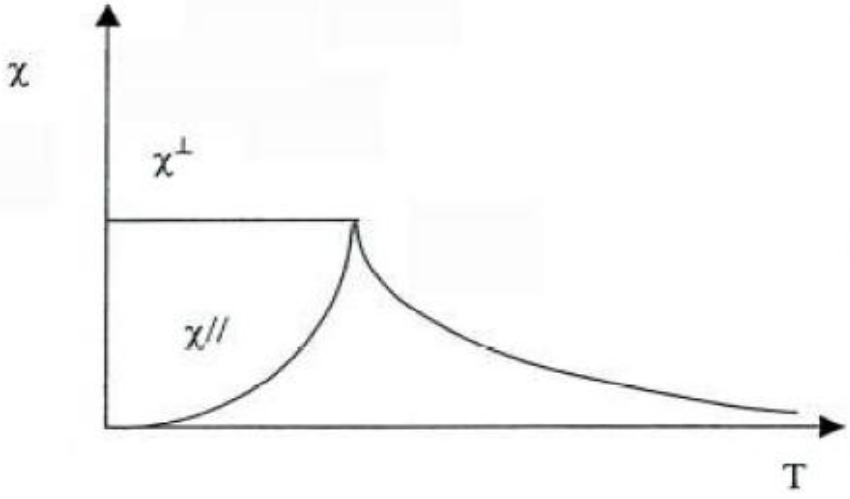

Parallel and perpendicular susceptibility of an antiferromagnet

Phase Diagram of $BiCoPO_5$

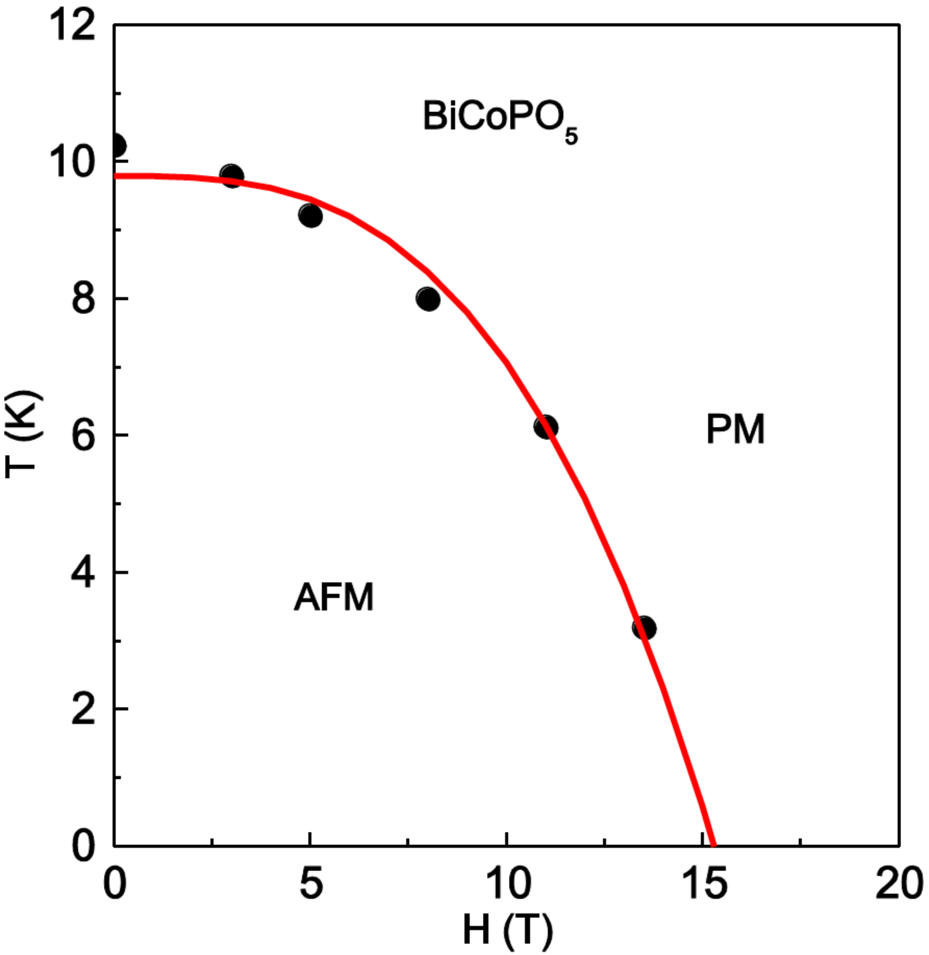

From $C_p(T)$ data

Mathews et al
SSC, (2013)

Fig. 5. $H-T$ phase diagram of $BiCoPO_5$ obtained from specific heat measurement
Solid line is the fit using the formula $H=H_c(1-T/T_N)^\beta$ with $T_N \approx 9.8$ K, $H_c \approx 15.3$
and $\beta=1/3$.

NO features other than AF-PM transition!!!!

The thermodynamics of complex magnetic such as $BiCoPO_5$

- *Strong and Long-Range Interaction between spins and orbital moments*
- *Existing model has >8 exchange parameters*
- *The magnitude of the moments changes, e. g. Low vs High Spin states in Co^{2+} with T*

- *Due to frustration->The glassy characters and the number states increases exponentially*
- *=>May have fractal energy spectra and the set of orbital magnetic moments*

To solve it is a hopeless task

We were looking for the help from???? In BLACK HOLE

Model for $\mathrm{BICoPO_5}$ and $\mathrm{SrCo_2V_2O_8}$

The low-energy dynamics of the large-spin one-dimensional Heisenberg Antiferromagnet is found to be the O(3) nonlinear sigma model. (Haldane , 1983)

$$L_i = \frac{2}{\hbar S}(\nabla_\mu \mathbf{n_i})^2$$

Provided that the vector field n(x) satisfy

$$(\mathbf{n_i})^2 = 1$$

Single Haldane Chain as Landau-Ginzburg-Wilson model

$$L_i = \frac{2}{\hbar S}(\nabla_\mu \mathbf{n_i})^2 + \frac{J}{8}((\mathbf{n_i})^2 - 1)^2,$$

When J S >> 1 it is sigma model

How can we describe interaction between the Haldane chains?! :

$$L_{ij} = -\frac{k}{2} \sum_{<i,j>,x,y} J(x,y)\mathbf{n_i}(\mathbf{x})\mathbf{n_j}(\mathbf{y})),$$

Model for BICoPO$_5$ and SrCo$_2$V$_2$O$_8$

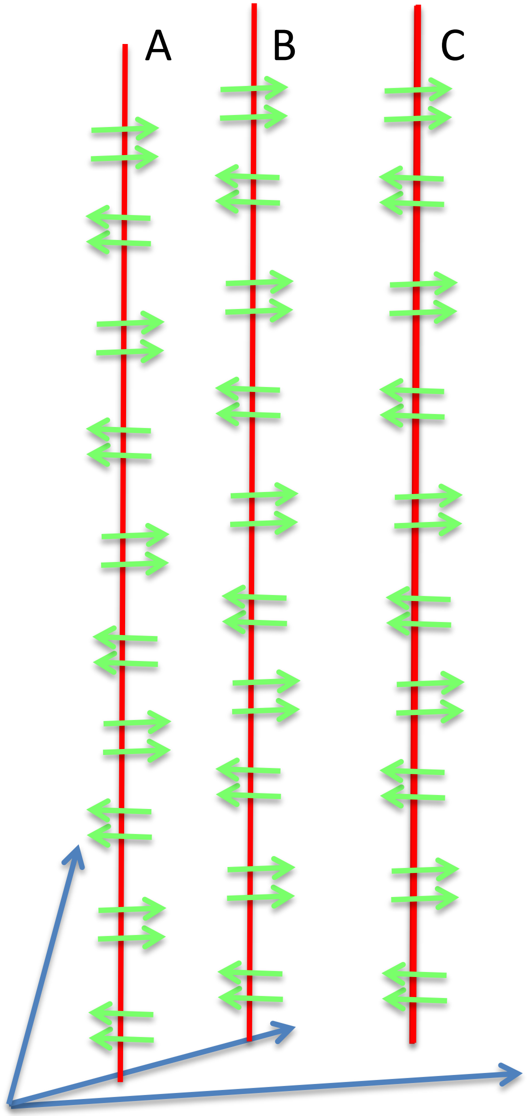

- System consisting of 1 D AF chains with large S
- The low-energy dynamics of the large-spin model
- one-dimensional Heisenberg Antiferromagnet as the O(3) nonlinear sigma model. (Haldane , 1983)

$$H = g\sum_{i} (\nabla n_i)^2 + \sum_{ij} n_i n_j$$

General relativity “=“ quantum field theory

Gravity

Quantum fields

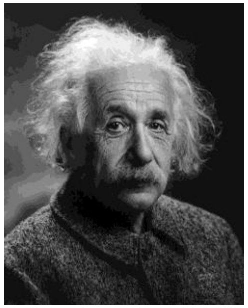

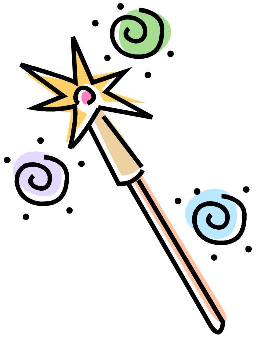

Maldacena 1997

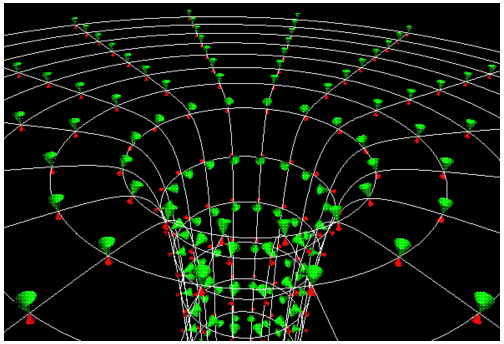

=

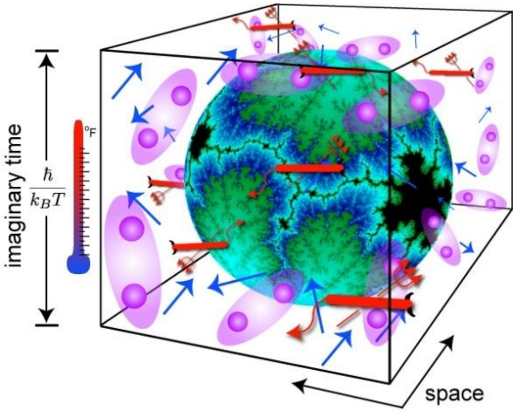

General relativity “=“ quantum field theory

Gravity

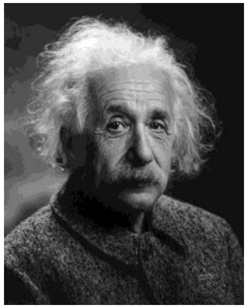

In Anti-de-Sitter space

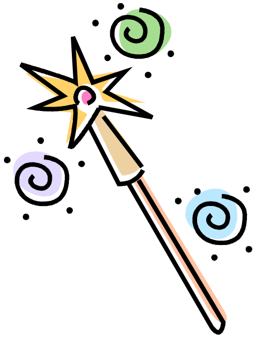

Maldacena 1997

=

AdS/CFT correspondence

Quantum fields

When they are conformal = quantum critical

Gravity helps for quantum world by holography

Einstein Universe “AdS”

Quantum field world “CFT”

lives on boundary

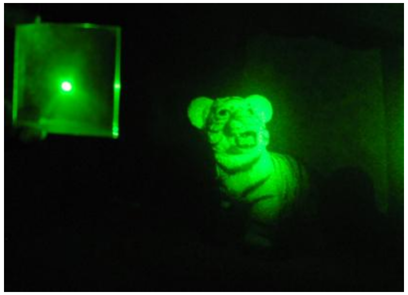

‘t Hooft Susskind
holographic principle

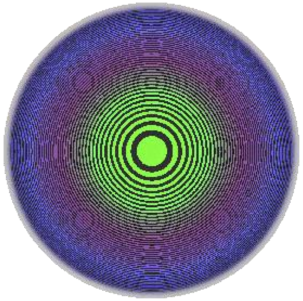

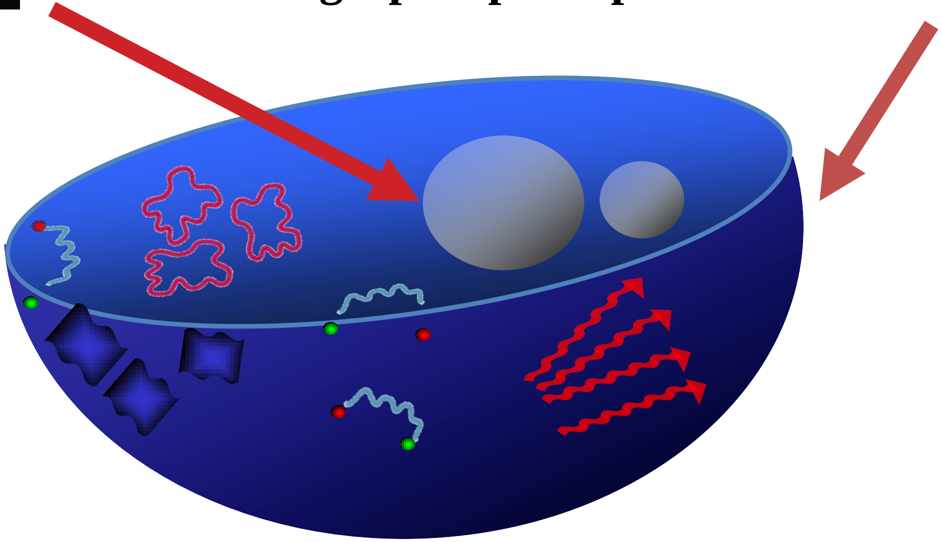

Classical world,
weakly
interacting

Very quantized,
strongly
interacting

AdS/CFT correspondence: String theory Magic!

d-dim. gauge theory
/ conformal field theory

⟷

(d+1)-dim string theory
/ gravity theory

One extra dimension,
hence the name
“Holography”

Maldacena

Witten, Gubser,Klebanov,Polyakov

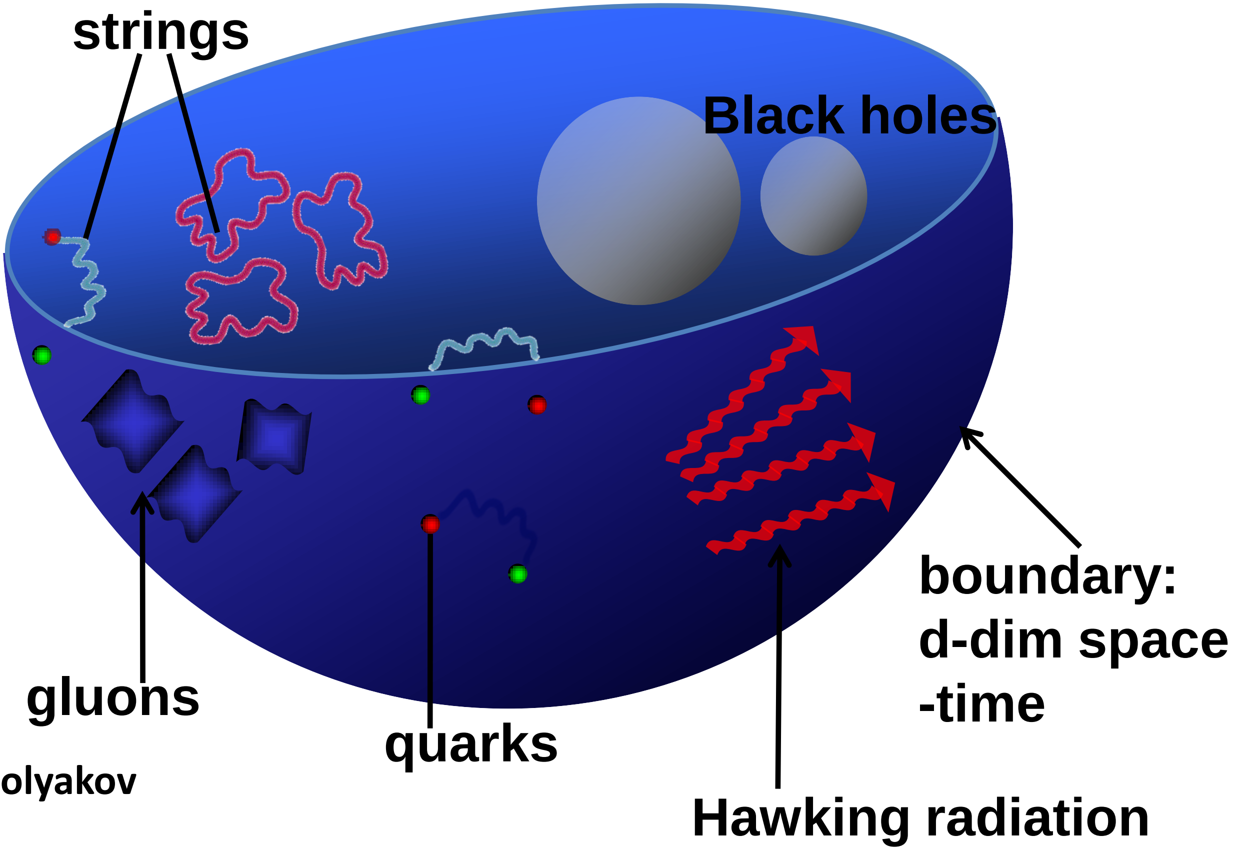

The bulk: Anti-de Sitter space

Extra radial dimension of the bulk <=> scaling "dimension" in the field theory

Bulk AdS geometry = **scale invariance of the field theory= scaling in phase transition=critical indices**

$$dr^2 = -F(r)dt^2 + \frac{dr^2}{F(r)} + r^2(d\theta^2 + \sin^2\theta d\phi^2)$$

$$F(r) = -\Lambda r^2 + 1, \qquad \Lambda < 0$$

The black hole is the heater

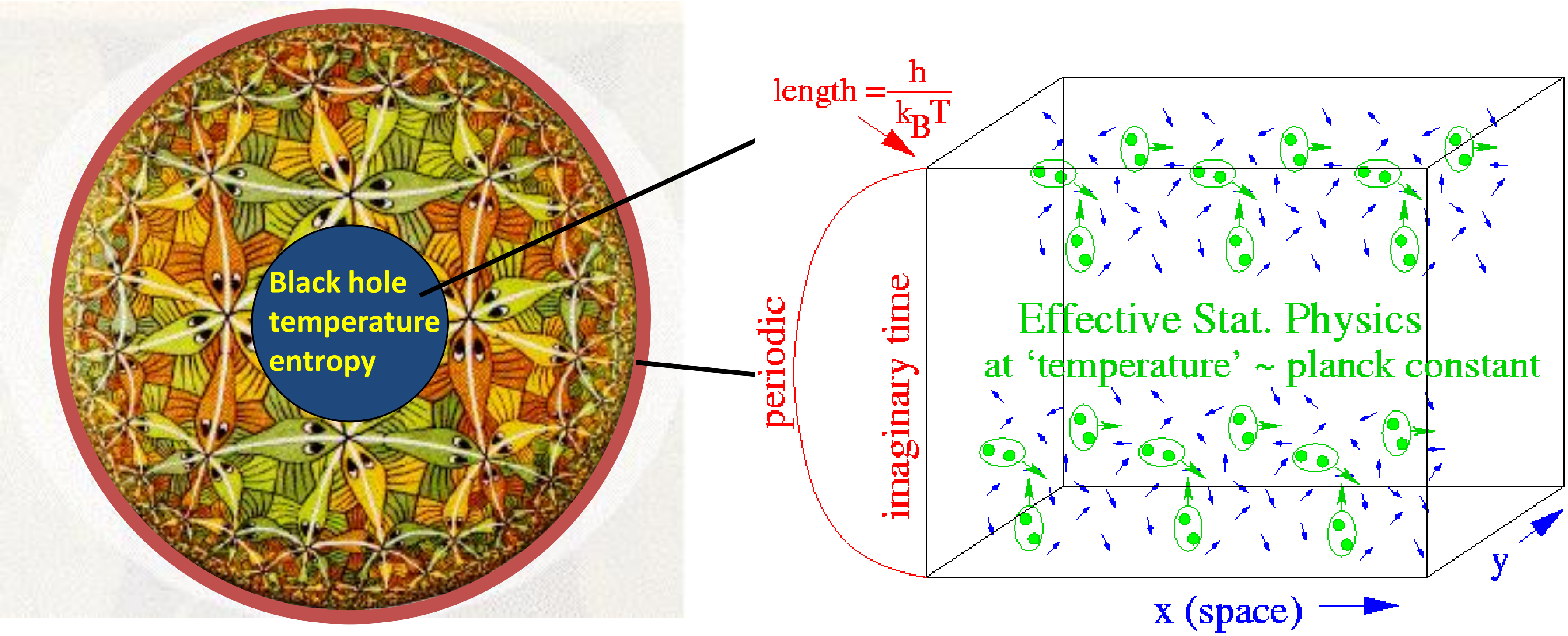

GR in Anti de Sitter space

$$dr^2 = -F(r)dt^2 + \frac{dr^2}{F(r)} + r^2(d\theta^2 + \sin^2\theta d\phi^2)$$

$$F(r) = -\Lambda r^2 + 1 - \frac{GM}{r}$$

Quantum-critical fields on the boundary:

- at the Hawking temperature

- entropy = black hole entropy

Model for BICoPO$_5$ and SrCo$_2$V$_2$O$_8$

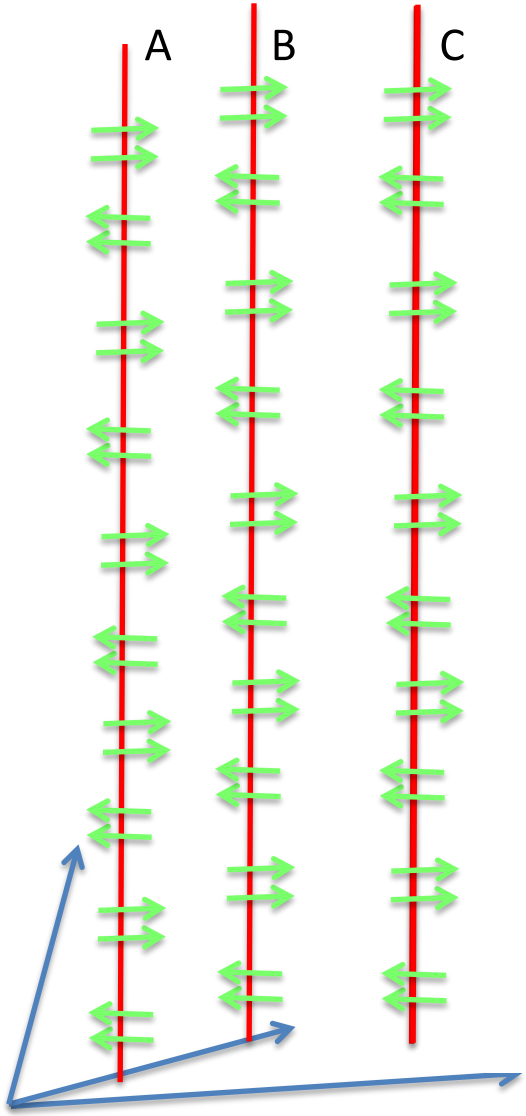

- We start with Haldane O(3) nonlinear sigma chains($n^2=1$):

$$H=\frac{2}{\square S}\sum_i(\nabla n_i)^2+k\sum_{ij}n_i n_j$$

- Then we would like to introduce quantum fields
- Like Landau-Ginzburg-Wilson

$$L_i=\frac{2}{\hbar S}(\nabla_\mu \mathbf{n_i})^2+\frac{J}{8}((\mathbf{n_i})^2-1)^2,$$

The thermodynamics of BiCoPO$_5$ is encoded into the Anti de Sitter (AdS) space with the black hole in the centre

$$S = \frac{1}{2\kappa^2}\int d^4x\sqrt{-g}\left[R + 6/L^2 - F^{\mu\nu}F_{\mu\nu} + \lambda^2(L_1 + L_2 + L_{12})\right],$$

$$L_{(a)} = -\frac{1}{4}\nabla^\mu M^{(a)\nu\tau}\nabla_\mu M^{(a)}_{\nu\tau} - \frac{1}{4}m^2 M^{(a)\mu\nu}M^{(a)}_{\mu\nu} - \frac{1}{2}M^{(a)\mu\nu}F_{\mu\nu} - \frac{1}{8}JV(M^{(a)}_{\mu\nu})$$

$$V(M^{(a)}_{\mu\nu}) = M^{(a)\mu}{}_{\nu}M^{(a)\nu}{}_{\tau}M^{(a)\tau}{}_{\sigma}M^{(a)\sigma}{}_{\mu},\ a = 1, 2$$

$$L_{12} = -\frac{k}{2}M^{(1)\mu\nu}M^{(2)}_{\mu\nu},$$

Black Hole

$$ds^2 = r^2(-f(r)dt^2 + dx^2 + dy^2) + \frac{dr^2}{r^2 f(r)},$$

$$f(r) = 1 - \frac{1 + \mu^2 + B^2}{r^3} + \frac{\mu^2 + B^2}{r^4}.$$

Temperature of black hole: $T = \frac{1}{4\pi}(3 - \mu^2 - B^2).$

The triumph: gravitational encoding of all thermal physics!

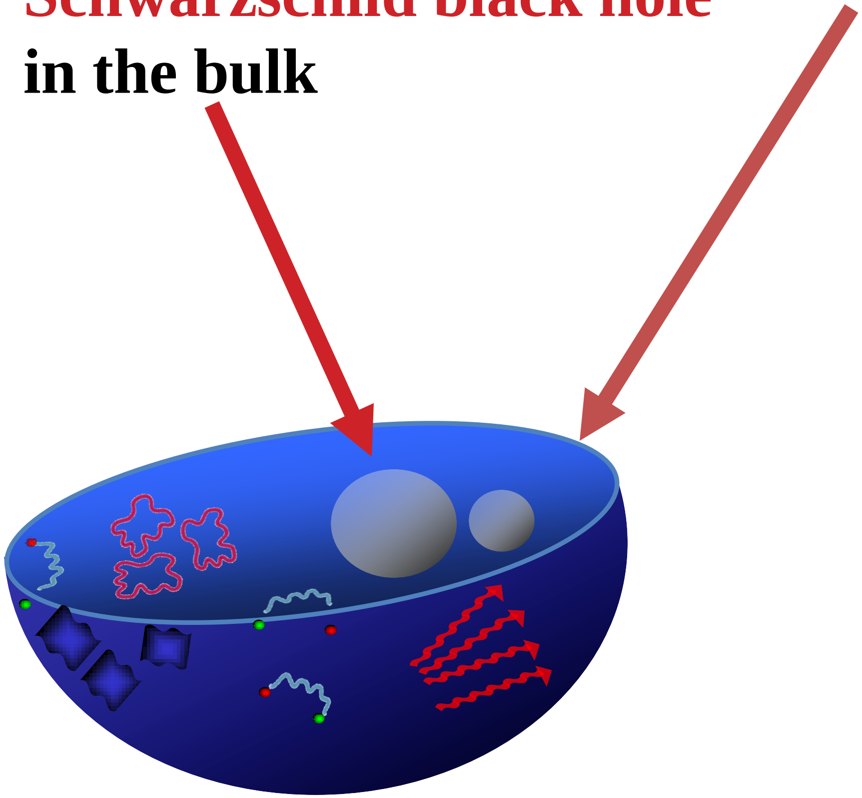

Schwarzschild black hole in the bulk

Boundary: the emergence theories of finite temperature matter.

- **All of thermodynamics!** **Caveat: phase transitions are mean field (large N limit).**

- **Precise encoding of Navier-Stokes hydrodynamics!** **Right now used to debug complicated hydrodynamics (e.g. superfluids).**

- **For special “Planckian dissipation” values of parameters (quantum criticality in HTSC):**

J. Zaanen et al , Nature, Science 2010 ,...
FVK, M. Saarela (2015)

$$\tau_\hbar = const.\frac{\hbar}{k_B T}, \quad const. = O(1)$$

Equation of Motion in AdS space

$$\nabla^2 M^{(a)}_{\mu\nu} - m^2 M^{(a)}_{\mu\nu} - k M^{(b)}_{\mu\nu} - J {M^{(a)}_{\mu}}^{\delta} {M^{(a)}_{\delta}}^{\tau} M^{(a)}_{\tau\nu} - F_{\mu\nu} = 0$$

- Separate into two polarisation fields: $M^1_{\mu\nu}$ and $M^2_{\mu\nu}$
- *Each is similar to the tensor* $F_{\mu\nu}$

- $M^1_{\mu\nu}$ is the polarisation quantum field associated with magnetisation of first sub-lattice*;*
- $M^2_{\mu\nu}$ -- is for the second one

- Tensor field is needed to take all multi-pole type of interaction: dipole, quadrupole and quantum dynamics of the spins system …

- m^2 - is the charge(mass) of the tensor fields particles (like Higgs bosons);
- k - is the interaction between fields;
- J *- is the self interaction as in sigma or LGW models*

$$\alpha = \frac{1}{2}(M_{xy}^{(1)} + M_{xy}^{(2)}), \quad \beta = \frac{1}{2}(M_{xy}^{(1)} - M_{xy}^{(2)}). \tag{7}$$

Then different values of α and β correspond to different magnetic phases. The staggered magnetization can be defined as,

$$N^{\dagger}/\lambda^2 = -\int_1^{\infty} \frac{\beta}{r^2} dr. \tag{8}$$

The antiferromagnetic phase corresponds to the phase with nonzero staggered magnetization.

Put the expressions (7) into equations (4), we have the equations for α and β as

$$\begin{aligned} \alpha'' + \frac{f'\alpha'}{f} + \Big[\frac{J(3\beta^2+\alpha^2)}{r^6 f} - \frac{2f'}{rf} \\ -\frac{4f+m^2+k}{r^2 f}\Big]\alpha = \frac{B}{r^2 f}, \\ \beta'' + \frac{f'\beta'}{f} + \frac{J\beta^3}{r^6 f} + \Big(\frac{3J\alpha^2}{r^6 f} - \frac{2f'}{rf} - \frac{4}{r^2} \\ -\frac{m^2-k}{r^2 f}\Big)\beta = 0. \end{aligned} \tag{9}$$

The charged back hole encoding for finite density (2008 - ????)

Anti de Sitter universe.

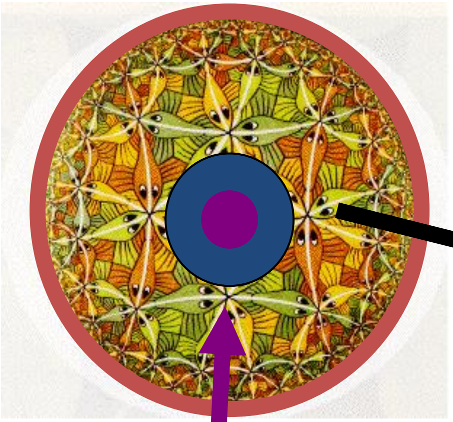

Charged black hole in the middle

J. Zaanen et al, 2008,…

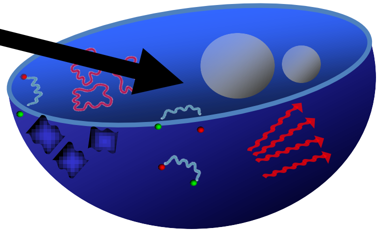

Finite density quantum matter:

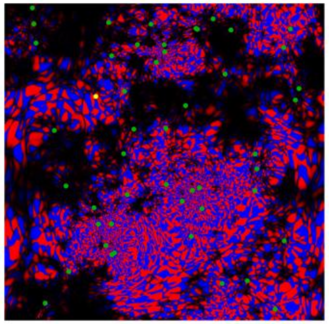

Holographic strange metals

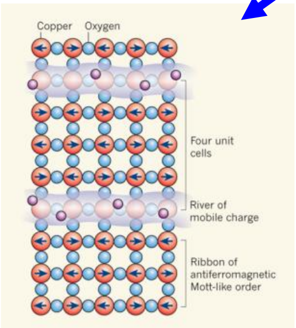

Stripy pseudogap orders

High Tc superconductors

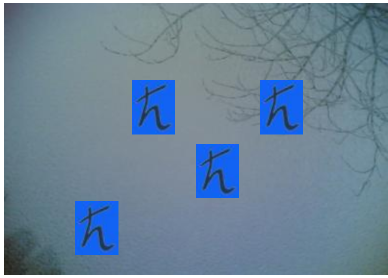

Emergent Fermi liquids

Quantum Critical Point in Magnetic Field

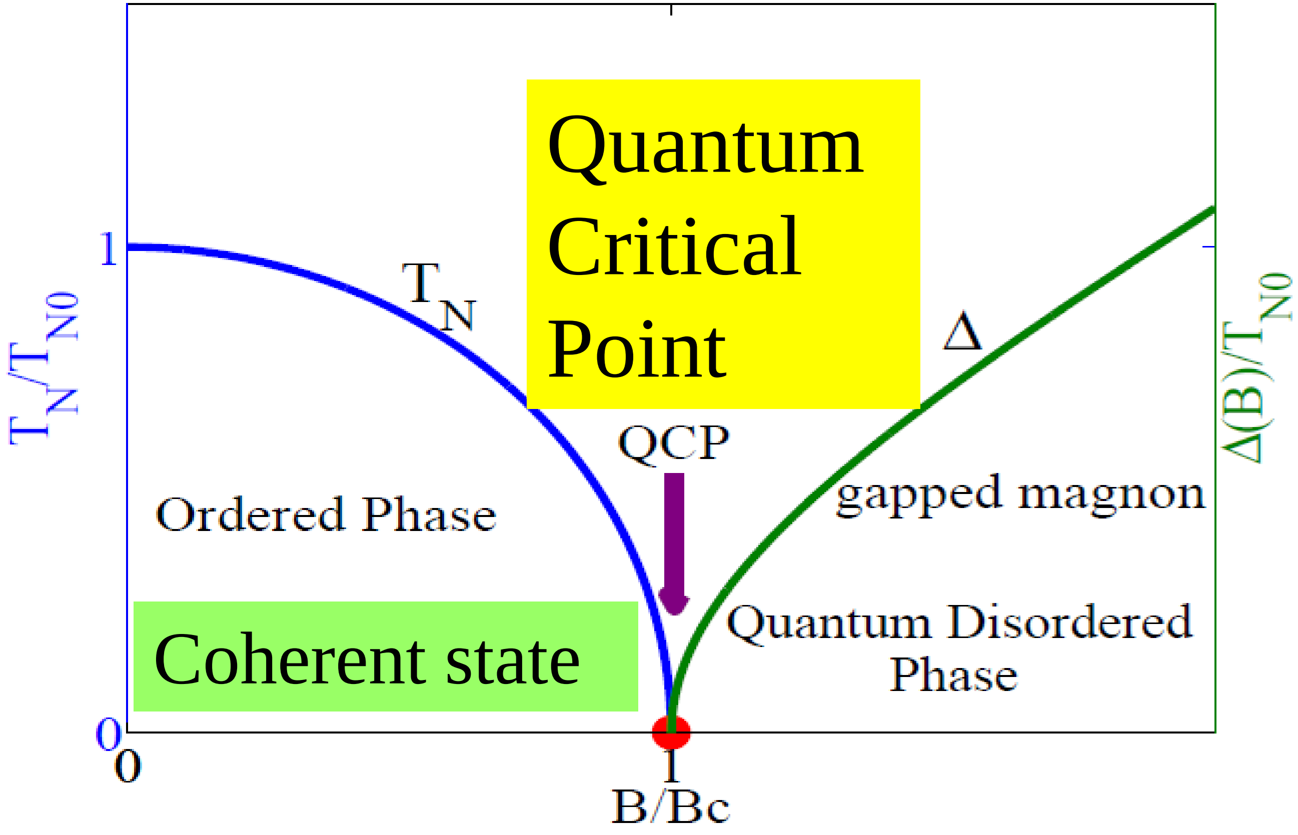

Existence of Coherence

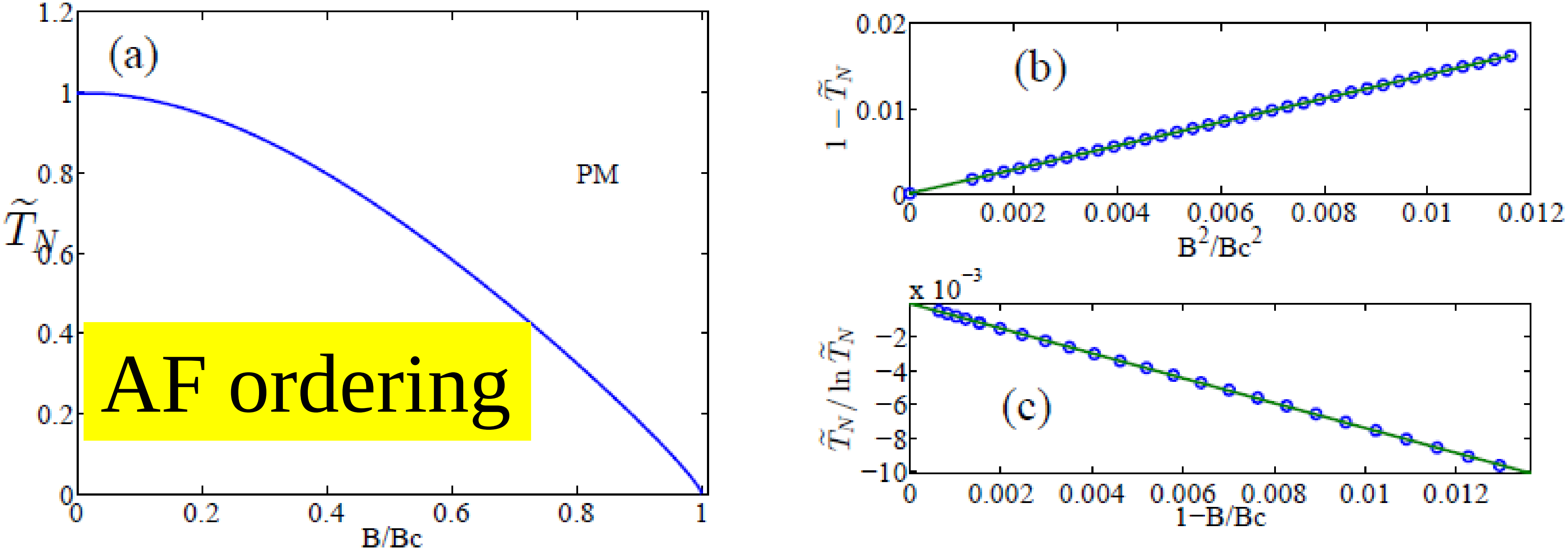

Figure 2: The relationship between antiferromagnetic critical temperature T_N and magnetic field B. (a) In the whole region of $0 \leq B \leq Bc$. (b) In the region of $B \ll B_c$. (c) In the region of $1 - B/B_c \to 0^+$.

Quantum Critical Point at B=B_c

$$\widetilde{T}_N / \ln \widetilde{T}_N \simeq -0.7393(1 - B/B_c).$$

Where $\widetilde{T}_N = T_N(B)/T_N(0)$

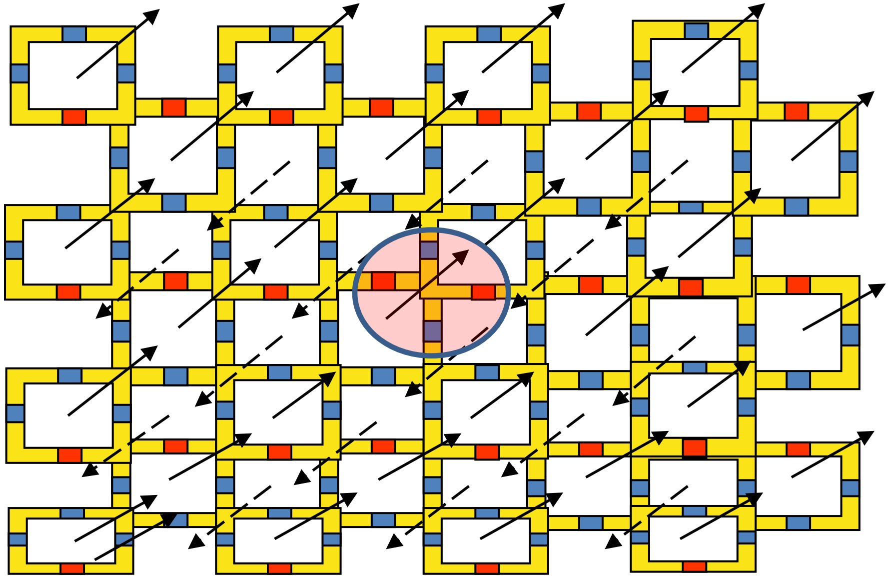

One may understand
it as rosy spin
in a mean field B_M
of all other spins

External field B_M
compensates
the applied one, B

When $B_M = B = B_c$
=>QCP

First Fit to Phase Diagram of $BiCoPO_5$

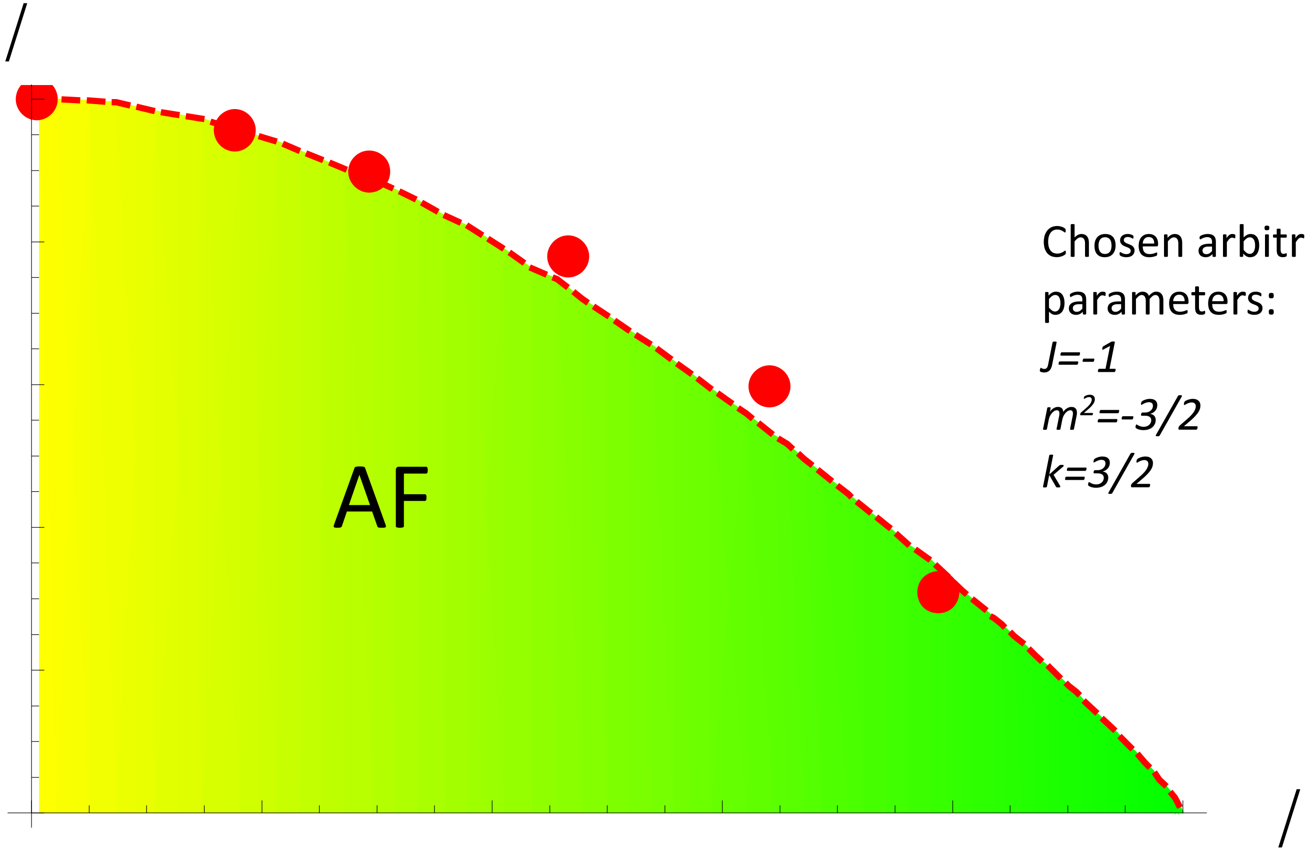

Chosen arbitrary parameters:
$J=-1$
$m^2=-3/2$
$k=3/2$

Phase Diagram of BiCoPO$_5$

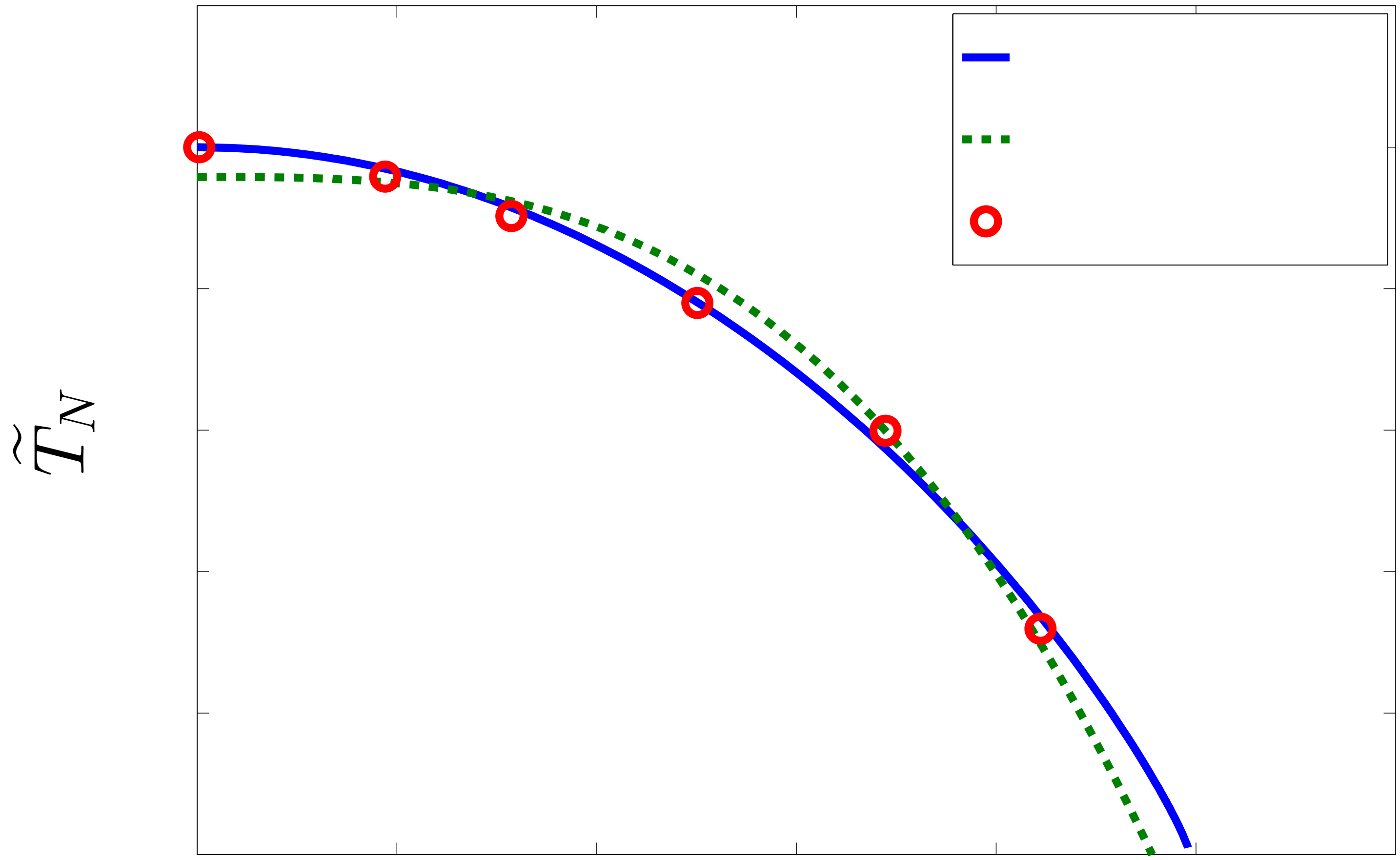

$J=-6$

$m^2=-3/2$

$k=3/2$

Comparison of Phase Diagram of BiCoPO$_5$ and other compounds

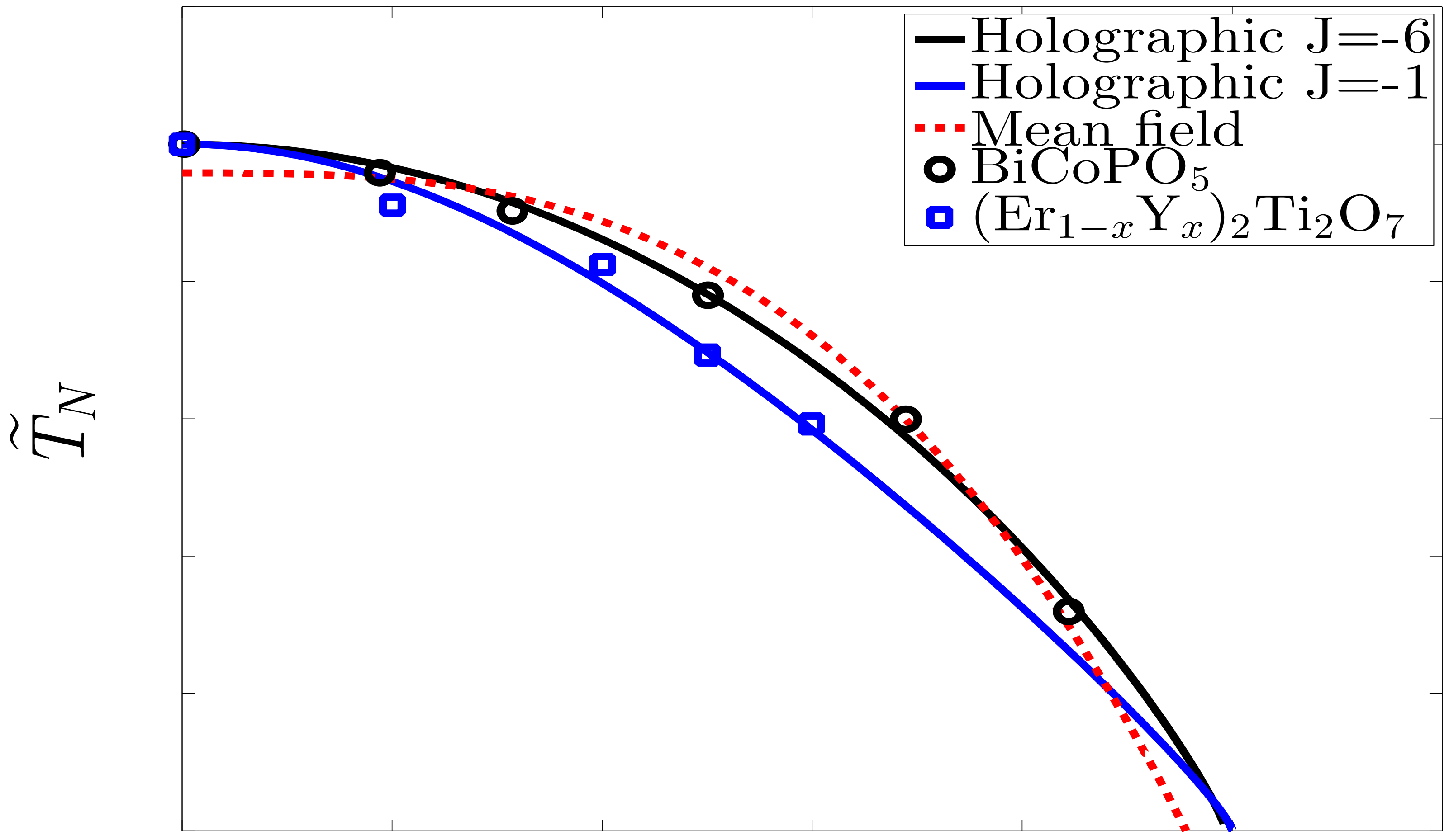

Quantum Critical Point for $BiCoPO_5$ and other compounds

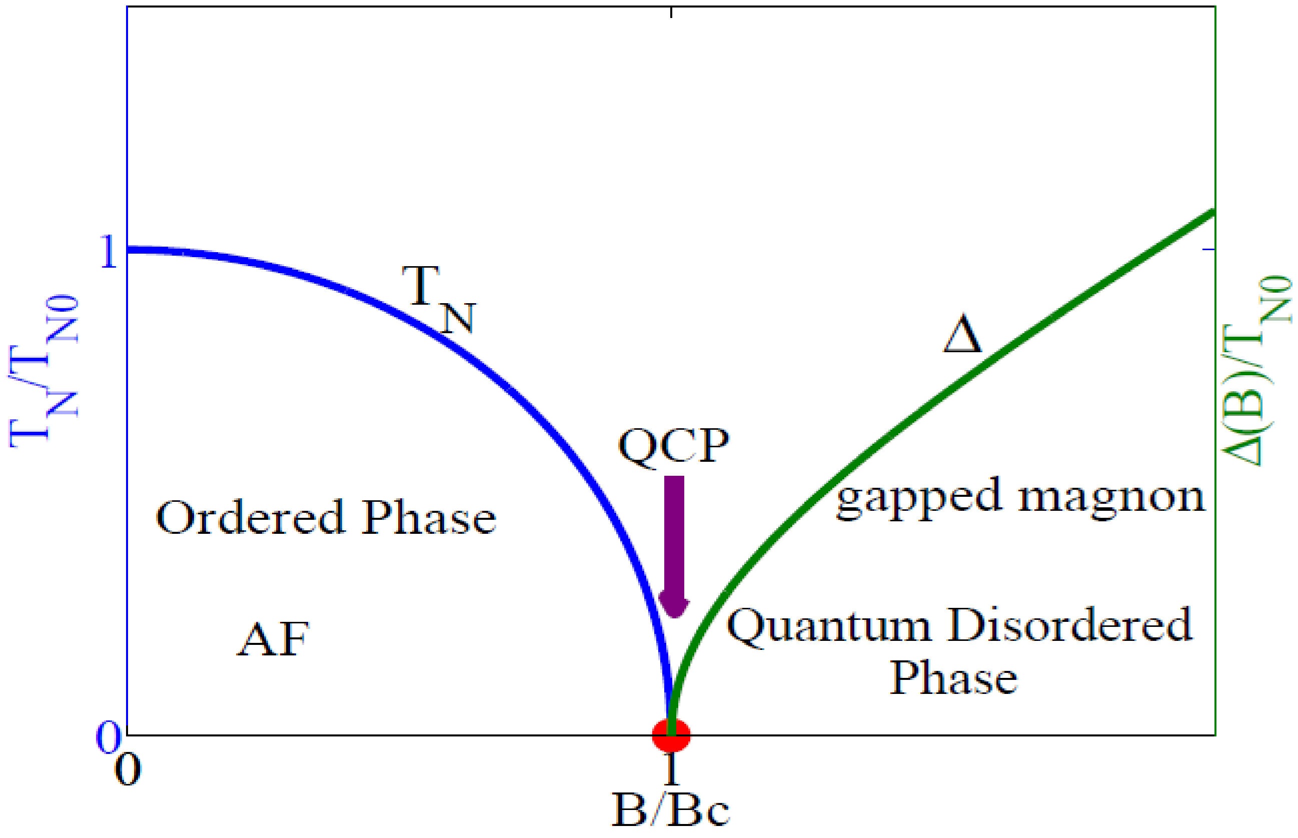

Spectral Function, when $B>B_c$

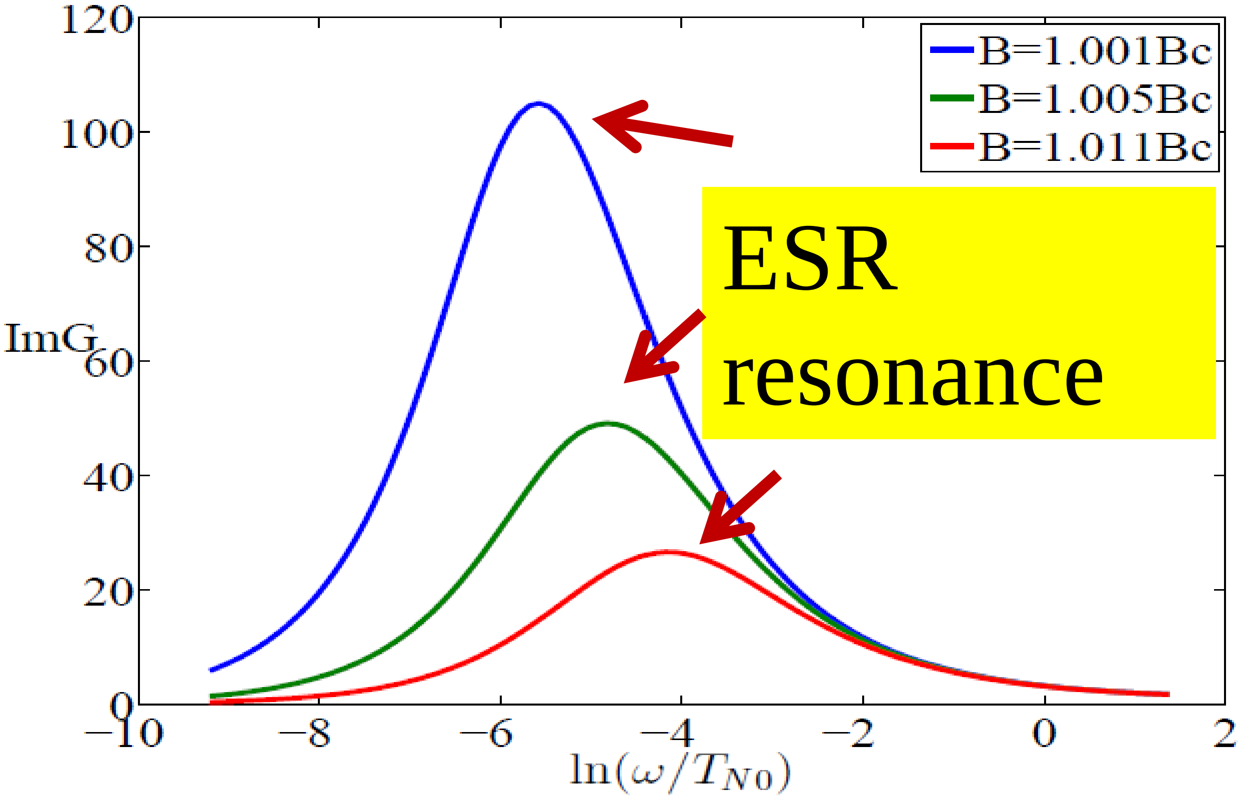

ESR resonance

we find the energy gap is fitted well by following

$$\widetilde{\Delta} \simeq 1.4803(B/B_c - 1), \text{with } \widetilde{\Delta} = \Delta/T_{N0}.$$

Summary, Part I

- Holographic duality AdS/CFT used to solve the quantum behavior of $BiCoPO_5$ at very low temperatures
- Finding of QPT from antiferromagnetic phase(AF) to quantum disordered or ferromagnetically order phase(QD)
- the Neel temperature, $T_{N,}$ of AF order is suppressed by magnetic field B at the critical magnetic field B_c, $T_N = 0$ there Quantum Phase Transition and QCP occur.
- At QCP, the dynamic exponent $z = 2$, which means that the boundary critical theory is indeed a strong coupling theory with effective dimension $d_e = d + z = 4$.
- The hyperscaling law is violated, logarithmic corrections and energy gap or ESR resonance excitation appear near the QCP,
- Correlation length describes by power law with exponents $\nu = 1/2$ and $z = 2$.

BiCoPO$_5$ in Magnetic Field

Reduced Temperature: $\varepsilon = (1-T/T_c)$

Critical Exponents:

$$\begin{array}{ll} M \approx \varepsilon^{\beta} & T < T_C \\ \chi \approx |\varepsilon|^{\gamma} & T \gtrless T_C \\ M \approx H^{1/\delta} & T = T_C \\ C \approx |\varepsilon|^{-\alpha} & T \gtrless T_C \\ \xi \approx |\varepsilon|^{-\nu} & T \gtrless T_C \\ G(r) \approx |r|^{-(D-2+\eta)} & T = T_C \end{array}$$

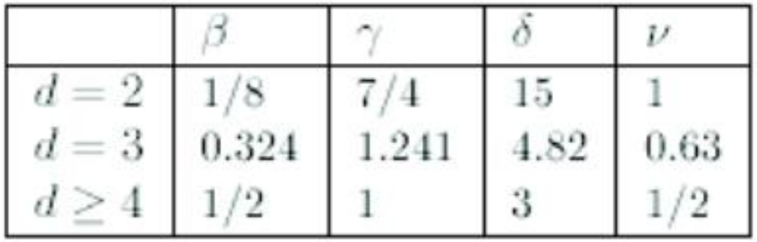

	β	γ	δ	ν
$d=2$	$1/8$	$7/4$	15	1
$d=3$	0.324	1.241	4.82	0.63
$d\geq 4$	$1/2$	1	3	$1/2$

Ising

Relations:

$$\begin{aligned} 2 &= \alpha + 2\beta + \gamma \\ \gamma &= \beta(\delta - 1) \\ \alpha &= 2 - \nu D \end{aligned}$$

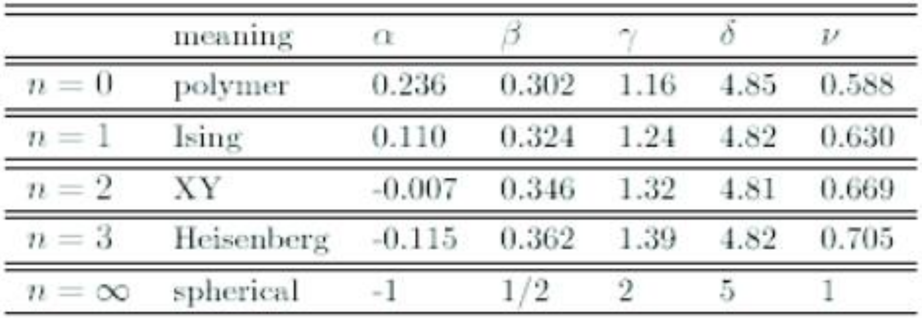

	meaning	α	β	γ	δ	ν
$n=0$	polymer	0.236	0.302	1.16	4.85	0.588
$n=1$	Ising	0.110	0.324	1.24	4.82	0.630
$n=2$	XY	-0.007	0.346	1.32	4.81	0.669
$n=3$	Heisenberg	-0.115	0.362	1.39	4.82	0.705
$n=\infty$	spherical	-1	1/2	2	5	1

3D n-vector model

Holographic AF state $$T_N \sim (-b)^{\psi}, \quad \Delta \sim b^{\nu z}, \quad l \sim b^{-\nu}.$$ ν=1/2

$$\psi = z/(d+z-2)$$ *z=d=2*

Summary, Part II

- Holographic duality AdS/CFT provides the complete characterisation of the AF state and QCP
- => other quasi one dimensional materials, no AF order
- Here Bc=0 , $T_N = 0$, and the QCP occur.
- At QCP, the dynamic exponent z = 2,
- The ESR resonance line ("energy gap") appear near the QCP,

we find the energy gap is fitted well by following

$$\widetilde{\Delta} \simeq 1.4803(B/B_c - 1), \text{with } \widetilde{\Delta} = \Delta/T_{N0}.$$

correlation length described by power law

- with exponents ν= 1/2 and z = 2.
- Similar quasi 1D compounds
- $(Sr,Ba)Co_2V_2O_8$

also $Er_{1-x}Y_xTi_2O_7$

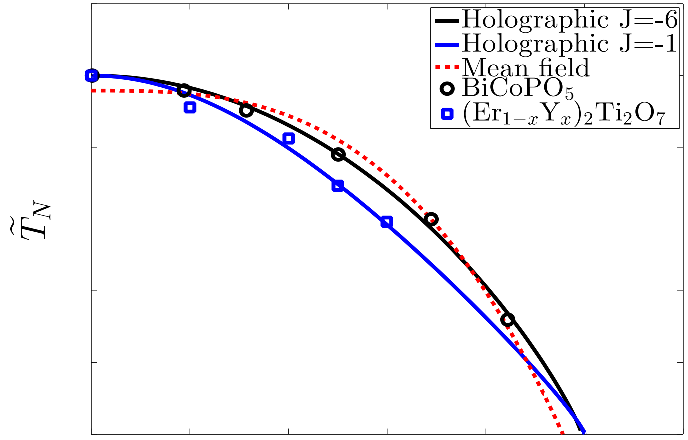

Holographic AF State in $BiCoPO_5$

Thank you for
your attention !

Magnetisation of $BiCoPO_5$

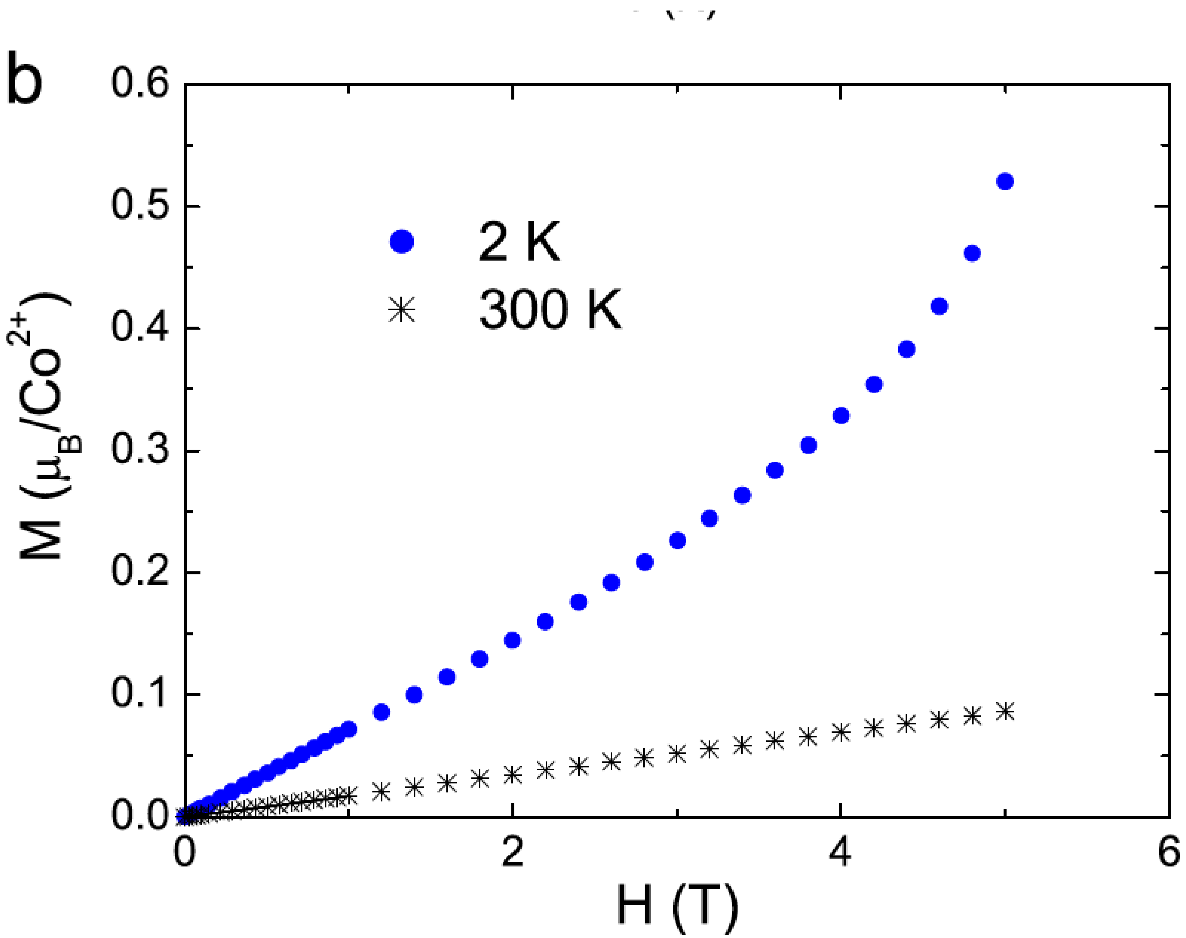

Weak vs Strong Interaction or Kramers-Wannier duality

Kramers Wannier, 1946

Low temperature or weakly coupled

$$H = \frac{J}{k_B T} \sum_{<ij>} S_i^z S_j^z$$

High temperature or strongly coupled

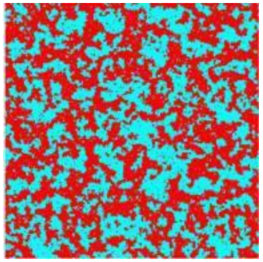

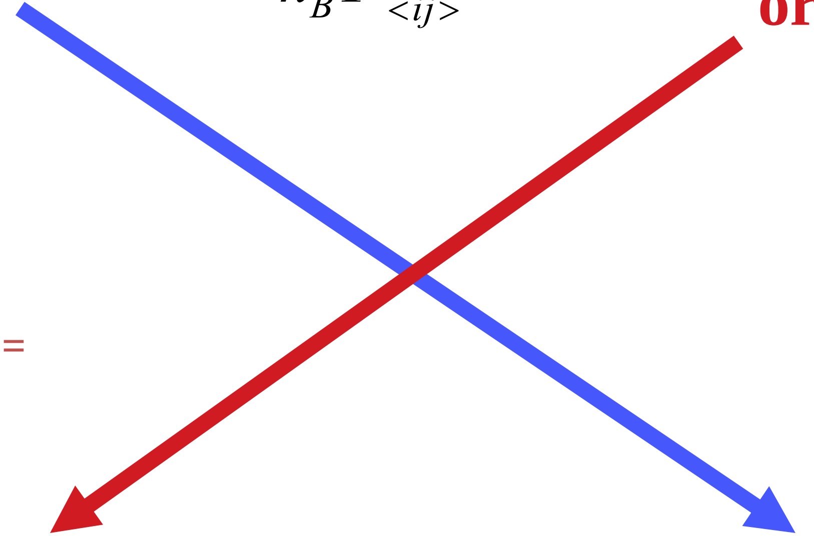

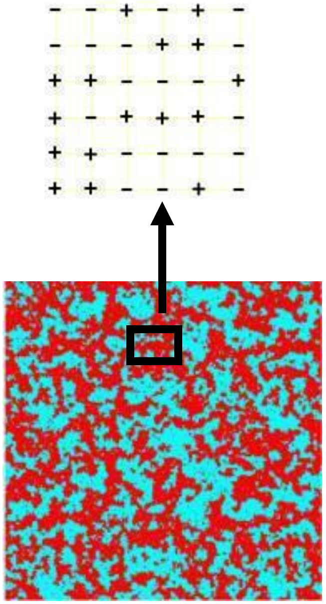

= domain wall condensate =

$$H = \frac{k_B T}{J} \sum_{<ij>} \tilde{S}_i^z \tilde{S}_j^z$$

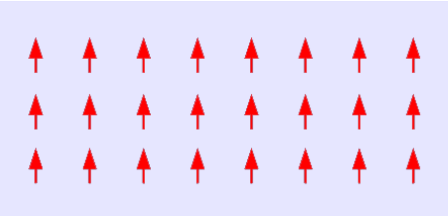

Self-duality special to 2D: e.g. in 3D global Ising dual to Ising gauge theory.

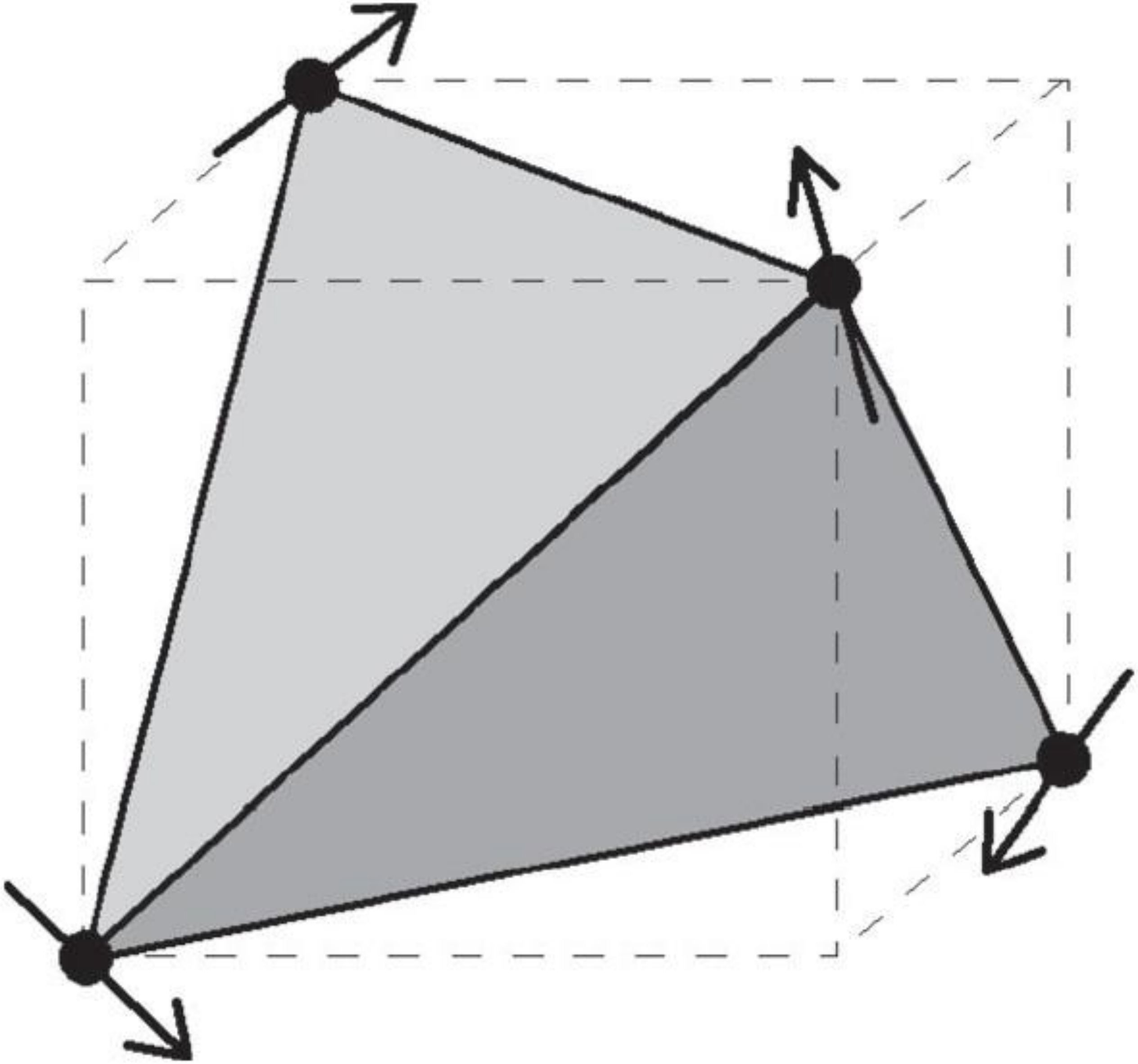

Figure 1. The ψ_2 ground state spin configuration for the *XY* antiferromagnet $Er_2Ti_2O_7$ [2].

Magnetisation of Er Ti O

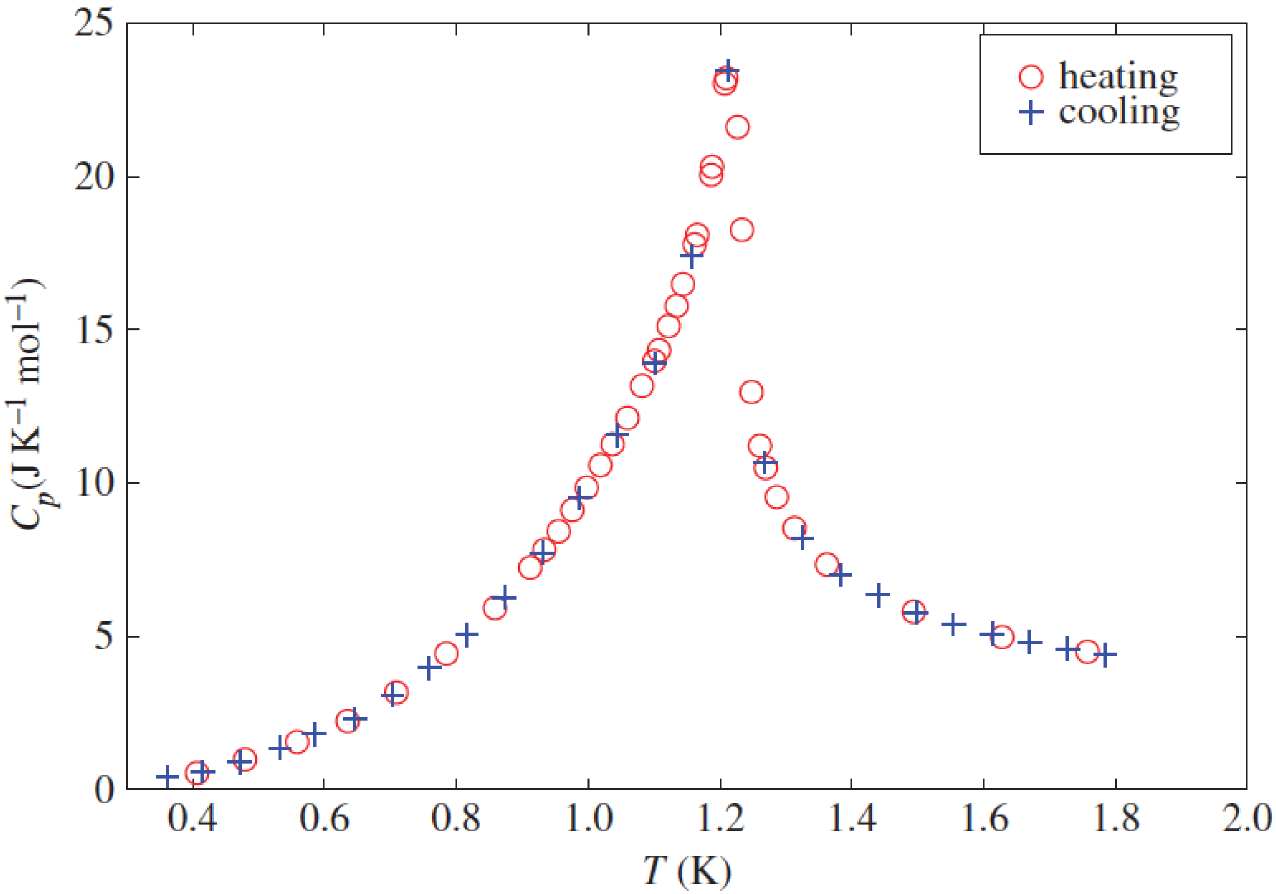

Figure 2. Experimental C_p values at zero field for $Er_2Ti_2O_7$ expressed per mole of $Er_2Ti_2O_7$, on heating and cooling, showing that the transition is second order. (Online version in colour.)

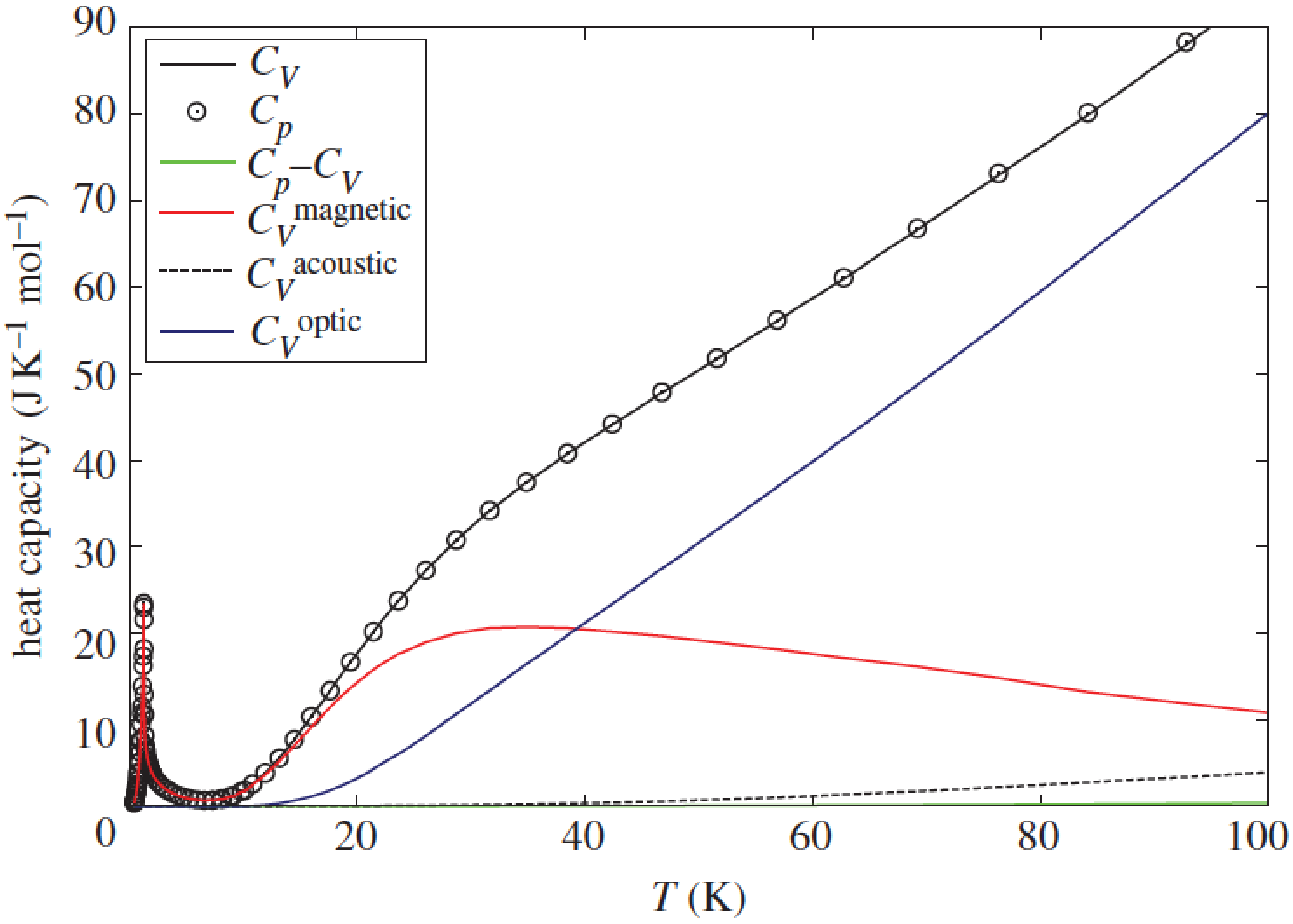

Figure 3. Experimental C_p values at zero field for $Er_2Ti_2O_7$ compared with the optic, magnetic and ($C_p - C_V$) contr where their sum is shown as C_V. Values are shown per mole of $Er_2Ti_2O_7$. (Online version in colour.)

Magnetisation of $Er_2Ti_2O_7$

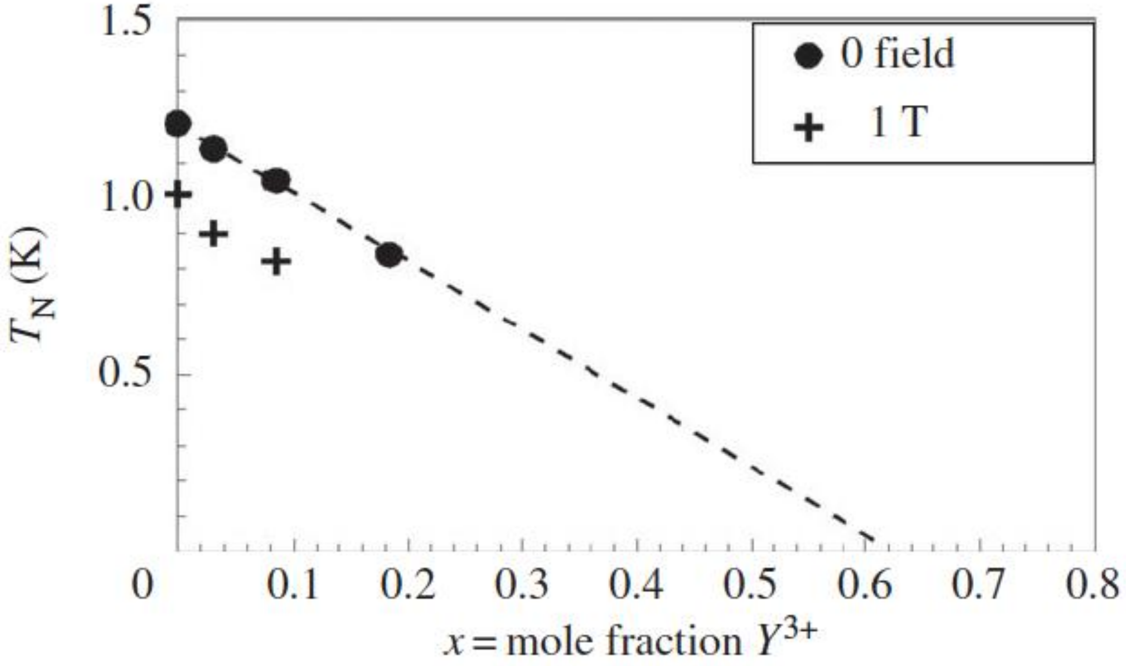

Figure 5. Néel temperature for $(Er_{1-x}Y_x)_2Ti_2O_7$ as a function of mole fraction of Y^{3+} ($= x$), in zero field and a 1 T field applied along the [110] direction.

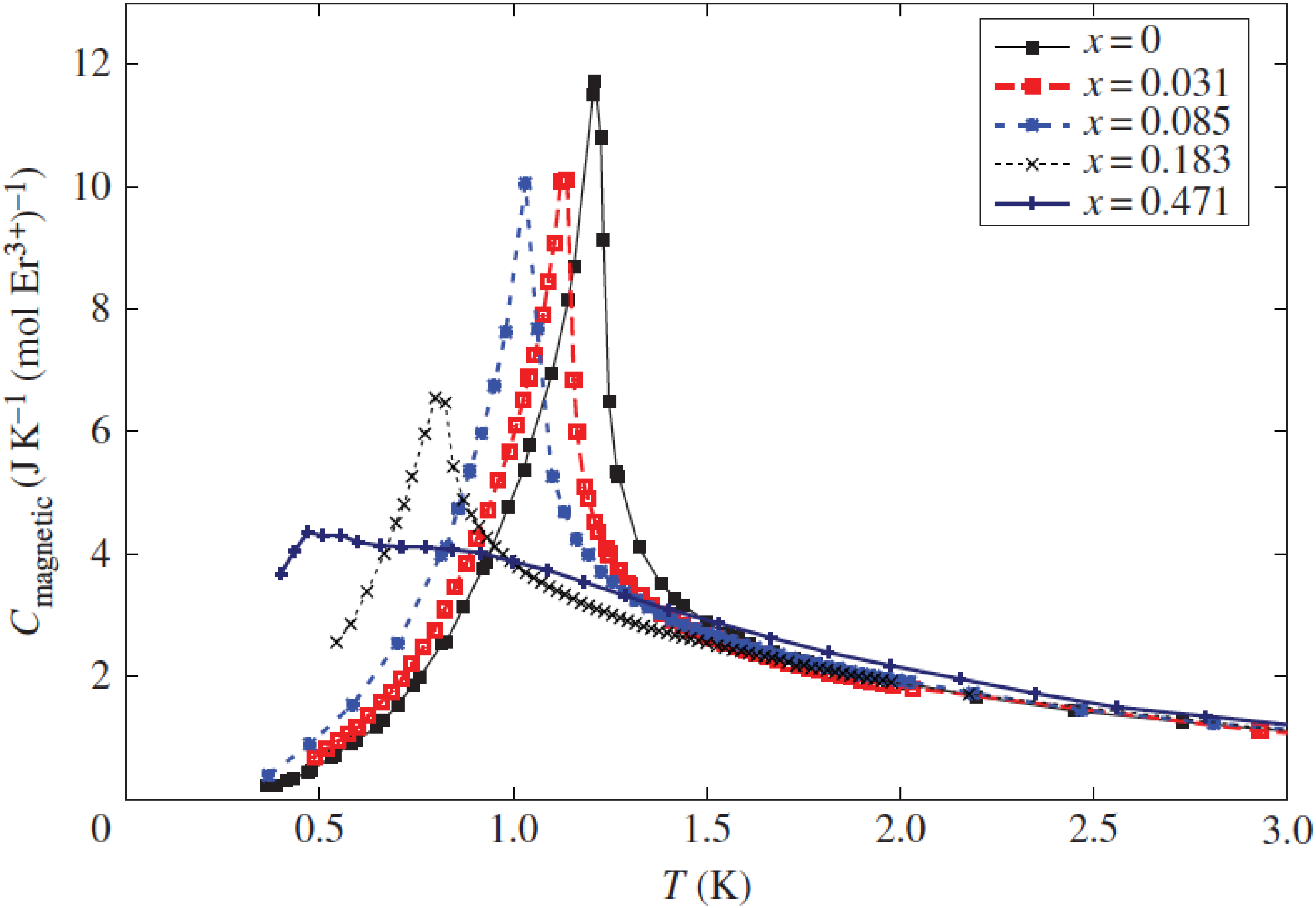

gure 6. Magnetic heat capacity of $(Er_{1-x}Y_x)_2Ti_2O_7$ in zero applied field. (Online version in colour.)

Magnetisation of Er Ti O

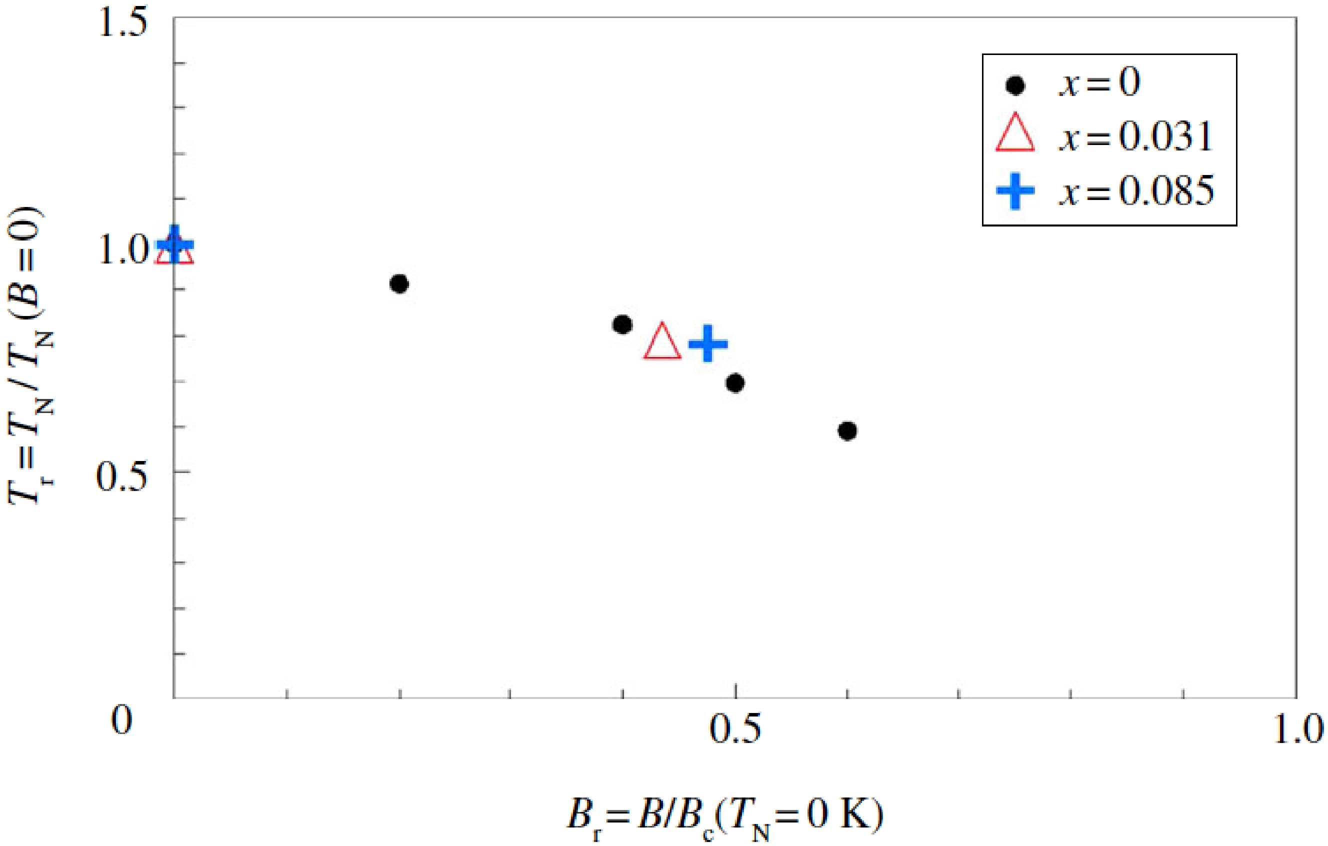

Figure 9. Reduced transition temperature as a function of reduced magnetic field for $(Er_{1-x}Y_x)_2Ti_2O_7$, showing that samples with different Y^{3+} doping levels exhibit the same relative behaviour as $Er_2Ti_2O_7$. (Online version in colour.)

Magnetic excitations in the *XY*-pyrochlore antiferromagnet $Er_2Ti_2O_7$

S. S. Sosin and L. A. Prozorova
P. L. Kapitza Institute for Physical Problems, RAS, 119334 Moscow, Russia

M. R. Lees, G. Balakrishnan, and O. A. Petrenko
Department of Physics, University of Warwick, Coventry CV4 7AL, United Kingdom

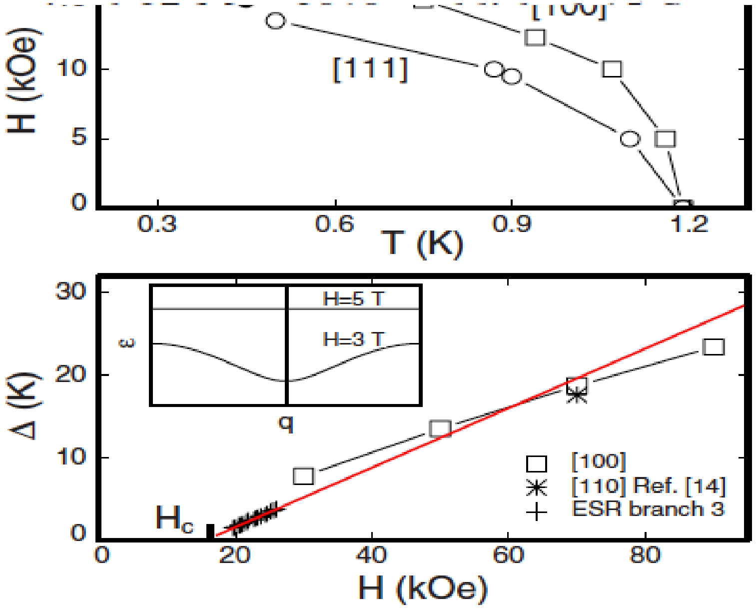

FIG. 6. (Color online) Upper panel: the phase diagram of $Er_2Ti_2O_7$ for $H \| [100]$ (□,■) and $H \| [111]$ (○, ●) obtained from specific heat and magnetic resonance data respectively. Lower panel: gap values determined from fitting the $C_p(T)$ curves for $H \| [100]$ by Eq. (1); $\nu(H)$ dependence of ESR branch 3 is shown by crosses, solid line is a linear extrapolation of this branch to high fields. The schematic transformation of the excitation spectrum at high fields (based on experimental data from Ref. 14) is given in the inset.

Magnetisation of $Er_2Ti_2O_7$

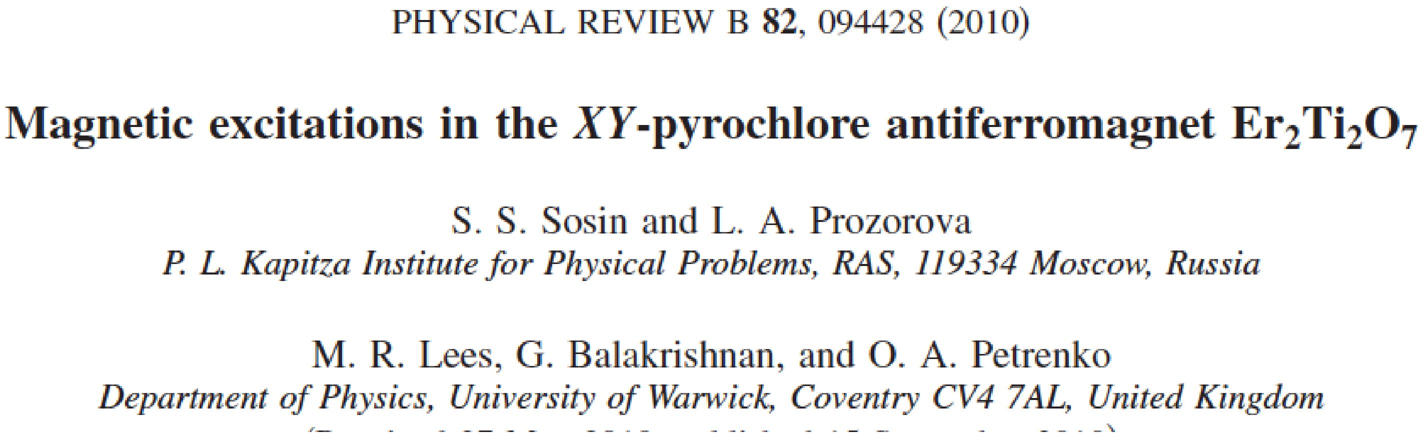

PHYSICAL REVIEW B **82**, 094428 (2010)

Magnetic excitations in the *XY*-pyrochlore antiferromagnet $Er_2Ti_2O_7$

S. S. Sosin and L. A. Prozorova
P. L. Kapitza Institute for Physical Problems, RAS, 119334 Moscow, Russia

M. R. Lees, G. Balakrishnan, and O. A. Petrenko
Department of Physics, University of Warwick, Coventry CV4 7AL, United Kingdom

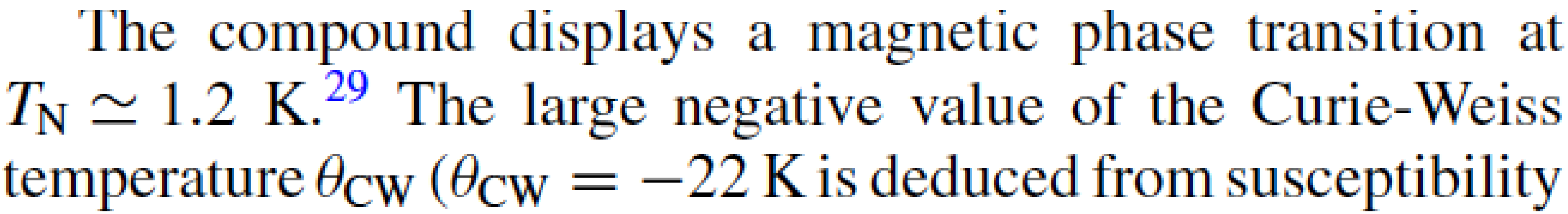

The compound displays a magnetic phase transition at $T_N \simeq 1.2$ K.[29] The large negative value of the Curie-Weiss temperature θ_{CW} ($\theta_{CW} = -22$ K is deduced from susceptibility

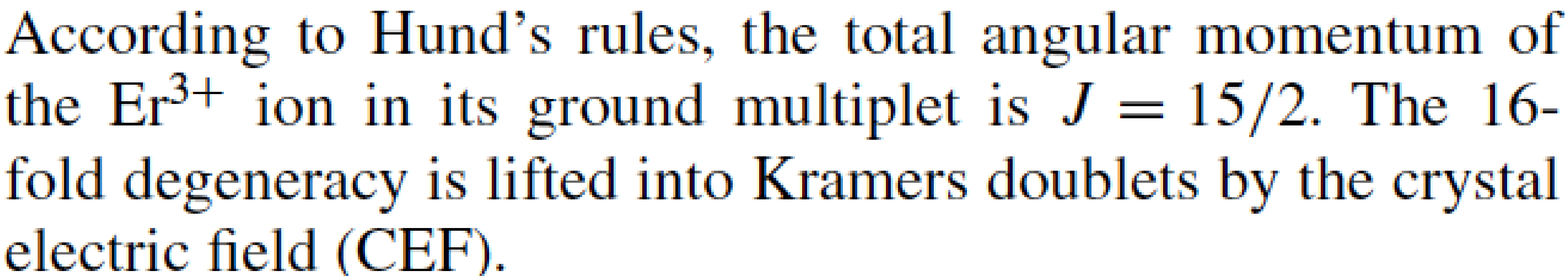

According to Hund's rules, the total angular momentum of the Er^{3+} ion in its ground multiplet is $J = 15/2$. The 16-fold degeneracy is lifted into Kramers doublets by the crystal electric field (CEF).

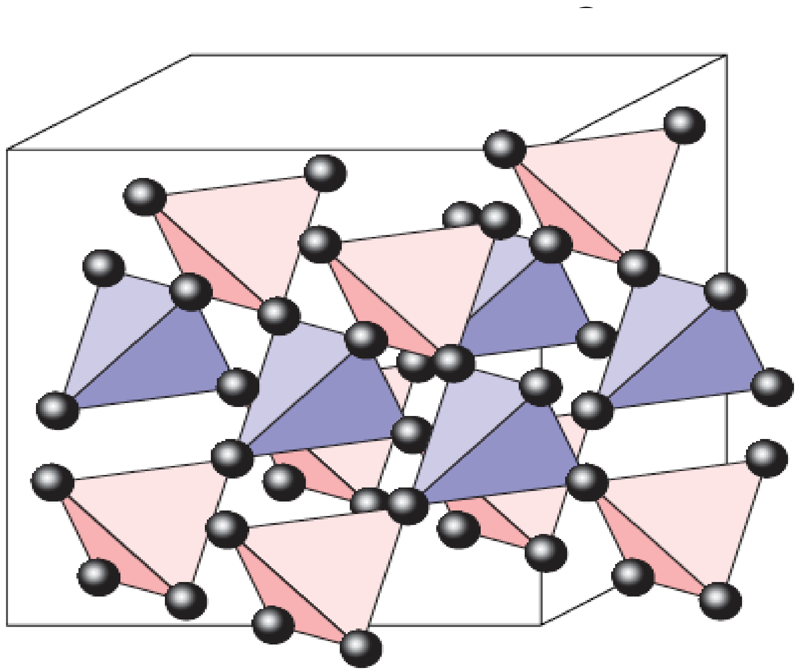

FIG. 1. (Color online) The network of corner-sharing regular tetrahedra formed by the rare-earth atoms in the pyrochlore structure in which $Er_2Ti_2O_7$ crystallizes. The axis of trigonal symmetry at the position of a rare earth is one of the cube diagonals. There are two types of tetrahedra in the network, which differ by their orientation: Type B is rotated by 90° about the cubic axes with respect to type A. We distinguish the two sets by two colors in the drawing. Since each rare earth is at a corner shared by two tetrahedra, one of each kind, either the set of the four corners of all the A tetrahedra or the set of the four corners of all the B tetrahedra is sufficient to describe the Er^{3+} lattice.

the static magnetic susceptibility χ is expected to follow a Curie-Weiss law far from the ordering temperature in the paramagnetic regime. It reads

$$\chi = \frac{C}{T - \theta_{\mathrm{CW}}}, \tag{4}$$

where the Curie constant C can be expressed in terms of the so-called paramagnetic moment m_{para}:

$$C = \frac{1}{v} \frac{\mu_0 \, m_{\mathrm{para}}^2}{3 k_{\mathrm{B}}}, \tag{5}$$

where $v = a^3 / N_{\mathrm{cell}}$ with N_{cell} being the number of Er^{3+} ions in the cubic cell ($N_{\mathrm{cell}} = 16$). For an isolated Er^{3+} ion, $m_{\mathrm{para}} = g_J \sqrt{J(J+1)} \, \mu_{\mathrm{B}} = 9.58 \mu_{\mathrm{B}}$.

In Fig. 5 we display our result for the inverse of the static susceptibility versus temperature in a large temperature range. The Curie-Weiss law provides a good description of our data above 30 K. The fit gives for the Curie-Weiss temperature $\theta_{\mathrm{CW}} = -17.5\,(3)$ K and $C = 3.73\,(4)$ K. This means that $m_{\mathrm{para}} = 9.55\,(10) \mu_{\mathrm{B}}$, in agreement with the result exchange integral $\mathcal{I}$ ($\mathcal{I} > 0$), i.e.,

$$\mathcal{H} = \frac{\mathcal{I}}{2} \sum_{i,j,i \neq j} \mathbf{J}_i \cdot \mathbf{J}_j = \mathcal{I} \sum_{\langle i,j \rangle} \mathbf{J}_i \cdot \mathbf{J}_j, \tag{6}$$

the molecular-field approximation predicts

$$\mathcal{I} = \frac{3\, k_{\mathrm{B}} |\theta_{\mathrm{CW}}|}{z_{\mathrm{nn}} J(J+1)}. \tag{7}$$

We denote as z_{nn} the number of nearest neighbor Er^{3+} ions to a given Er^{3+} ion. In our case $z_{\mathrm{nn}} = 6$. From the measured θ_{CW} value and taking into account that $J = 15/2$, we compute $\mathcal{I}/k_{\mathrm{B}} = 0.138\,(2)$ K.

We have also measured the susceptibility for $2.0 < T < 6.0$ K under a field of 1 mT applied along a [111] axis using two protocols; see Fig. 6. Contrary to a previous report,[30] we do not observe any history-dependent effect at $T \leqslant 3.2$ K. Hence, there is no spin-glass-like irreversible effect for our $\mathrm{Er}_2\mathrm{Ti}_2\mathrm{O}_7$ crystals.

The other contribution to the low-temperature specific heat arises from magnons. Low-energy magnons have indeed been observed in neutron scattering experiments.[20] The dispersion relation $\hbar\omega(\mathbf{q})$ for their lowest energy branch is needed to compute C_{sw}. An approximate expression valid at small wave vectors is

$$\hbar^2\omega^2(\mathbf{q}) = \hbar^2\omega^2(q) = \Delta_{\mathrm{sw}}^2 + \hbar^2 v_{\mathrm{sw}}^2 q^2. \tag{10}$$

Here Δ_{sw} is the gap energy of the magnon spectrum at the zone center and v_{sw} is the magnon velocity. We note that a dispersion relation has recently been proposed for $\mathrm{Er_2Ti_2O_7}$ in the framework of linear spin-wave theory.[26] The applicability of this theory in frustrated systems might be questionable as recently discussed in the case of the triangular lattice.[42] Still, the model of Ref. 26 leads to an anisotropic dispersion relation. The resulting specific heat depends on a single magnon velocity which is the geometrical mean of the three magnon velocities along orthogonal axes. In our model it corresponds to v_{sw}.

quadrupole interaction is not negligible compared to the Zeeman interaction. This is due to the fact that the quadrupole moment Q_{167} of ^{167}Er is larger than that of ^{159}Tb (3.565 vs 1.432 barns) and the gyromagnetic ratio γ_{167} of ^{167}Er is much smaller, in absolute value, than that of ^{159}Tb (-7.7157 vs 64.31 Mrad $\mathrm{s}^{-1}\,\mathrm{T}^{-1}$); see Ref. 41. The Zeeman and quadrupolar Hamiltonians are written

$$\mathcal{H}_{\mathrm{Zee}} = -\hbar\gamma_{167}\mathbf{I}\cdot\mathbf{B}_{\mathrm{hyp}} \tag{8}$$

and

$$\mathcal{H}_{\mathrm{Q}} = \hbar\omega_{\mathrm{Q}}\left[3I_z^2 - I(I+1)\right], \tag{9}$$

respectively. In these equations, $\mathbf{I}$ is the ^{167}Er spin operator ($I = 7/2$) and $\hbar\omega_{\mathrm{Q}} = \frac{eQ_{167}V_{zz}}{4I(2I-1)}$, where V_{zz} is the principal component of the electric field gradient tensor acting on the rare-earth nucleus with z being as before the local threefold axis. The symmetry at the rare-earth site imposes the electric-field gradient to be axial. Because the Er^{3+} ordered magnetic moments are (nearly) perpendicular to z we shall also take

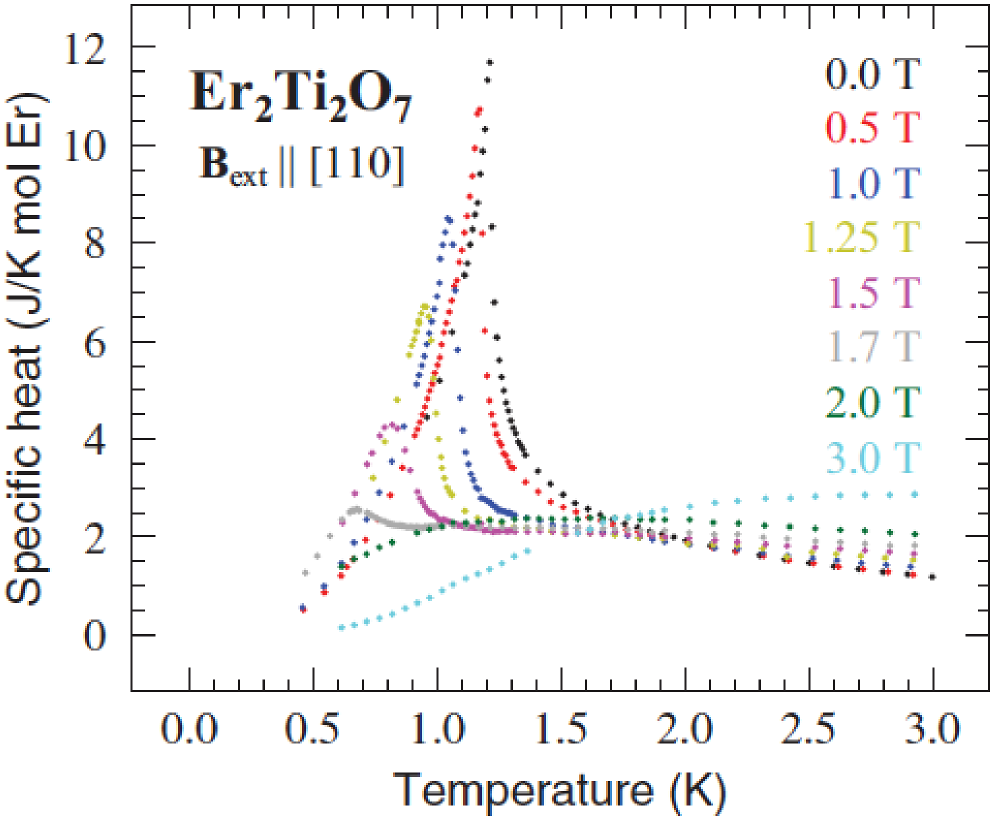

FIG. 11. (Color online) Temperature dependence of the specific heat of a Er$_2$Ti$_2$O$_7$ single crystal for different magnetic field intensities applied along [110]. The maximum of the specific-heat peak moves to lower temperatures as the field increases up to 1.7 T. No peak is observed when the field strength is above 1.7 T.

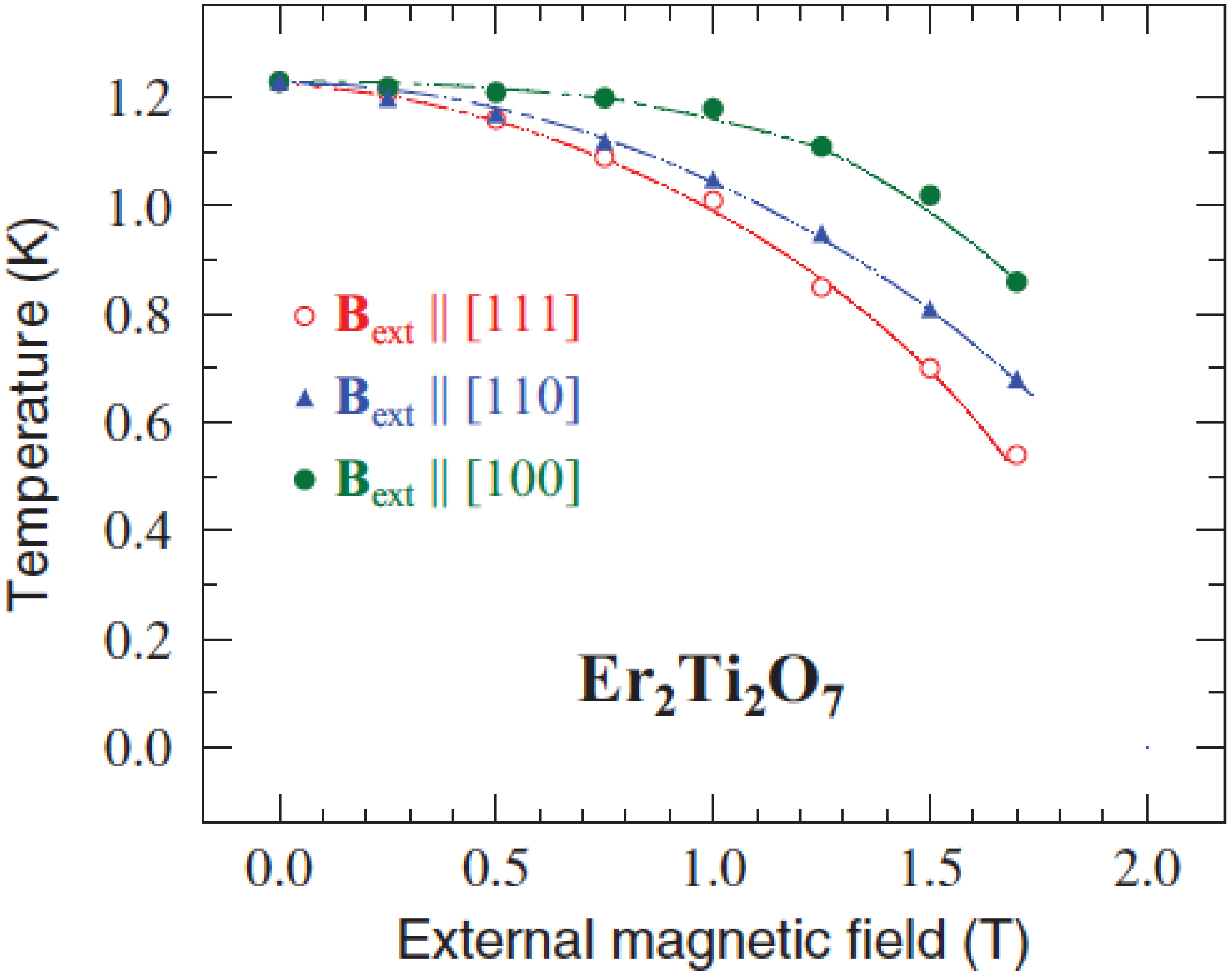

FIG. 12. (Color online) The phase diagram derived from specific-heat measurements for the three main crystal directions of cubic $Er_2Ti_2O_7$. The dashed-dotted lines are guides to the eye.

1. Magnetic correlation length

Here we determine the correlation length of the critical magnetic correlations. For this purpose we consider the scattered intensity measured in the vicinity of the reciprocal positions $\mathbf{q}_{(h,k,l)} = \mathbf{q}_{(2,2,0)}$ and $\mathbf{q}_{(1,1,1)}$ at $T = 2.00$ and 1.47 K, respectively; see Fig. 15. This critical scattering intensity is described by the sum of a Lorentzian function and a constant:

$$\mathcal{L}(|\mathbf{q} - \mathbf{q}_{(h,k,l)}|) = \frac{I_{\mathrm{L}}}{1 + |\mathbf{q} - \mathbf{q}_{(h,k,l)}|^2/\kappa_{\mathrm{m}}^2} + I_0, \qquad (15)$$

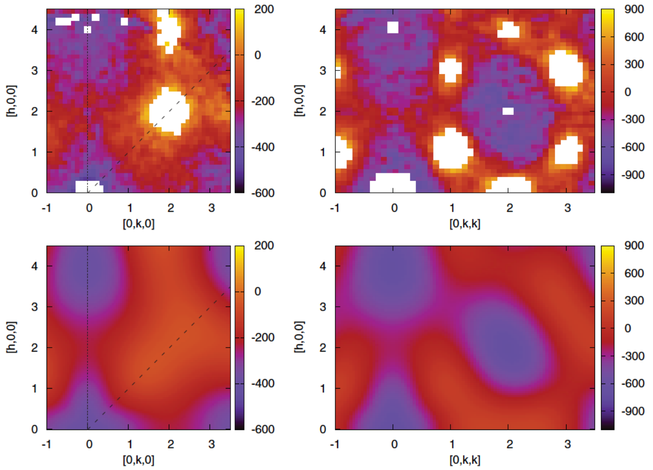

(Color online) Top two panels: Magnetic diffuse neutron scattering intensity recorded for a crystal of $Er_2Ti_2O_7$

FIG. 14. (Color online) Top two panels: Magnetic diffuse neutron scattering intensity recorded for a crystal of $Er_2Ti_2O_7$ in the reciprocal $(h,k,0)$ and (h,k,k) planes at 2.00 (3) and 1.47 (3) K, respectively. The positions in the reciprocal lattice are in $2\pi/a$ units, where a is the lattice parameter of the cubic unit cell. These maps are obtained as explained in the main text. To preserve the maps appearance, pixels with off-scale intensities, e.g., pixels influenced by Bragg reflections and critical scattering, as well as pixels located near the origin of the reciprocal lattice have been graphically eliminated: They are represented in white color. Bottom two panels: $(h,k,0)$ and (h,k,k) magnetic correlation maps computed with the tetrahedron model explained in the main text. The comparison between the theoretical and experimental maps displayed above enables us to derive information on the $Er_2Ti_2O_7$ interaction constants. The lines drawn in the $(h,k,0)$ maps indicate the position of the cuts shown in Fig. 16.

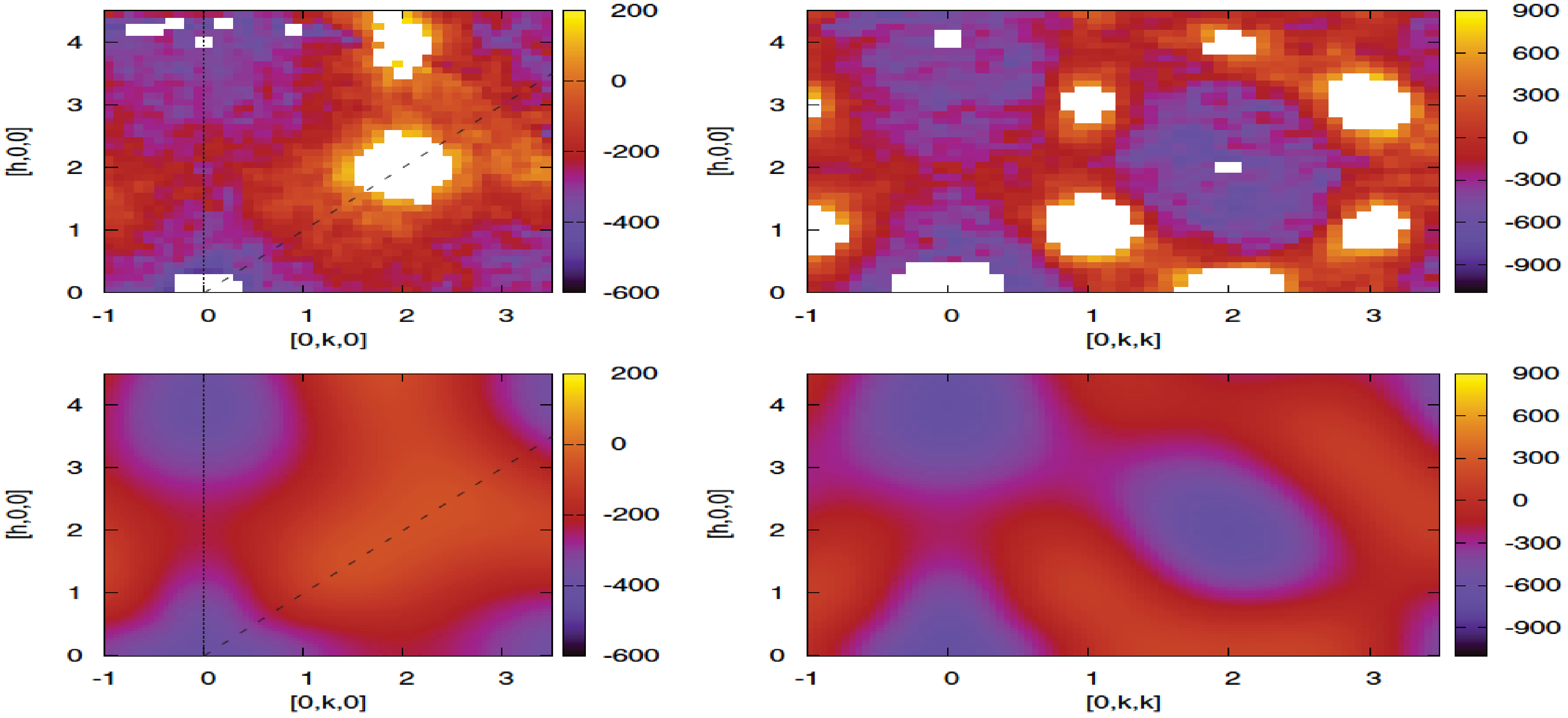

lor online) Top two panels: Magnetic diffuse neutron scattering intensity recorded for a crystal of $Er_2Ti_2O_7$

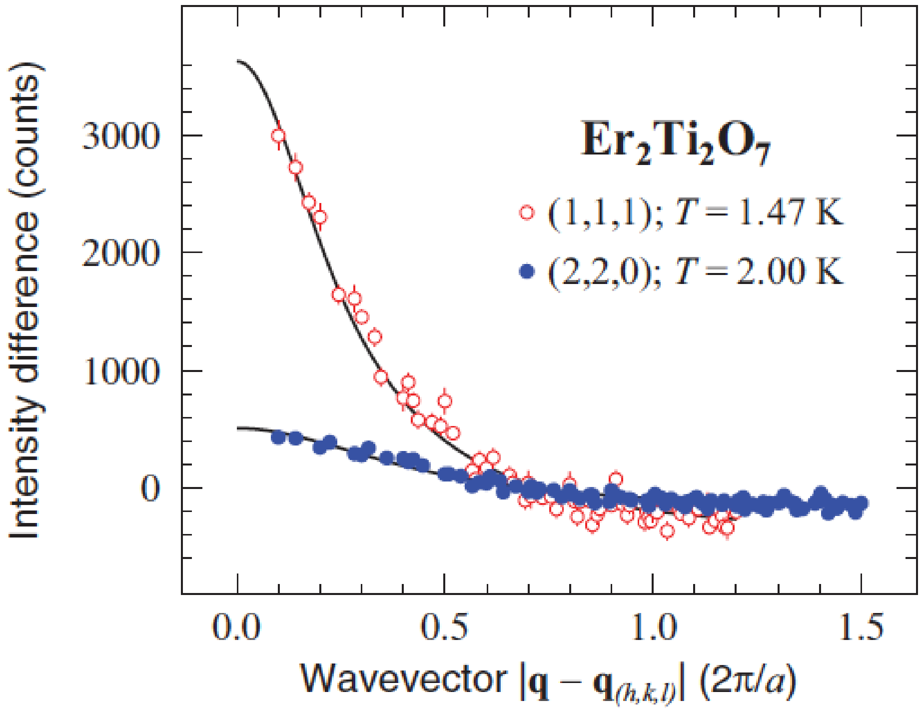

Fig. 15 yield the magnetic correlation lengths $\xi_{\rm m} = \kappa_{\rm m}^{-1} =$ 3.6 (2) and 6.6 (5) Å for the (2,2,0) and (1,1,1) reflections measured at 2.00 and 1.47 K, respectively. As expected, $\xi_{\rm m}$ shoots up as the sample is cooled toward the transition. These two values are comparable with the Er^{3+}-Er^{3+} ion distance $d =$ 3.56 Å. Hence the analysis of the experimental maps shown

from fits of Eq. (15) to the data.

Magnetisation of $SrCo_2V_2O_8$

$SrCo_2V_2O_8$ has the tetragonal crystal structure of space group *I*41*cd* with lattice constants $a=12.267(1)$ Å, $c=8.424(1)$ Å, and Z=8.[11] As shown in Fig. 1, similar to $BaCo_2V_2O_8$, the most prominent structural feature is that all magnetic Co^{2+} ions are equivalent in the arrays of edge-shared CoO_6 octahedra forming a screw-chain along the *c*-axis and the screw chains are separated by non-magnetic VO_4 (V^{5+}) tetrahedra and Sr^{2+} ions, resulting in quasi-one-dimensional arrangement.

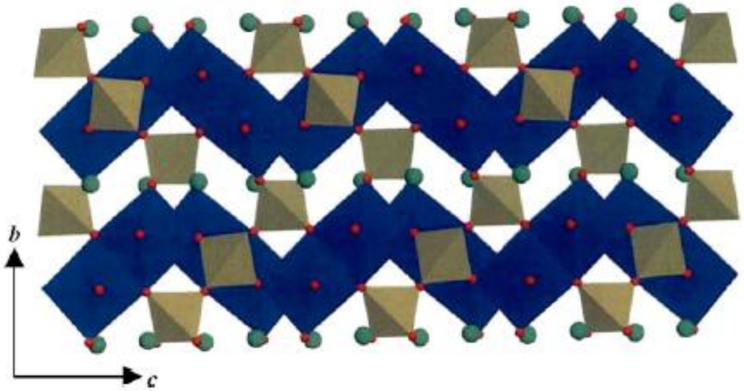

FIG. 1. (Color online) Crystal structure of $SrCo_2V_2O_8$. Octaheadra, tetraheadra, large ball and small ball represent CoO_6, VO_4, Sr, and O, respectively.

Magnetisation of Sr

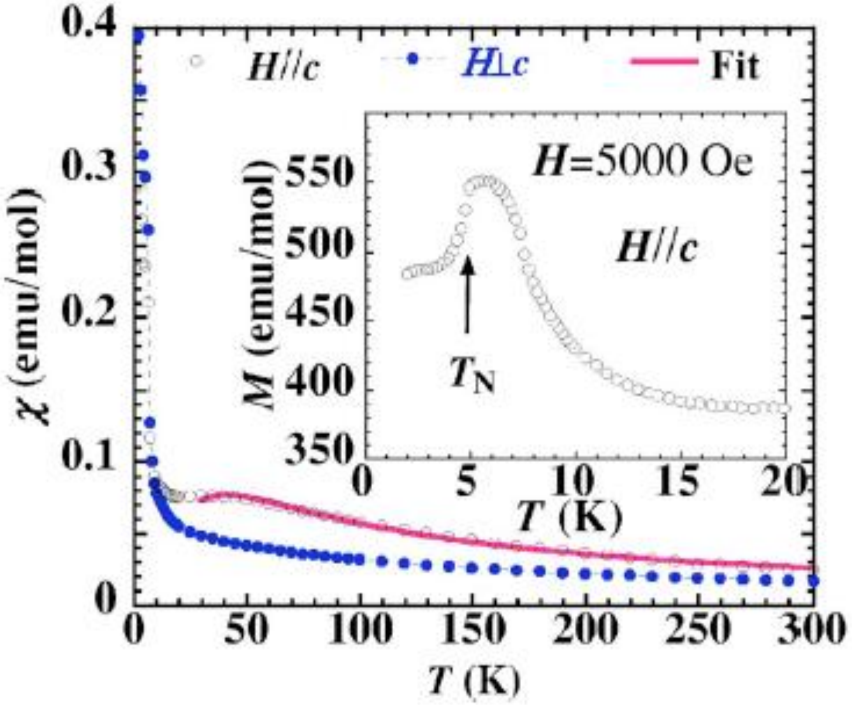

FIG. 2. (Color online) (a) Magnetic susceptibilities in H =1000 Oe parallel ($\chi_{\parallel}$) and perpendicular ($\chi_{\perp}$) to the c-axis. The solid line is a fit using a 1D Ising spin chain model for Co^{2+} magnetic systems (Ref. 14). The inset of Fig. 2 shows an antiferromagnetic ordering at ~5 K and the ferromagnetic ordered moment in an applied field of 5000 Oe.

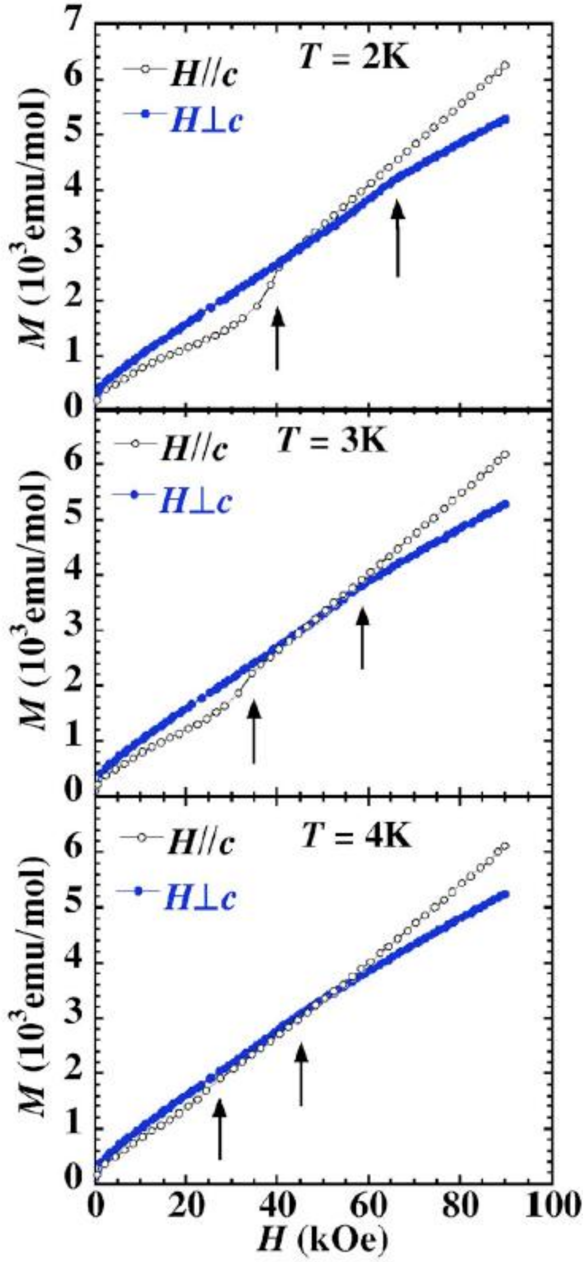

FIG. 3. (Color online) Magnetization versus applied field

Magnetisation of $SrCo_2V_2O_8$

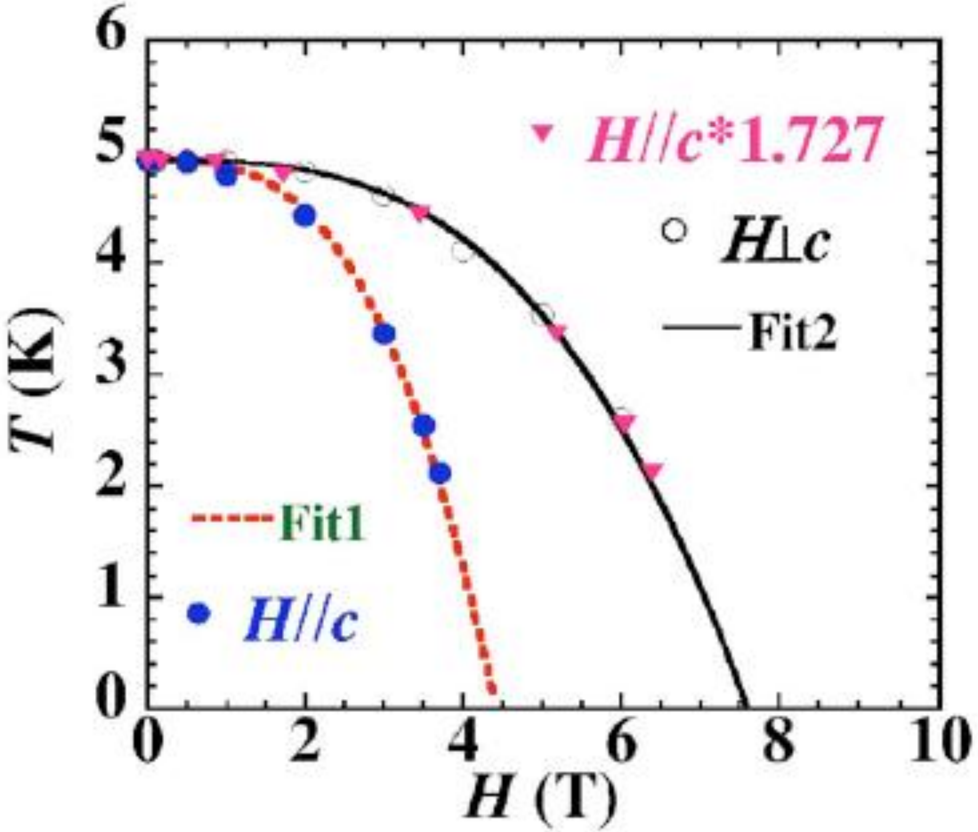

FIG. 6. (Color online) Phase diagram of $SrCo_2V_2O_8$ in the field (H)-temperature (T) plane. Solid lines and dashed lines are fits with $H=H_c(1-T/T_N)^{1/3}$. The triangles denote the data points for fields parallel to the c-axis where the critical fields are multiplied by a

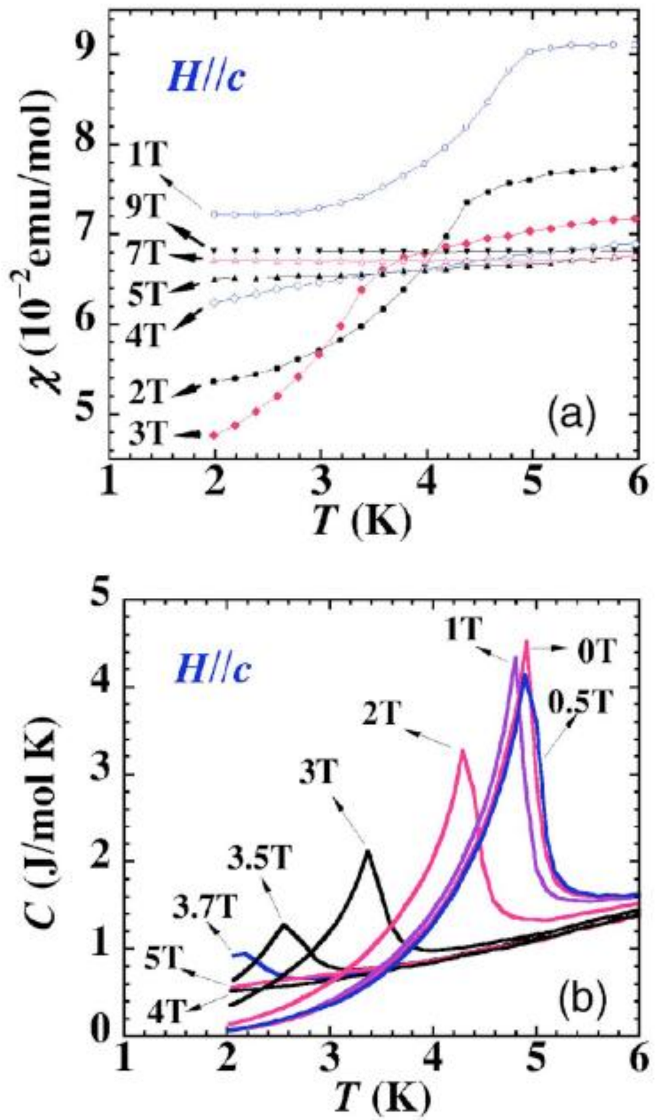

FIG. 4. (Color online) (a) Low temperature susceptibility and (b) heat capacity data measured in various fields parallel to the c-axis.

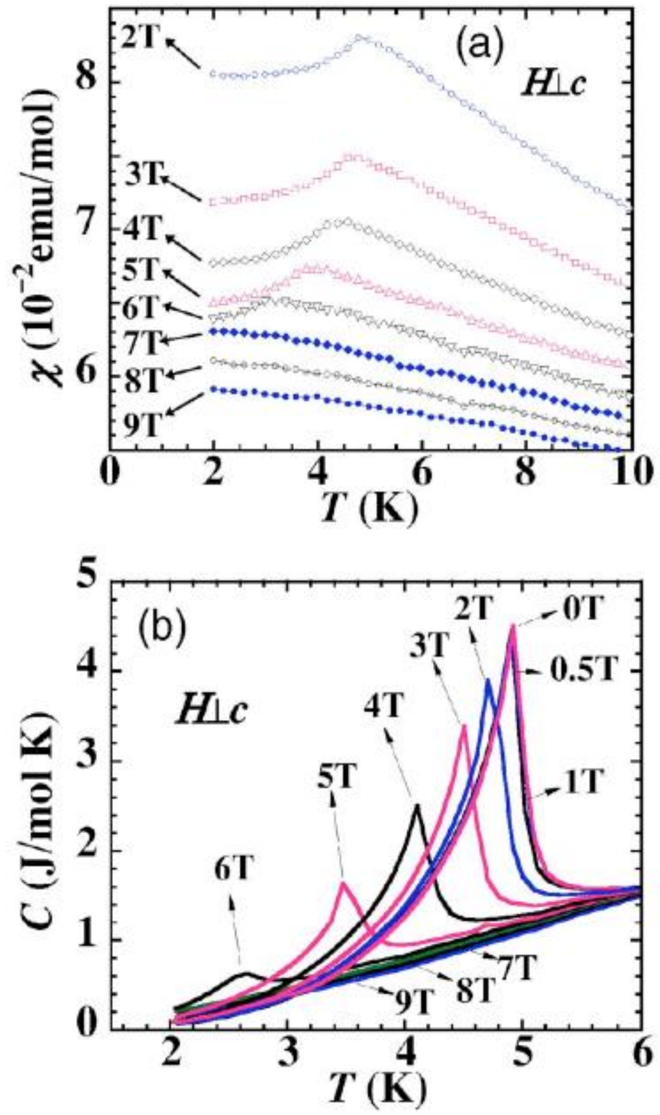

FIG. 5. (Color online) (a) Low temperature susceptibility and (b) heat capacity data measured in various fields perpendicular to the c-axis.

Summary for $SrCo_2V_2O_8$

- There is the field-induced magnetic transitions in the quasi-1D spin chain system $SrCo_2$ V_2 O_8 under longitudinal and transverse fields
- by means of magnetic susceptibility and heat capacity measurements.

- antiferromagnetic-paramagnetic transition is observed instead of spin-flop transition in the longitudinal field to magnetic easy **c** -axis, which is similar to that in the transverse field.

The antiferromagnetic-paramagnetic (AF-PM) transitions occur

- in the same framework for both longitudinal and transverse fields.
- These interesting magnetic transitions in $SrCo_2$ V_2 O_8 , irrespective of the applied field direction, are likely due to its large anisotropy

- The observation of field-induced magnetic transition in $SrCo_2$ V_2 O_8 will stimulate further theoretical and experimental studies of quasi-1D anisotropic spin chain systems

Magnetisation of $SrCo_2V_2O_8$

Magnetisation of $SrCo_2V_2O_8$

Magnetisation of $SrCo_2V_2O_8$

The low-energy dynamics of the large-spin one-dimensional Heisenberg Antiferromagnet is found to be the O(3) nonlinear sigma model. (Haldane , 1983)

Basics of holographic description

- Boundary values of bulk fields act as sources, deforming the action of boundary theory

$$< e^{\int J\mathcal{O}} >= \lim_{\epsilon\to 0} e^{S_{grav}[\phi, z\geq\epsilon]+S_{c.t.}[\phi, z=\epsilon]}$$

- $\phi(z=0)\sim J$ Boundary values of ϕ are sources for $\mathcal{O}$
- Extra "holographic" dimension z corresponds to scaling, so scaling dimensions of boundary operators ⇔ bulk energies.
- Global charges in the boundary theory ⇔ Gauge fields in the bulk
- Finite electron density is implemented with electric field in the bulk => consider charged Reissner-Nordström Black Hole background

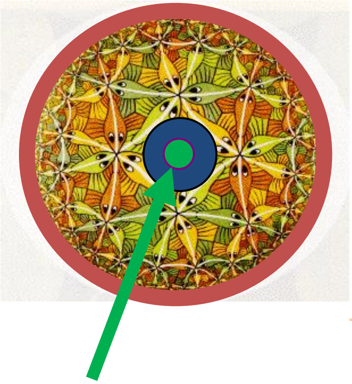

$$\frac{ds^2}{L^2} = \frac{1}{z^2}\left(-f(z)dt^2 + dx^2 + dy^2\right) + \frac{1}{z^2}\frac{dz^2}{f(z)} \,,$$

$$A = \frac{hx}{z_h}dy - q\left(1-\frac{z}{z_h}\right)dt \,, \qquad f(z) = 1 + (h^2+q^2)\alpha\frac{z^4}{z_h^4} - (1+(h^2+q^2)\alpha)\frac{z^3}{z_h^3}$$

$$\alpha = \frac{\kappa^2 z_h^2}{2g^2L^2}$$

The AdS/CFT dictionary

SUSY Einstein-Maxwell in AdS$_4$ ⇔ SUSY 3D Yang-Mills CFT

E-field

transverse E-field ⇔ 3d electric field
radial E-field ⇔ 3d charge density

B-field

radial B-field ⇔ 3d magnetic field
transverse B-field ⇔ 3d current density

spatial metric perturbations

transverse gradient ⇔ 3d distortion
radial gradient ⇔ 3d stress tensor

temporal metric perturbations

transverse gradient ⇔ temperature gradient
radial gradient ⇔ heat flow

Analytic computation of real-time transport properties:
Resistivity,
Heat conductivity
Nernst effect,
Magnetic susceptibility...

Entanglement entropy is proportional to Black hole horizon area.

General scheme of holographic computations

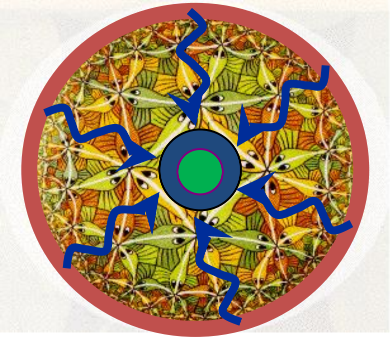

- Take some Gravity+Maxwell+.... background
- Couple some scalar/fermion/vector/spin-2 field

to it and solve equations of motion.

$$A_\mu(x,z) = a_\mu(x) + b_\mu(x) z + \ldots$$

$$\delta S_{\rm EM} = \frac{1}{g^2}\int d^3x\, \eta^{\mu\nu}\delta A_\mu \partial_z A_\nu \Big|_{z=0} = \frac{1}{g^2}\int d^3x\, \eta^{\mu\nu}\delta a_\mu b_\nu$$

$$\langle J^\mu \rangle = \frac{\delta S}{\delta a_\mu} = \frac{1}{g^2} b^\mu$$

- a and b are source and expectation value. If there is a solution with a=0 and b≠0 we get condensate (Black Hole with “hair”)
- AdS-to-ARPES program: Coupling fermions to various scalar, vector and tensor fields in the bulk, all types of behaviour can be generated: pseudogap, Fermi arcs, Fermi pockets

Examples of AdS-to-ARPES

- Fermi-liquid from charged black hole background (J.Zaanen et al, Science 325 (2009) 439)
- Marginal Fermi-liquid (C.M.Varma, P.B.Littlewood,S.Schmitt-Rink, E.Abrahams, A.E.Ruckenstein PRL 63, 18 (1989)) is constructed holographically from the same background. T-linear resistance is obtained for some values of parameters.(J.Zaanen et al, Science 325 (2009) 439,

S.S.Lee; Faulkner, Polchinki, Liu, Vegh, McGreevy, Iqbal, Sachdev....2009 -2010)

Low-energy theory can also be derived by conventional large-N approximation (from, e.g. Sachdev-Ye model). (Sachdev 2010)

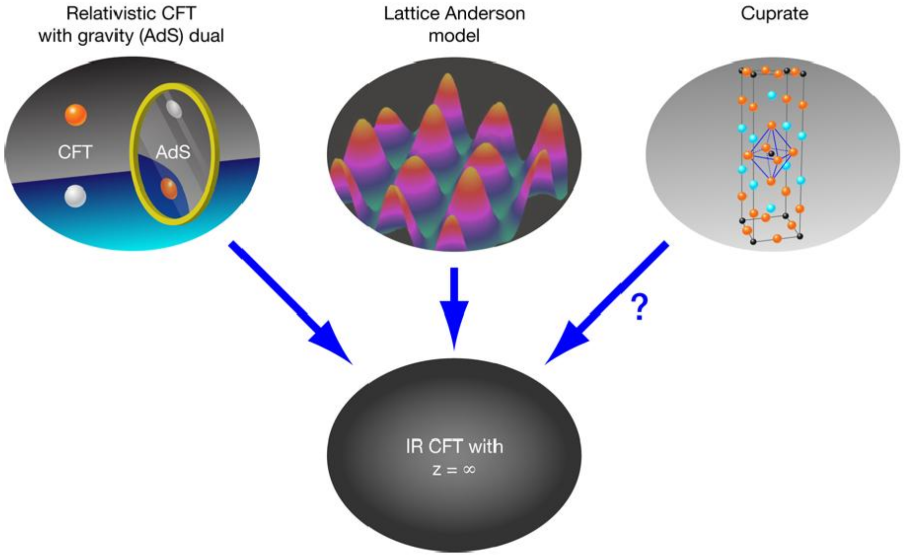

(Credit: Alan Stonebraker)

Examples of AdS-to-ARPES

- Fermi pocket and Fermi arc from coupling of fermions to p-wave order parameter and to spin-density wave order. (D.Vegh, 1007.0246)

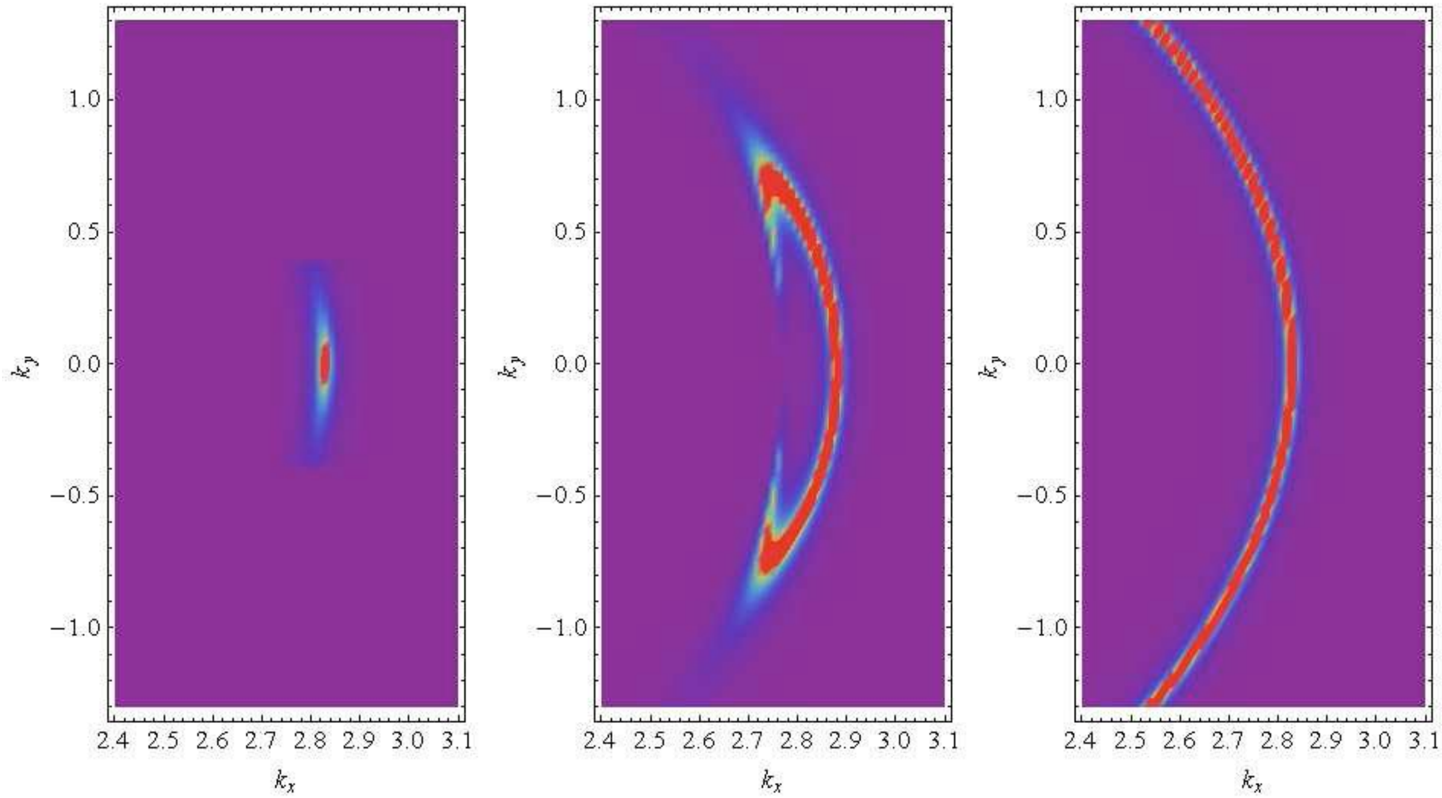

Holography as a tool to explore microscopic models

- How to connect to microscopic models?
- Semi-holographic models: Goldstone modes are extracted from low-energy dynamics. Obtained by holographic Wilsonian RG flow.
- “Fractionalization”, Spin-model ⇔ Lattice Gauge theory duality

New

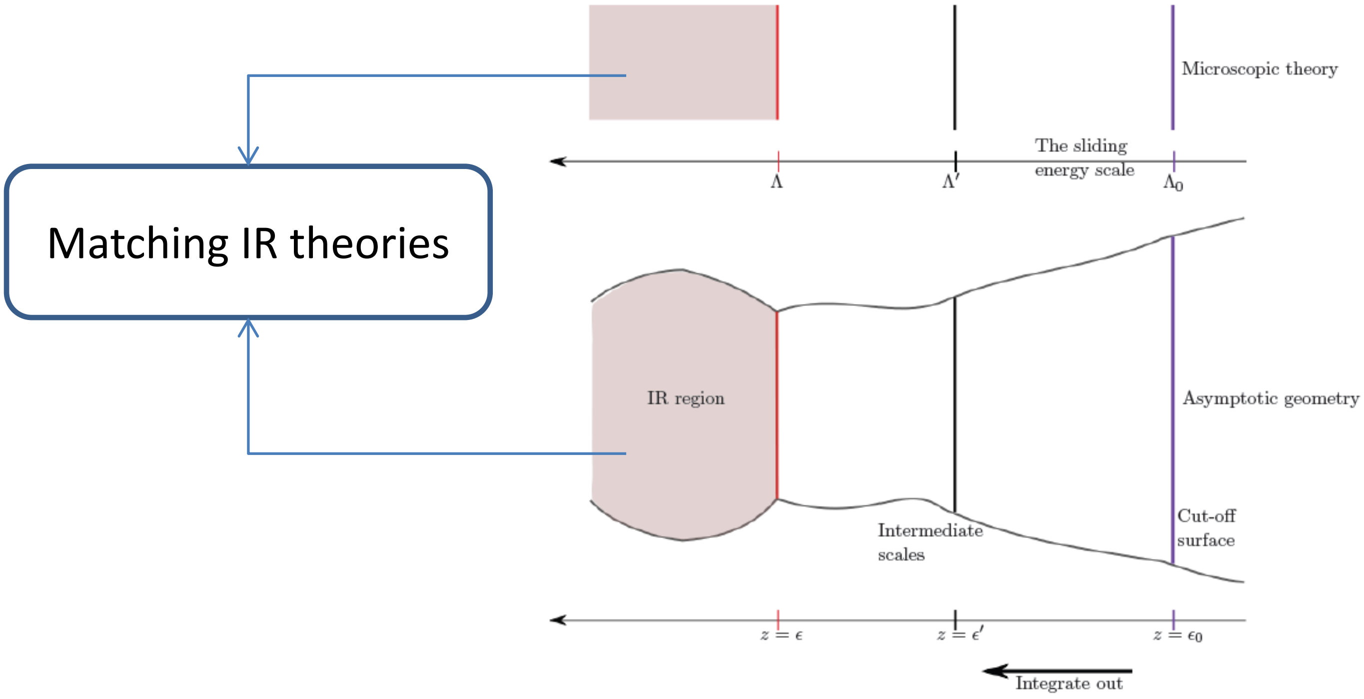

Matching IR theories

Faulkner,Liu,Rangamani 2010

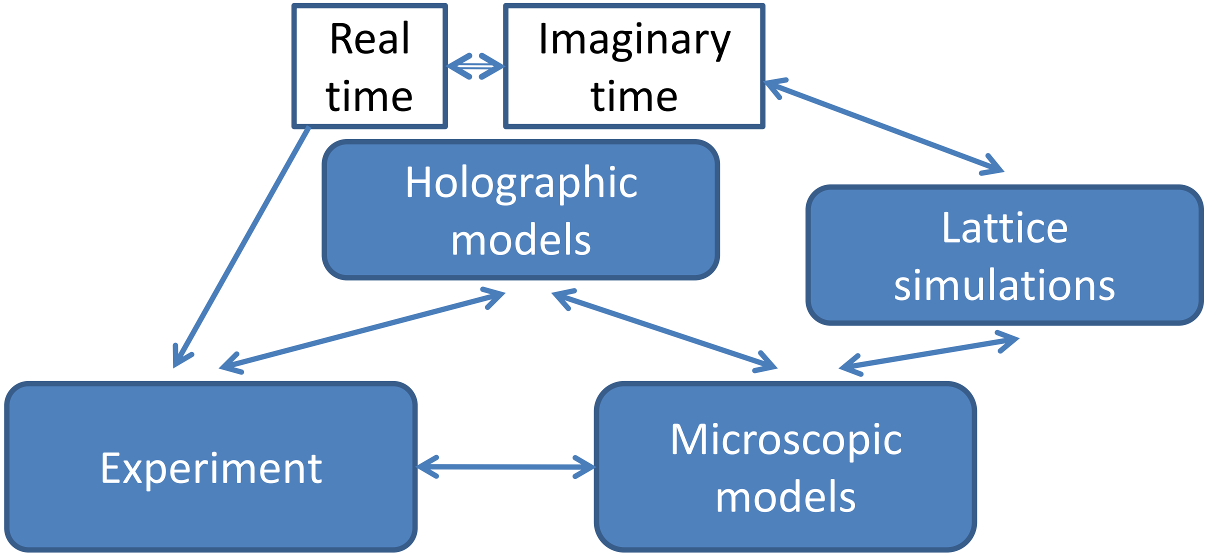

Real time

Imaginary time

Holographic models

Lattice simulations

Experiment

Microscopic models

Holographic models are good for:

Analytic computation of real-time transport properties:

Resistivity,

Heat conductivity

Nernst effect,

Magnetic susceptibility...

Entanglement entropy is proportional to the Black hole horizon area.

BUT: Underlying field content of holographic model is usually not clear.

Sachdev's work as a prototype S.Sachdev, PRL 105, 151602 (2010)

- Mean-field solution of Hubbard model ⇔ Holographic model
- Detailed correspondence between low energy Fractionalized FL and holography in which low-energy limit is factorized to $AdS_2 \times R^2$

$$H = H_0 + H_1[\mathfrak{d}, c] + H_{\rm AdS}$$

$$H_0 = \sum_\alpha \int \frac{d^2k}{4\pi^2} (\varepsilon_{\mathbf{k}} - \mu) c^\dagger_{\mathbf{k}\alpha} c_{\mathbf{k}\alpha}$$

Conduction electrons with small Fermi-surface

$$H_1[\mathfrak{d}, c] = \sum_\alpha \int \frac{d^2k}{4\pi^2} \left[V_{\mathbf{k}} \mathfrak{d}^\dagger_{\mathbf{k}\alpha} c_{\mathbf{k}\alpha} + V^*_{\mathbf{k}} c^\dagger_{\mathbf{k}\alpha} \mathfrak{d}_{\mathbf{k}\alpha} \right]$$

Hybridization with strongly-coupled IR CFT

$$\left\langle \mathfrak{d}_{\mathbf{k}\alpha}(\tau) \mathfrak{d}^\dagger_{\mathbf{k}\beta}(0) \right\rangle_{H_{\rm AdS}} \sim \left[\frac{\pi T}{\sin(\pi T \tau)} \right]^{2\Delta_k}$$

IR CFT

Marginal Fermi-Liquid for $\Delta_k = 1$

Connected with Anderson model: Spins form gapless spin liquid

$\mathfrak{d} \sim c\,\hat{S}$ In large-spin limit Sachdev gets the same IR CFT

Research plan

- Goal: develop QFTs near observed Quantum Critical points and connect them with AdS-CFT phenomenology at low energies.
- Match fractionalized (with slave-boson technique) microscopic models to semi-holographic models (with separation of Goldstone and Strongly-coupled modes) :
  - multiband Hubbard models;
  - include long-range Coulomb interaction
- Compare with conventional techniques for finding corrections to Fermi-liquid behaviour.
- Calculate physical properties and understand experimental data.
- Tune the holographic model by matching to lattice simulations and experiments
- Study the effects of impurity scattering in the models.
- Compare Holographic RG with Functional RG calculations

Semi-Holographic models

New

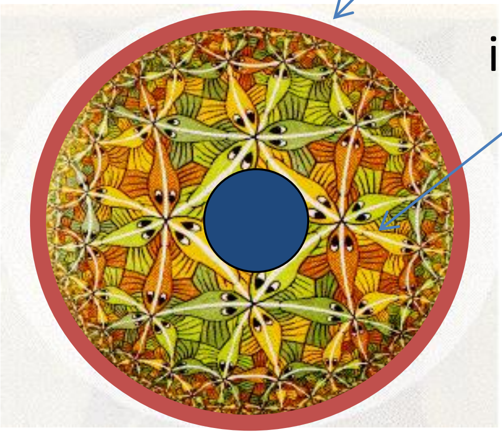

Non-trivial QFT on the boundary
that is
interacting with bulk modes

Shrinking the boundary generates the RG flow
Goldstone modes on the boundary are coupled to
IR modes in the bulk

Nickel, Son 2010 “Deconstructing holographic liquids”;
Faulkner, Liu, Rangamani 2010 “Integrating out geometry:
Holographic Wilsonian RG and the membrane paradigm”
Heemskerk, Polchinski 2010 “Holographic and Wilsonian RG”

List of influential papers

- Lee, Nagaosa,Wen 2006: Doping a Mott insulator: Physics of high-temperature superconductivity
- Sachdev 2010: The Landscape of the Hubbard model; Strange metals and AdS/CFT correspondence
- Faulkner, Polchinski 2010: Semi-Holographic Fermi Liquids
- Nickel, Son: Deconstructing holographic liquids
- Herzog 2009: Lectures on Holographic Superfluidity and Superconductivity
- Kusmartsev, Saarela 2008: Nanoscale structures and pseudogap in Under-doped High-Tc Superconductors

Bi forms Infinite $(BiO2)^-$ chains

- Short bonds to 4 oxygen atoms in the plane
- Forming a distorted square pyramid
- Which share edges with two Bi atoms
- Above and below the BiO2 plane

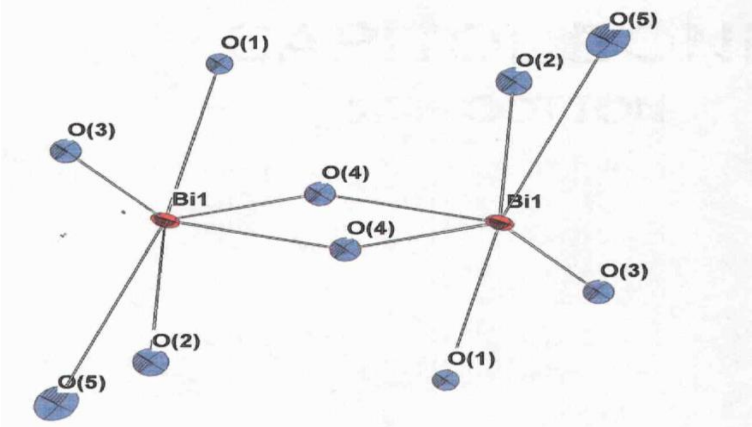

Bi forms Infinite $(BiO2)^-$ chains

short bonds to four oxygen atoms forming

toms forming a distorted square pyramid

Bi(III) has electronic configuration $[Xe]4f^{14}5d^{10}6s^{2}$

nonbonding electronic 6s pair, Bi^{3+}

distorted square pyramids share edges, with bismuth atoms above and below the mid-plane of oxygen atoms

The compounds $BiMNO_5$ (M = Ni, Co, Ca, Cd, Pb, N = P, V, As)